

ABSTRACT

GEBB II, DAVID MARTIN. Performance Characterization of a Single Abrasive Grit with Force Measurements and Visualization Techniques. (Under the direction of Dr. Thomas A. Dow.)

The goal of this project was to establish the characteristics among tool wear, geometry, and forces based on operating parameters experienced in the grinding process through experiments of single abrasive grit. Individual abrasive grits on a coated abrasive are generally within a given size range but can have a range of cutting geometries. Grit geometries can change as grits wear and fracture. Experiments were performed to determine an effective experimental procedure for testing and visualizing a single triangular shaped alumina grinding grit.

Shaped alumina grits were used in a single point turning experimental setup to remove material. Cutting forces were measured using a three axis load cell and simultaneous high speed video at 6006 frames per second was recorded. The experimental depth of cut was varied from 5 – 60 μm and the surface cutting speed from 1 – 8 m/s. High Speed videos were used to measure chip shear angles by measuring chip speeds. Shear angle measurements were limited to a maximum of 1 m/s cutting speed by the high speed video quality. Material build up at the cutting interface was sometimes observed when tool forces rose to the point of grit fracture. Abrasive grit geometry was measured through workpiece surface profiling techniques and optical microscopy. Methods of measuring both the grit and workpiece geometry combined with experimental control provided necessary tools to compare variable grit experiments.

Machining experiments were completed on 304 stainless steel, 4330V steel, 1215 steel and 52100 steel. Shaped alumina grits were oriented in different configurations on 304 SS to compare cutting characteristics. Experimental results were compared with Third Wave AdvantEdge simulations and an empirical cutting force model to determine the validity of cutting models in a single abrasive grit application. The Third Wave model fit the experimental data with mixed results; it was found that a few experiments followed cutting

simulations once localized geometry was determined for single abrasive grits. The empirical cutting model deviated from the experiments and was determined to be an ineffective method for tool characterization at this time.

Surface profiling techniques in conjunction with non-overlapping tool paths were used to successfully compare experiments with variable grit geometry that would otherwise make comparison difficult. The research and concepts developed within the context of this thesis provide experimental tools that can be utilized to optimize abrasive products from the perspective of a single grit.

© Copyright 2014 by David Martin Gebb II

All Rights Reserved

Performance Characterization of a Single Abrasive Grit with
Force Measurements and Visualization Techniques

by
David Martin Gebb II

A thesis submitted to the Graduate Faculty of
North Carolina State University
in partial fulfillment of the
requirements for the Degree of
Master of Science

Mechanical Engineering

Raleigh, North Carolina

2014

APPROVED BY:

Dr. Ronald O. Scattergood

Dr. Michael Kudenov

Dr. Thomas A. Dow
Chair of Advisory Committee

BIOGRAPHY

David M. Gebb II grew up in Brevard, NC – a small town nestled in the mountains of Western North Carolina. He grew up in a “Brady Bunch” family, being the ninth child of ten. David enjoys wandering around in the woods which is contrasted with his interest in catching a game of Pro Video Gaming. David attended NC State in his undergrad career where he graduated Summa Cum Laude with a BS Mechanical Engineering and a minor in Graphic Communications on December 2013. During his undergraduate studies he was a CoOp at Novartis Vaccines and Diagnostics in their new cell culture flu vaccine plant in Holly Springs, NC. David pursued a MS Mechanical Engineering degree in light of realizing his interest was in engineering research and design. David worked under Thomas Dow at the Precision Engineering Center at NCSU where he worked on the analysis and visualization of a single abrasive grain as part of the enclosed Thesis.

ACKNOWLEDGEMENTS

I greatly appreciate everyone that has helped me through the past year and a half of graduate school. This includes my countless friends, family, and professors not mentioned by name below.

Dr. Thomas Dow, for helping me with project direction and coming up with numerous ways to better test the grit. I also appreciate providing me a project to fund my graduate school career.

Ken Garrard for being a master at all things programming and operating the machines. You have helped me countless times with making sure something is running as it should, or effectively using equipment.

Dr. Ronald Scattergood for serving on my committee and giving an insightful perspective on alumina material and fracture mechanics.

Dr. Michael Kudenov for serving on my committee and working on a system to measure the temperature through infrared techniques (even if we never followed through).

Chuck Mooney for his expertise and help with the SEM as well as the AIF at NCSU for the facilities.

Third Wave systems for graciously providing an AdvantEdge license.

Sean, Greg, and John for cracking jokes on each other and enjoying the time in the lab.

Jesus for an example to live by. “Trust in the Lord with all your heart, lean not on your own understanding. In all your ways acknowledge him, and he will direct your path.” – Proverbs 3:5-6

TABLE OF CONTENTS

LIST OF TABLES.....	ix
LIST OF FIGURES	x
LIST OF SYMBOLS.....	xvi
1 BACKGROUND.....	1
1.1 MATERIAL REMOVAL PROCESSES	1
1.1.1 MACHINING	1
1.1.2 GRINDING	2
1.2 COATED ABRASIVES	2
1.3 GRINDING PHYSICS.....	4
1.4 GRINDING WEAR	6
1.5 PROBLEM STATEMENT	7
2 EXPERIMENTAL APPARATUS.....	7
2.1 ALUMINUM OXIDE GRIT MATERIAL	7
2.2 ALUMINA GRIT GEOMETRY	7
2.3 PRECISION LATHE	10
2.4 LOAD CELL AND dSPACE SYSTEM	12
2.5 HIGH SPEED VIDEO SYSTEM AND OPTICS	14
3 PRELIMINARY IDEAS FOR GRIT MOUNTING AND WEAR	15
4 GRIT GEOMETRY FOR FORCE AND WEAR EXPERIMENTS	17
4.1 GRIT GEOMETRY.....	17
4.2 TOOL HOLDER DESIGN	18
4.3 NEGATIVE RAKE ANGLE ORIENTATION.....	20

4.4	ZERO RAKE ANGLE ORIENTATION.....	21
4.5	HALFWAY RAKE ANGLE	22
5	GRIT CUTTING ASSESSMENT WITH FORCES AND IMAGING.....	23
5.1	BACKGROUND AND FORCES	23
5.1.1	FEED DIRECTION	24
5.1.2	GENERAL EXPERIMENTAL PROCEDURE.....	25
5.2	TRAVERSE EXPERIMENTS AND CHARACTERISTICS.....	25
5.2.1	TRAVERSE CUT GRIT EXPERIMENTS.....	26
5.2.2	TRAVERSE CUT CASE STUDY AT THE ZERO RAKE ORIENTATION.....	27
5.2.3	TRAVERSE CUT CASE STUDY AT THE NEGATIVE RAKE ORIENTATION	29
5.2.4	TRAVERSE CUT SUMMARY.....	35
5.3	PLUNGE EXPERIMENTS AND CHARACTERISTICS.....	36
5.3.1	PLUNGE CUT GRIT EXPERIMENTS FOR THE NEGATIVE RAKE ORIENTATION	38
5.4	HIGH SPEED CAMERA IMAGING	42
5.4.1	IN PROCESS VIDEO.....	42
5.4.2	VIEW OF GRIT AND FOCAL DEPTH	43
5.4.3	MATERIAL BUILD UP AND CHIP FORMATION	45
5.4.4	HIGH SPEED VIDEO CONCLUSIONS	50
5.5	GRIT PREPARATION FOR VISUALIZATION	51
5.5.1	GRIT PRE-SELECTION	51
5.5.2	GRIT SURFACE PREPARATION AND POLISHING	51
5.5.3	CUTTING INTERFACE PREPARATION.....	53
6	DEFINING GRIT CUTTING GEOMETRY	54

6.1	TOOL FORCE MODEL	54
6.1.1	MOTIVATION	54
6.1.2	ARCONA TOOL FORCE MODEL DESCRIPTION	55
6.1.3	MODEL FORCE COMPONENTS	57
6.2	MEASURING REMOVED WORKPIECE MATERIAL.....	57
6.2.1	INCREASING DEPTH SPIRAL.....	57
6.2.2	POLARIS PROFILE MEASUREMENTS.....	58
6.2.3	TALYSURF GROOVE MEASUREMENT	62
6.2.4	RELATING GROOVES TO FORCES	64
6.3	MEASURING FLANK CONTACT AREA	66
6.3.1	FLANK CONTACT INTRO	66
6.3.2	OPTICAL MICROSCOPE MEASUREMENTS	66
6.3.3	GRIT FLANK CONTACT AREA MEASUREMENTS: ZERO RAKE ORIENTATION	67
6.3.4	GRIT FLANK CONTACT AREA MEASUREMENTS: NEGATIVE RAKE ORIENTATION	70
7	GRIT CUTTING RESULTS.....	72
7.1	CUTTING SPEED COMPARISON: 304 SS	72
7.2	WORKPIECE MATERIALS	76
7.2.1	BACKGROUND ON MATERIALS	76
7.2.2	EXPERIMENTAL COMPARISON OF STEELS	76
7.2.3	EXPERIMENTAL VARIATION IN RELATED FORCES.....	80
7.3	GRIT ORIENTATION EFFECT.....	81
7.3.1	ORIENTATION IMPACT ON FORCES	81

7.3.2	ORIENTATION IMPACT ON GRIT FRACTURE AND MATERIAL REMOVAL.....	83
7.4	SPECIFIC CUTTING ENERGY COMPARISON	88
7.4.1	SPECIFIC CUTTING ENERGY BACKGROUND.....	88
7.4.2	SPECIFIC CUTTING ENERGY RESULTS	89
7.5	SHEAR ANGLE MEASUREMENT IN HIGH SPEED VIDEO	94
7.5.1	MEASUREMENT PROCESS	94
7.5.2	MEASURED SHEAR ANGLE IN HIGH SPEED IMAGING.....	96
7.5.3	SHEAR ANGLE WITH ERNST AND MERCHANT MODEL	98
8	MODELLING RESULTS.....	100
8.1	EXPERIMENTAL COMPARISON TO THE ARCONA MODEL	100
8.1.1	MODEL PARAMETERS	100
8.1.2	MODEL COMPARISON	100
8.1.3	CONCLUSIONS REGARDING THE ARCONA MODEL	107
8.2	FINITE ELEMENT THIRD WAVE ADVANTEDGE MODELS	108
8.2.1	BACKGROUND.....	108
8.2.2	FINITE ELEMENT ANALYSIS PARAMETERS	109
8.2.3	FEA MODEL AND EXPERIMENTAL GEOMETRY RELATION.....	111
8.2.4	EFFECT OF SPEED ON 304 SS IN ZERO RAKE ORIENTATION.....	114
8.2.5	EFFECT OF MATERIAL IN ZERO RAKE ORIENTATION.....	115
8.2.6	EFFECT OF RAKE ANGLE	119
8.2.7	THIRD WAVE MODEL TEMPERATURE.....	122
8.2.8	THIRD WAVE MODEL SHEAR ANGLE.....	127
9	CONCLUSIONS.....	128
9.1	FUTURE WORK	130

REFERENCES.....	133
APPENDICES.....	136
10 EXPERIMENTAL SETUP DETAILS	137
10.1 HIGH SPEED CAMERA SETTINGS	137
10.2 CAMERA FOCUSING TECHNIQUES.....	137
11 THIRD WAVE	139
11.1 FLANK AREA INTERPOLATION CURVES FROM MEASUREMENTS.....	139
11.2 THIRD WAVE MODEL MATERIALS	140
12 FURTHER EXPERIMENTAL SETUP DETAILS.....	142
12.1 WORKPIECE CONSIDERATIONS	142
12.2 LOAD CELL AMPLIFIER SETTINGS.....	143
12.3 NATURAL FREQUENCY OF LOAD CELL.....	143
13 TEMPERATURE	145
13.1 CUTTING TEMPERATURES	145
13.2 THERMOCOUPLE EXPERIMENT	145
13.3 THERMOCOUPLE MODEL RELATION.....	147
14 GRIT CLAMP/HOLDER DRAWING	149

LIST OF TABLES

Table 7-1. Workpiece Material Properties	76
Table 7-2. High Speed Video Shear Angle Measurements.....	97
Table 7-3. Shear Angles for Ernst and Merchant [31] Model.....	99
Table 8-1. 304SS Model Parameters.....	101
Table 8-2. 4330V Model Parameters	102
Table 8-3. 1215 Model Parameters	103
Table 8-4. 52100 Model Parameters	105
Table 8-5. 304 SS Negative Rake Model Parameters	106
Table 8-6. Modeling Parameters	110
Table 8-7. Third Wave Shear Angles.....	127
Table 10-1. High Speed Camera Settings	137
Table 11-1. Default Third Wave Workpiece Properties	141
Table 12-1. Amplifier Settings and Gains for Load Cell	143

LIST OF FIGURES

Figure 1-1. Coated Abrasive Belt	3
Figure 1-2. SEM Image of Shaped Alumina Grits [10] (left), Crushed Alumina Grits (right)	4
Figure 1-3. Orthogonal Tool Model: Positive Rake (left), Negative Rake (right).....	5
Figure 2-1. SEM Image of Alumina Grits on Coated Abrasive [10].....	8
Figure 2-2. Nominal Grit Dimensions on a Carbon Tape Background in a SEM.....	9
Figure 2-3. Grit geometry and variability at the scale of cutting.....	10
Figure 2-4. Experimental Setup	11
Figure 2-5. Grit and Workpiece Setup with Cut, Thrust and Side Force Components	12
Figure 2-6. Kistler Model 9251A Piezoelectric Load Cell and Axes [27]	13
Figure 2-7. Camera Setup and Flexure Focus Mechanism	14
Figure 3-1. First Mounting Techniques and Estimated Wear Pattern.....	16
Figure 3-2. Epoxy Mounting on a Flat Surface (left) and in a Notched Hole (right)	16
Figure 3-3. Grit Before Fracture (left), Grit After Fracture (right).....	17
Figure 4-1. Extreme Grit Orientations	18
Figure 4-2. Tool Holder: a) Top view and, b) Side view of grit placement with respect to the perpendicular holder surfaces and epoxy placement. c) Grit holder in the negative rake orientation and, d) the Zero rake orientation	19
Figure 4-3. Negative rake angle orientation.....	20
Figure 4-4. Microscope Image of Grit Contact Width for Negative Rake Orientation	21
Figure 4-5. Zero rake angle orientation	21
Figure 4-6. Microscope Image of Two Grit Rake Faces for the Zero Rake Orientation	22
Figure 4-7. Halfway Rake Orientation Oblique Rake Faces: Orthogonal to Cutting Direction (left), Top Perspective (right)	23
Figure 5-1. Feed Directions	25
Figure 5-2. Traverse Feed Experimental Representation.....	26
Figure 5-3. Zero Rake: Consecutive Traverse Tests at 5 μ m Depth, 1 m/s Speed, and 12 μ m Feed Using a Single Grit on 304 SS	28

Figure 5-4. Traverse Experiment at 5 μm Depth and 1 m/s for a Zero Rake Grit on 304 SS	29
Figure 5-5. Sample Negative Rake Angle Traverse Experiment at a 12 μm Feed and 1 m/s Speed on 304 SS	30
Figure 5-6. Average Cutting and Thrust Forces for Negative Rake Angle Traverse Experiments at a 12 μm Feed and 1 m/s Speed on 304SS.....	31
Figure 5-7. Standard Deviation for Cutting and Thrust Forces at 5 μm and 10 μm Depths for Negative Rake Angle Traverse at 12 μm Feed and 1 m/s Speed on 304SS	32
Figure 5-8. Maximum Forces for the Negative Rake Traverse Experiments at a 12 μm Feed and 1 m/s Speed on 304SS.....	33
Figure 5-9. 5 μm Depth, Negative Rake Angle: Experimental Data and Base Forces.....	34
Figure 5-10. Negative Rake Traverse Experiment Base Forces at 12 μm Feed and 1 m/s Speed on 304 SS	35
Figure 5-11. Plunge Cut Experiment Representation	37
Figure 5-12. Grit Contact Area for Plunge Experiment in the Extreme Orientations	37
Figure 5-13. Negative Rake Plunge Experimental Forces for Four Experiments at 10 μm Depth of Cut on 304 SS: 1 m/s in a) and b) while 0.1 m/s in c) and d).....	39
Figure 5-14. Average Forces for Negative Rake Plunge at 10 μm Depth of Cut on 304 SS	40
Figure 5-15. Average Force and Standard Deviation of Negative Rake Plunge at 10 μm Depth of Cut on 304 SS	41
Figure 5-16. Maximum Forces for the Negative Rake Plunge Experiments at 10 μm Depth of Cut on 304 SS.....	42
Figure 5-17. 42x Grit Video at 20 μs Shutter Speed: Negative Rake (left), Zero Rake (right)	44
Figure 5-18. Grit Variation and Focal Depth at 20 μs Shutter Speed.....	45
Figure 5-19. Chip Formation (left) and Material Build Up (right).....	46
Figure 5-20. Material Build Up and Resulting Force Increase	47
Figure 5-21. Buildup progression of a Negative Rake Plunge at 10 μm Depth and 0.5 m/s Speed on 304 SS at time: a) 0.300 s, b) 0.350 s, c) 0.353 s, d) 0.368s , e) 0.389 s, f) 0.420 s	48

Figure 5-22. Buildup progression of a Negative Rake Plunge at 2.5 μm Depth and 1 m/s Speed on 304 SS at time: a) 1.524 s, b) 1.575 s, c) 1.625 s, d) 1.637 s	50
Figure 5-23. Polished Grit Cutting 304 SS at 1 m/s	52
Figure 5-24. Grit at Zero Rake Orientation: Top down view of the rake face (left), Video Image of the side of the grit (right).....	53
Figure 5-25. Grit Wear Shaping Method: Original (left), after seven passes (right).....	54
Figure 6-1. Sketch of forces for the Arcona model.....	56
Figure 6-2. Increasing Depth Spiral Experiment with grit profiles every revolution	58
Figure 6-3. Polaris CMM and Optical Probe	59
Figure 6-4. a) Polaris Cylinder Measurement and b) Unwrapped Polaris Surface.....	60
Figure 6-5. Close up Unwrapped Polaris Measurement for Workpiece Grooves	61
Figure 6-6. Polaris Groove Profiles that were Distorted by Interpolation of Poor Data Density and Probe Drop Out.....	62
Figure 6-7. Axial Grit Profile with the Talysurf	63
Figure 6-8. Talysurf and Rotary Index Setup for Axial Profile Measurements.....	64
Figure 6-9. Relating forces to workpiece grooves at 0° spindle position (theta).....	65
Figure 6-10. Grit Profile: a) Top View, b) Side View	66
Figure 6-11. Zero Rake Flank Faces a) Top view and the two flank face edges, b) Side view and the flank face	68
Figure 6-12. True height measurement for a foreshortened surface [23]	68
Figure 6-13. Original and Stretched Flank Face Images	69
Figure 6-14. Flank Area Measurement	70
Figure 6-15. Negative Rake Flank Area a) Top View and projection of rake area, b) Front view, c) right side view and projection of flank area.....	71
Figure 7-1. Ten Increasing Depth Cutting Experiments at Different Cutting Speeds with Zero Rake Tool on 304 SS (** Experiments were at a Single Depth of Cut)	73
Figure 7-2. Zero Rake Speed Comparison for Cutting Forces on 304 SS	74
Figure 7-3. Zero Rake Speed Comparison for Thrust Forces on 304 SS.....	75

Figure 7-4. 4330 Steel Experimental Cutting Forces with Respect to Chip Area (** Experiment was at a Single Depth of Cut).....	77
Figure 7-5. 1215 Steel Experimental Cutting Forces with Respect to Chip Area	78
Figure 7-6. 52100 Steel Experimental Cutting Forces with Respect to Chip Area	78
Figure 7-7. Cutting Force Comparison for Steel Materials at 1 m/s Surface Speed.....	79
Figure 7-8. Thrust Force Comparison for Steel Materials at 1 m/s Surface Speed	79
Figure 7-9. Grit Orientation Impact on Cutting Forces	82
Figure 7-10. Grit Orientation Impact on Thrust Forces	82
Figure 7-11. Zero Rake Orientation Workpiece Profile	84
Figure 7-12. Negative Rake Orientation Workpiece Profile.....	85
Figure 7-13. Halfway Rake Orientation Workpiece Profile	86
Figure 7-14. Orientation Fracture Forces and Removed Chip Area	87
Figure 7-15. Fractures on a 304 SS at 1 m/s for an Increasing Depth Spiral: a) Zero Rake Orientation, b) Halfway Rake Orientation, c) Negative Rake Orientation.....	88
Figure 7-16. Specific Cutting Energy Comparison.....	90
Figure 7-17. Specific Cutting Energy Data Fit for Clarity	90
Figure 7-18. Specific Cutting Energy Comparison for 304 SS Speeds	91
Figure 7-19. Specific Cutting Energy Comparison for Rake Orientation.....	92
Figure 7-20. Specific Cutting Energy Comparison to Depth of Cut for Rake Orientations .	93
Figure 7-21. Chip Speed Calculation Images for a Negative Rake Plunge	94
Figure 7-22. Shear Angle Relation to Chip and Workpiece Velocity	95
Figure 7-23. Four Contiguous Images for a Zero Rake Increasing Depth Spiral Used to Calculate the Shear Angle.....	96
Figure 8-1. 304 SS Cutting Force: Experiment and Modeled Fit	101
Figure 8-2. 304SS Thrust Force: Experiment and Modeled Fit.....	101
Figure 8-3. 4330V Cutting Force: Experiment and Modeled Fit.....	102
Figure 8-4. 4330V Thrust Force: Experiment and Modeled Fit	103
Figure 8-5. 1215 Cutting Force: Experiment and Modeled Fit.....	104
Figure 8-6. Thrust Force: Experiment and Modeled Fit	104

Figure 8-7. 52100 Cutting Force: Experiment and Modeled Fit.....	105
Figure 8-8. 52100 Thrust Force: Experiment and Modeled Fit	105
Figure 8-9. Negative Rake Orientation Cutting Force: Experiment and Modeled Fit.....	106
Figure 8-10. Negative Rake Orientation Thrust Force: Experiment and Modeled Fit	107
Figure 8-11. AdvantEdge Parameter Description [34]	109
Figure 8-12. Tool Geometrical Parameters for a) Zero Rake, b) Negative Rake	112
Figure 8-13. Zero Rake Width Approximation for AdvantEdge	113
Figure 8-14. 304 SS Speed and Cutting Force Comparisons to Third Wave	114
Figure 8-15. 304 SS Speed and Thrust Force Comparisons to Third Wave.....	115
Figure 8-16. Steel Cutting Force Comparisons to Third Wave	116
Figure 8-17. Steel Thrust Comparisons to Third Wave	116
Figure 8-18. 1215 Cutting and Thrust Comparison to Third Wave.....	117
Figure 8-19. Third Wave Grit Orientation Effect on Cutting Forces at 1 m/s for 304 SS..	119
Figure 8-20. Third Wave Grit Orientation Effect on Thrust Forces at 1 m/s for 304 SS ...	120
Figure 8-21. Third Wave Grit Orientation on Cutting Forces at 1 m/s for 52100 Steel.....	121
Figure 8-22. Third Wave Grit Orientation on Thrust Forces at 1 m/s for 52100 Steel.....	121
Figure 8-23. 304 SS Peak Tool Temperatures at 1, 4, and 8 m/s Cutting Speed.....	123
Figure 8-24. Peak Tool Temperatures of Steel Workpieces	124
Figure 8-25. 304 SS Temperature Profile at 1 m/s and 20 μm Depth	125
Figure 8-26. 1215 Temperature Profile at 1 m/s and 20 μm Depth	125
Figure 8-27. 52100 Temperature Profile at 1 m/s and 20 μm Depth	126
Figure 8-28. Negative Rake Orientation for 304 SS at 1 m/s and 20 μm Depth	126
Figure 10-1. Camera Focus Locations for: a) Negative Rake Orientation Viewpoint, b) Zero Rake Orientation Viewpoint	139
Figure 12-1. Discontinuous Workpieces: 40 mm Contact (left), 3 mm Contact (right).....	142
Figure 12-2. Load Cell Response (left) and FFT (right).....	144
Figure 12-3. FFT of Several Load Cell Reponses	144
Figure 13-1. Thermocouple Placement on Grit	145
Figure 13-2. Measured Cutting Forces and Temperatures.....	146

Figure 13-3. Analytical Grit Model as a 60° Segment of a Circle..... 147
Figure 13-4. Peak Grit Comparison for Two Measured Temperatures 148
Figure 14-1. Grit Holder Dimension Drawing: Units are in Inches..... 149
Figure 14-2. Grit Clamp Dimension Drawing: Units are in Inches 150

LIST OF SYMBOLS

<u>Symbol</u>	<u>Meaning</u>
μ	Friction coefficient between the rake face of the tool and workpiece
μ_f	Friction coefficient at the flank face of the tool and workpiece
μ_s	Specific cutting energy
A	Area
A_c	Removed chip area
$A_{experiment}$	Experimental Area
A_f	Flank contact area of tool
$A_{profile}$	Removed chip area or removed material area
d	Depth
E	Elastic Modulus
F_c	Cutting Force
F_t	Thrust Force
G	Grinding Ratio
H	Hardness of workpiece material
P	Power
P_c	Cutting Force
P_t	Thrust Force
Q	Volume removal rate for material
r_c	Cutting ratio
v_{chip}	Chip speed
v_{cut}	Workpiece speed or cutting speed
$V_{Removed}$	Volume of material removed from workpiece
v_w	Workpiece speed or cutting speed
V_{Wear}	Volume of wear on abrasive product
W_{model}	Width of tool for the model
α	Shear angle of the chip
σ_s	Normal Stress
τ_s	Shear Stress
ϕ	Rake Angle

1 BACKGROUND

1.1 MATERIAL REMOVAL PROCESSES

There have been many methods developed to remove excess material from a part or workpiece. These material removal processes have aided innovation by providing the ability to shape parts for complex machines all the way to insignificant household commodities. Understanding and improving specific mechanisms involved with any type of material removal process can give the upper hand to an innovator against competing parties. Small improvements can create better products that remove material more efficiently, which can correlate to larger profit margins.

1.1.1 MACHINING

Machining is characterized by removing material from a workpiece with a harder tool, or a collection of tools, that has a sharp edge. Machining can take many different forms and is categorized by the methods that a workpiece and tool contact and remove material. A few brief examples of different machining methods are given for clarity. Lathing uses a stationary tool with a spinning workpiece to remove material on the outer diameter of the workpiece. A mill uses a rotating tool to remove material as the workpiece moves under it. Grinding uses a collection of sharp abrasive particles to remove material.

Grinding and machining operations have been researched and many publications date back to the 1940's and 1950's. Research was conducted before this but according to Merchant [1] this was an important era in the development in the current understanding of machining processes. Classical models developed during the 1940's and 1950's are still used as a basis due to their simplicity. According to Shaw [2], the idea that machining was a product of a concentrated shear plane came from contributions from Ernst, Merchant, and Piispanen. A concentrated shear plane refers to a location in the workpiece where the stresses from a tool shear and remove the material from the body of the workpiece in a chip formation process. These early breakthroughs in machining comprehension ultimately lead to the orthogonal cutting model described by Merchant [3] in 1945. The classical models have progressed into more complex models that simulate cutting based on workpiece material properties and tool

geometries. An extensive review of cutting models is given by Shaw [2]. Other models have been developed by Drescher [4] in 1992 and Arcona [5] in 1996 to predict forces in precision machining. However, each model is usually applicable for parameters that are similar to the conditions which the model was based on. Shaw [2] attributes the limits of any model to the over-simplification of the intricate material removal process.

1.1.2 GRINDING

Grinding is a generic term that describes machining with abrasive particles. An abrasive particle is synonymous to abrasive grits or abrasive grains, and shortened further to just a grain or grit. Grinding processes can be further defined by the method that abrasive products are held together. The two main categories of grinding abrasives are bonded and coated abrasives [6,7].

Bonded abrasives include products like grinding wheels and are composed of grits held together by a rigid bonding matrix. Bonded abrasives make up the majority of abrasive products due to their versatility in general grinding, sharpening, and cutting applications. They are used for cutoff applications where material is cut off from ends of workpieces, and in precision applications where the rigid structure of the wheel allows small material removal depths.

Coated abrasives are made up of a single layer of abrasive grits that are attached to a flexible substrate backing material with resin. The substrate material can be a cloth, paper, or polymer material and include products such as an abrasive disk, sandpaper, or abrasive belt. Coated abrasives are used in surface-treatment applications from smoothing and finishing to stock material removal, where a large quantity of material is removed.

1.2 COATED ABRASIVES

Coated abrasives are generally manufactured by orienting grits on the backing belt by an electrostatic charge [6] (in Chapter 2). The charge arranges the grits with the longest, most slender, dimension vertical while the rest of the geometry is oriented without certainty. This process provides good placement with many sharp grit edges facing outwards, which

promotes more material removal. A first coat of resin is used to hold the grits in place after the electrostatic field is removed and a second coat of resin is used to further secure them [8]. The outer layer of resin completely covers the abrasive grains as shown on the coated abrasive belt in Figure 1-1 (the grits appear as bumps).

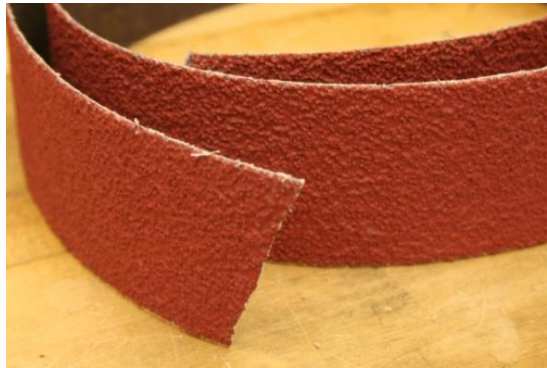


Figure 1-1. Coated Abrasive Belt

Recent advancement of coated abrasive products includes micro-replication techniques that replaced randomly oriented and geometrically shaped grains with a replicated geometrical structure. Such products promised to remove material more consistently and efficiently to provide a longer life and better surface finish. One of the first products was named Trizact by 3M and consisted of three-dimensional pyramids that were uniformly distributed across the product surface [9]. The pyramid structures were made of multiple layers of smaller abrasive material so that when a layer wore down the next layer of the pyramid was exposed to the workpiece. Another design was introduced in 2009 that had shaped abrasive grains that also promised an improvement of material removal, belt life, and surface finish. The millimeter sized structures are flat triangular prisms shown in Figure 1-2 on the left, while conventional grinding grits that are irregular and blocky in shape are shown on the right of Figure 1-2. Shaped abrasive are proposed to act more like individual cutting tools that remove material instead of a randomly shaped blocky grain that plows through material [10].

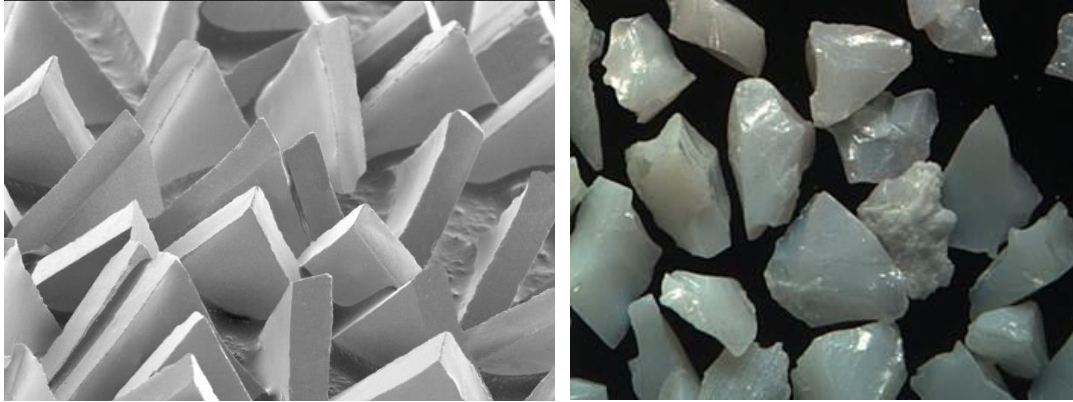


Figure 1-2. SEM Image of Shaped Alumina Grits [10] (left), Crushed Alumina Grits (right)

1.3 GRINDING PHYSICS

The physics of grinding is similar to machining but has different tool geometry. While milling and lathing tools generally have a single well-defined cutting region that is then worn down by machining, grinding is made up of up of many grits acting cooperatively in the cutting process. This is appealing when cutting hard to machine materials. Where a single tool would wear quickly, many cutting tools or abrasive grains wear together and the product as a whole can last longer before it is replaced.

However, there are still challenges with grinding. Individual grits have a different width, depth, length and position [6,11,12] which change the tool/workpiece contact conditions and effect material removal morphologies [13-17]. The geometry variation between grits on a single abrasive product can impact the surface finish quality of a grinding product at identical machining conditions [9,18].

Main mechanisms of individual grit/workpiece contact are rubbing, plowing, and cutting [12,19]. No material is removed through rubbing and plowing but still impacts forces and grit wear. Rubbing is due to frictional forces of the contacting grit, causing elastic deformation, while plowing plastically displaces material without fully removing it from the workpiece. Cutting is what completely removes material from the workpiece, but still may be accompanied by rubbing and plowing. Cutting is also the most efficient method of material

removal; that is the least energy used per material volume removed. In grinding the majority of the grits either rub or do not contact the workpiece, while only a few grits are actively removing material by cutting [17,20].

Shaw (in Chapter 1) [6] explains that grinding is influenced by the large cutting edge radius of the tool and often times, large negative rake angle. This creates a small region of plastic deformation in the workpiece and chip. The rake angle is shown in Figure 1-3 and represents the contact angle of the front face of a tool with respect to a position normal to the workpiece surface. Komanduri [21] also compared grinding of a single grit to cutting with a large negative rake angle tool because of the large cutting edge radius of the grit.

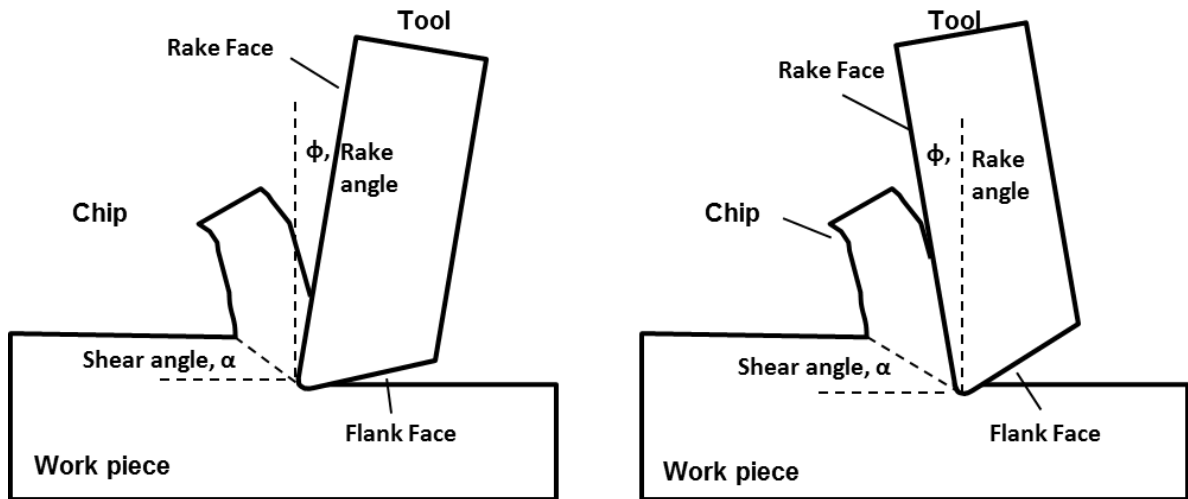


Figure 1-3. Orthogonal Tool Model: Positive Rake (left), Negative Rake (right)

Shaw [6] distinguishes two approaches to study grinding; deterministic and stochastic. Deterministic includes studying the performance of single grits [20] and stochastic studies the overall performance of a grinding belt/wheel. The deterministic approach will be taken in this thesis even though single grit performance may be hard to compare at a wide range of grinding conditions with non-uniform geometry between grits.

1.4 GRINDING WEAR

Mechanisms of wear in grinding are typically attritious wear, fracturing, and grain pull out [6,8,11,12,22]. Grain pull out was not a mechanism of wear that was studied within this thesis because it occurs at the bonding agent of a grinding belt or wheel, not at an individual grit. Attritious wear is a flattening of the flank face (flank wear) or further dulling of the grit cutting radius. Effects of attritious wear may lead to an increase in forces and lead to grit fracture. Attritious wear can also have a large impact if the cutting tool and workpiece have a chemical affinity. For example, in the case of alumina on steels, flank wear is lower than other materials since the two materials are fairly inert, [8] (in Chapter 22 and 26). Grain fracture can either be small scale, retaining grit shape, or large scale splitting the grit into multiple fragments. The individual microstructure has a large impact on which type of fracture is most common [12] (in Chapter 3).

Wear is typically measured in a product perspective via a grinding ratio, or the volume of material removed from the workpiece, $V_{Removed}$, to volume of wear on the abrasive product, V_{wear} . A grinding ratio represents the overall performance of a coated abrasive or grinding wheel where the quantitative values of material are significant enough for measurements and comparisons. The grinding ratio is given in Equation (1-1).

$$G = \frac{V_{Removed}}{V_{wear}} \quad (1-1)$$

The grinding ratio can also be measured by the change in weight of the workpiece compared to the abrasive product. The weight of the wear is then related to the equivalent volume of the material. In some applications of grinding, the weight may be more convenient to measure than the volume. However, the grinding ratio was not applied to the single abrasive experiments in this thesis. The methods employed to measure removed workpiece material or wear of a single abrasive grit was not adequate for practical volume measurements.

1.5 PROBLEM STATEMENT

The research and concepts developed in this thesis sought to provide necessary tools to visualize and evaluate a single abrasive grit during cutting. High speed video was used to capture images of the grit cutting while tool forces were recorded with a load cell. Experimental results were compared to finite element simulations and empirical cutting models to determine the validity of models in a single abrasive application. The goal of this project was to establish methods to distinguish characteristics among tool wear, geometry, temperature and forces based on operating parameters experienced in the grinding process.

2 EXPERIMENTAL APPARATUS

2.1 ALUMINUM OXIDE GRIT MATERIAL

The grit material used in the experiments within this thesis is an unknown composition of Aluminum oxide. Aluminum oxide has the general material composition Al_2O_3 and is also referred to as alumina, corundum and emery. Alumina is a generic term and may refer to a pure alumina substance or may have other material compositions added for improved physical properties. Alumina is known for its physical properties of high hardness and strength. The mechanical properties of alumina are affected by the material microstructure and tend to fail by fracture. The fracture force is dependent on the specific microstructure of the grit; therefore a well-designed grit microstructure could produce fracture at beneficial intervals. For instance, alumina grits are often used for ferrous metals like steel because they have a low chemical affinity to ferrous metals, but also fracture before abrasive wear has much time to negatively affect cutting [6,12].

2.2 ALUMINA GRIT GEOMETRY

Even though grinding consists of removing material with many cutting surfaces from a plethora of grits, an individual grit removes a small amount of material at localized geometry and depth of cut. The coated abrasive of interest in is shown in Figure 2-1. It consists of a large number of triangular Al_2O_3 grits that are glued to a fiber belt. Figure 2-1 shows that the result of grit mounting is mostly upright triangular abrasives that are randomly orientated with respect to direction of travel of the abrasive belt.

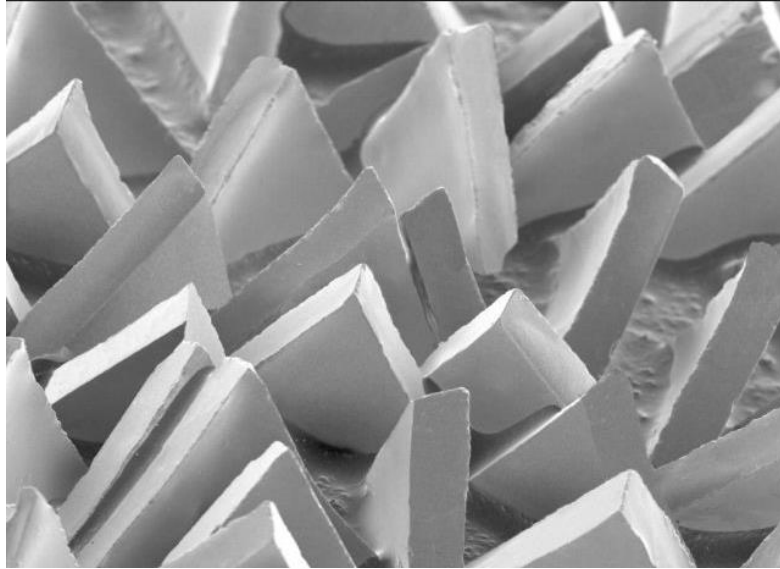


Figure 2-1. SEM Image of Alumina Grits on Coated Abrasive [10]

The approximate dimensions of the grits are given Figure 2-2; however individual grits may have slightly different dimensions and geometrical fluctuations. The benefit of using the shaped abrasive grits is that each grit has similar surfaces on a large scale for repeatable mounting, visualization with the high speed video system, and testing in distinct orientation differences. The relatively flat faces of the grit were used as regions to focus the high speed optical system for insight on the cutting process. More detail for the mounting and video are given in Sections 4 and 5.4 respectively.

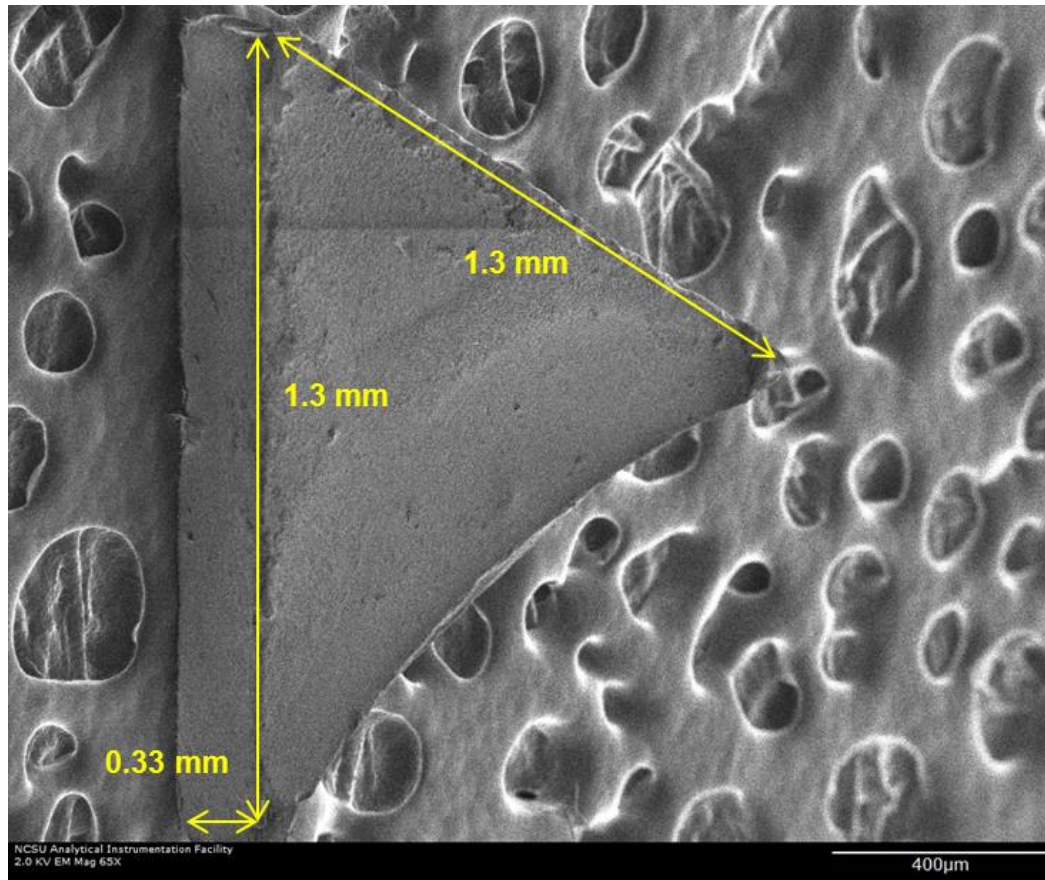


Figure 2-2. Nominal Grit Dimensions on a Carbon Tape Background in a SEM

However, even though the grit shape itself is generically planar, there are still variations on the same grit on the scale of the chip formation. Figure 2-3 shows the variability of a single grit on the micrometer scale as well as the comparatively large cutting and nose radius. One of the three vertices of the triangular face of the grit from Figure 2-2 is shown in Figure 2-3.

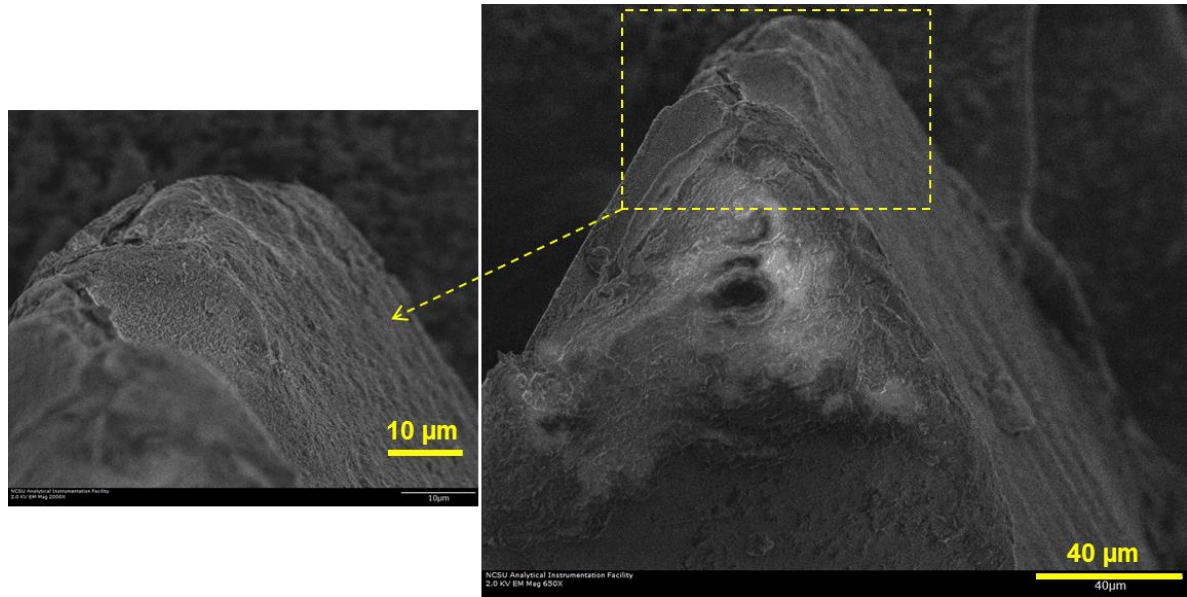


Figure 2-3. Grit geometry and variability at the scale of cutting

A typical depth of cut may be in the range of $10\ \mu\text{m}$. Looking at the Figure 2-2 there is variability at the nose with different ridges and high spots on the grit. A case study was done to measure the cutting radius of a specific grit to give the order of magnitude of the grit geometry. The measurement followed the procedure that Lane [23,24] and Shi [25,26] used for measuring diamond tools, called an EBID (Electron Beam Induced Deposition) measurement. The recorded edge radius was $20\ \mu\text{m}$. This was only used as a general scale relation since individual grits would be different.

2.3 PRECISION LATHE

The single grit grinding process was studied using a high precision, two axis lathe shown in Figure 2-4. The lathe is a Rank Pneumo ASG 2500 diamond turning machine (DTM) with two orthogonal slides. The X-axis carries the tool and the Z-axis carries the spindle. The DTM axes are moved by specifying a coordinate position and movement feed rate. The machine is equipped with feedback control for accurate movement. The DTM axes are equipped with laser interferometer system that allows a movement resolution of $2.47\ \text{nm}$. The axes are driven by DC servo motors that are converted to a linear motion through 0.2

inch pitch lead screws. The workpiece was attached to the spindle that rotates around the z-axis on an air bearing at speeds ranging from 100 to 1600 RPM.

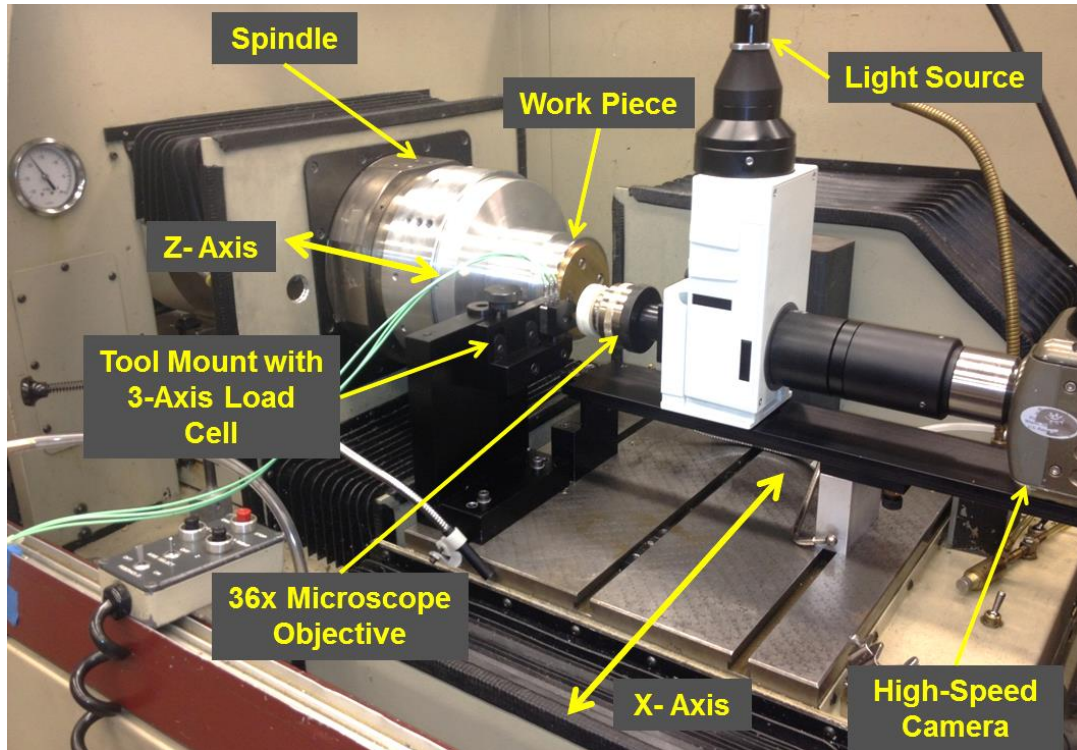


Figure 2-4. Experimental Setup

Workpieces were thin disks with diameters between 3.5 to 5 inches and thicknesses between 1/32" to 1/4". The workpiece was attached to the DTM spindle. Excess run out of the workpiece was removed before experiments by facing off the workpiece diameter with a carbide tool. A segmented workpiece could replace the cylindrical workpiece for discontinuous cutting experiments. Further orientation and experimental procedure of the grit and workpiece are described in Section 4.

A tool mount was bolted on the x-axis of the DTM as shown in Figure 2-4 and could be adjusted for various tool heights. Using the tool holder, the cutting edge of the tool was

aligned with the center of the workpiece. The grit was held on a tool shank that could be removed from the tool mount for tool wear analysis. The tool mount also held the three-axis load cell used to record cutting forces. A high speed camera with a 36x microscope objective captured the cutting process simultaneously as forces were recorded. A high intensity light source illuminated the grit and chip field of view of the camera for the short exposure times needed for a high frame rate.

2.4 LOAD CELL AND DSPACE SYSTEM

The load cell was a Kistler model 9251A three axis piezoelectric load cell; two axes are in shear and one in compression. The load cell measured cutting, thrust, and side forces that were tangential, normal and axial to the workpiece as shown in Figure 2-5. A diagram of the load cell is given in Figure 2-6.

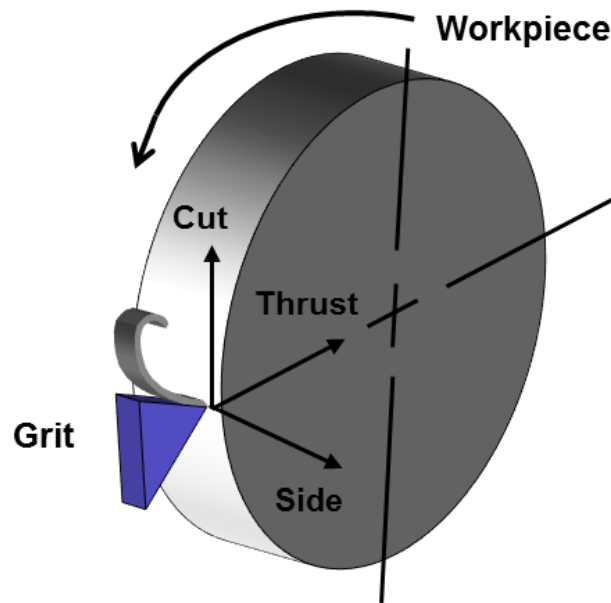


Figure 2-5. Grit and Workpiece Setup with Cut, Thrust and Side Force Components

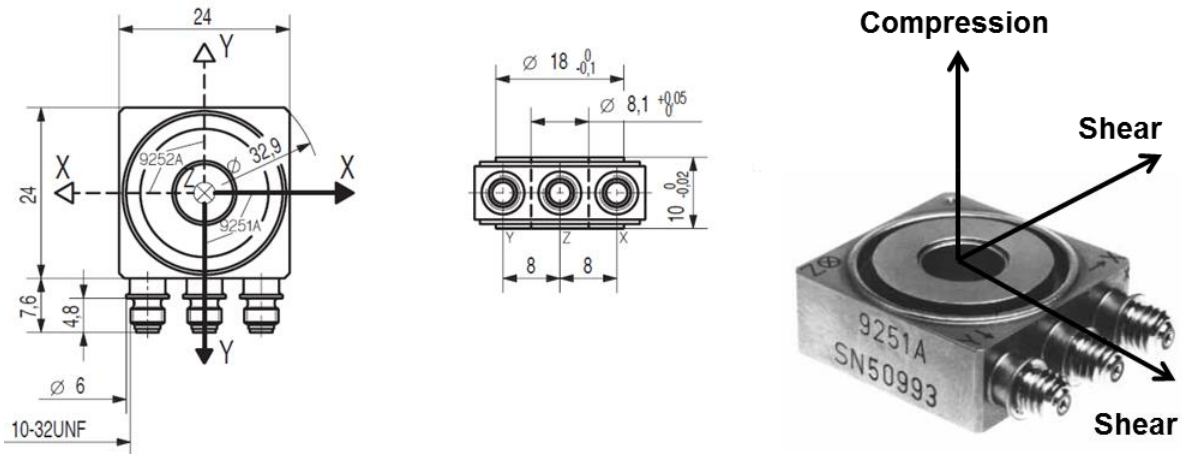


Figure 2-6. Kistler Model 9251A Piezoelectric Load Cell and Axes [27]

The recorded forces are often referred to together as the cutting forces. The cutting and thrust forces were measured with the shear axes and the side force with the compressive axis. The sensitivity of the compression axis is 4 pC/N and the shear axes were 8 pC/N while the stiffness of the compression axis was 2600 N/ μ m and the shear axes were 1000 N/ μ m. The natural frequency of the two shear axes, corresponding to the cutting and thrust forces, was measured to be 11.6 kHz. The load cell was read through a 3 channel, 10 V, Kistler 5004 amplifier. The gain and miscellaneous settings of the amplifier are given in Appendix 12. The load cell and amplifier could measure forces up to 45-50 N.

The load cell was calibrated by fitting a linear regression to measurements of 200, 500, and 1000 gram weights. The resulting slope of the linear regression for each load cell axis is the calibration factor. A dSpace data acquisition system was set to record the data at a sample time of 5 kHz. The data collected was the cutting, thrust, and side forces, as well as spindle position, spindle velocity, and either the x or z DTM axis position. A choice between measuring the x or z axis position was due to a limitation of serial ports on the dSpace system. The dSpace system was also used to trigger the high speed camera for simultaneous visual data collection. The trigger was a voltage signal sent to the camera once the thrust

force signal reached a magnitude of 0.12 V or about 0.5 N. The data that was recorded by the dSpace system was also recorded once the thrust force reached the aforementioned trigger magnitude.

2.5 HIGH SPEED VIDEO SYSTEM AND OPTICS

The high speed camera in Figure 2-4 was aligned with the grit and workpiece to provide high speed imaging of the cutting process. The camera and grit were both positioned on the DTM x-axis so they moved together while the workpiece moved independently on the z axis. The camera was mounted on a stand that could be adjusted for fine focus of the camera. The focus was adjusted by a flexure mechanism shown in Figure 2-7. A screw on the flexure is advanced by 25 $\mu\text{m}/\text{rev}$ which causes the flexure to bend and moves the entire camera a few micrometers towards the workpiece. A 36x Newport reflective microscope objective and a 1.2x camera attachment was used to magnify the cutting interface. The combined optical system had a magnification of 43.2x which corresponded to a 440 μm by 330 μm viewing window of the cutting process and depth of view of 30 μm .

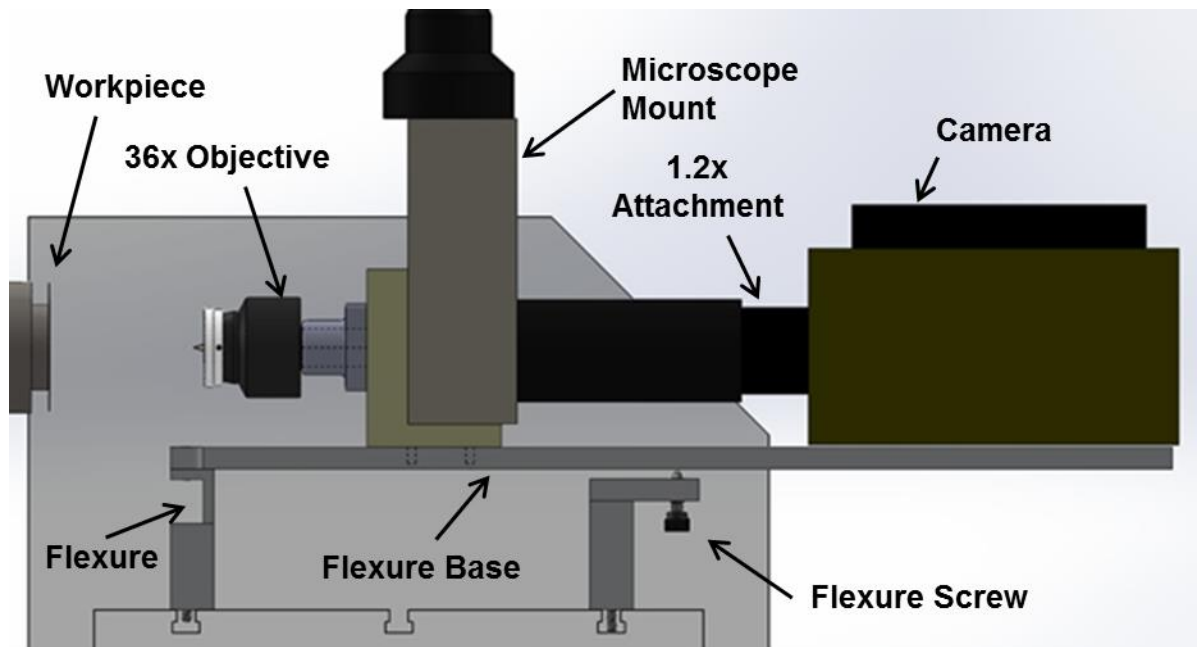


Figure 2-7. Camera Setup and Flexure Focus Mechanism

The high speed camera is a Phantom Cam v7.3 with a detector array of 800 x 600 pixels that can run at speeds up to 6006 FPS (frames per second). The video camera contained 16 GB (gigabytes) of memory, which corresponds to about 3.4 seconds of continuous video footage at 6006 fps or 6.8 seconds at 3000 fps. The camera was capable of a circular recording buffer, meaning it could record video a set time before and after the trigger time. Information on how the high speed imaging system was used to capture cutting is given in Section 5.4. The shutter speed could be as short as 1 μ s. However, as the shutter speed was reduced, more light was required to produce the same image intensity on the detector. The shutter speed was typically set at 10 μ s to 20 μ s for experiments to provide acceptable images.

The shutter speed had a large impact on motion blur for moving objects in the field of view; a shorter speed could capture faster objects. Clarity of material visualization suffered at long exposure times and resulted in blurred still frame images. The exposure time was balanced to capture both objects in motion and stationary ones. A Prior Lumen 200 light source was directed to the field of view through the top of the microscope mount in Figure 2-7. The light is redirected in the microscope mount to follow the same optical path as the video camera. The light source was a 200 W white light halogen source.

3 PRELIMINARY IDEAS FOR GRIT MOUNTING AND WEAR

The first method of testing the grit was by cutting with a long edge of the triangular grit with a workpiece thinner than the grit (<1 mm). This is different than how the grit would be oriented on the coated abrasive in Figure 2-1. This method was designed so the resulting tool wear would leave an unworn fiducial region that could be compared to the worn region. Figure 3-1 describes the grit orientation and expected wear pattern. This concept has been used extensively for diamond tools [4,5,23,25]. However, grit wear was much different than the anticipated pattern described in Figure 3-1.

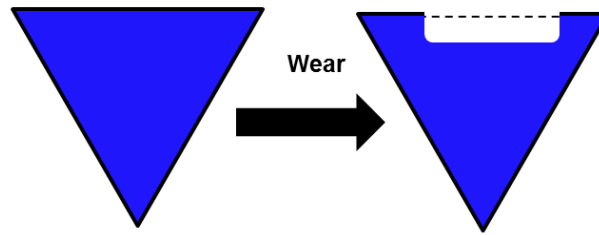


Figure 3-1. First Mounting Techniques and Estimated Wear Pattern

More significant difficulties in early experiments involved problems of grit mounting with epoxy alone. The epoxy was a 3M two part structural epoxy, called DP-460 off white. The DP 460 was cured at 60°C for two hours for maximum bond strength. Two methods of using epoxy to secure the grit are shown in Figure 3-2. Epoxy was placed around and under the grit on a flat mount and also in a small notched hole that fit the tip of the grit. Both methods utilized epoxy as the main source of securing the grit.



Figure 3-2. Epoxy Mounting on a Flat Surface (left) and in a Notched Hole (right)

If the epoxy did not fail, the grits were found to fracture in large sections that did not leave regions of the tool untouched by wear as anticipated in Figure 3-1. An example of how much of the grit was removed during the fracture is given in Figure 3-3.

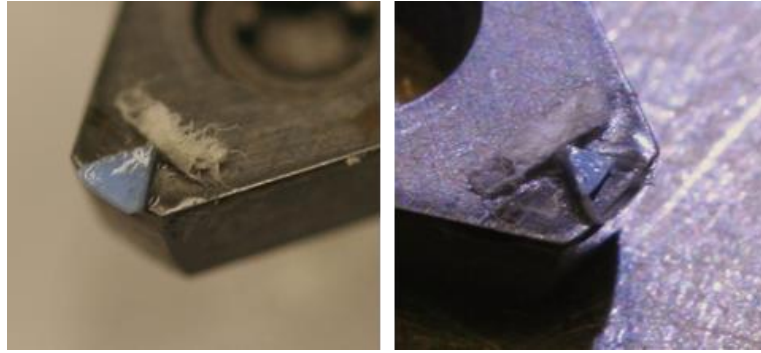


Figure 3-3. Grit Before Fracture (left), Grit After Fracture (right)

In both methods to secure the grit from Figure 3-2, once cutting and thrust forces were above 20 N either the epoxy was likely to fail or fracture occurred. The forces reached that magnitude because the grit was in contact with the workpiece across about a 0.8 mm width, which created a large chip area. The epoxy failed in tension while the shear stress direction of the epoxy could resist larger forces.

The tensile stress was a direction that lifted the grit from the surface of the holders and the shear stress was in a direction that moved the grit around the mounting surface. For adhesives in general, tensile stress may also be more specifically referred to as peel or cleavage stress for oblique forces with respect to the adhesive layer. Most epoxies have a high shear strength and low tensile strength. The cutting forces employed on the grit were not pure tension or shear but a combination. It was determined that epoxy alone did not have the necessary strength to hold the grit and a different design was needed to constrain the grit.

4 GRIT GEOMETRY FOR FORCE AND WEAR EXPERIMENTS

4.1 GRIT GEOMETRY

As mentioned in the grinding background, the shaped grits are mounted on coated abrasive product with the tip of a triangular surface upright, but the precise placement and orientation is uncontrolled. Refer back to Figure 2-1 for the grits in the random orientation on a coated abrasive. To represent the alignment for possible mounting, the grit was tested at two

extreme grit orientations and one intermediate orientation. The testing orientation also provided an experimental basis for an optimal grit placement. The two extreme grit orientations, shown in Figure 4-1, could create either a zero rake angle or a negative rake angle with respect to the workpiece. Although grit irregularities may not provide a perfect 0° or -30° rake angle, the general rake angle was referenced to distinguish the orientation. Further explanations of the rake angles are described further in Sections 4.3 to 4.5.

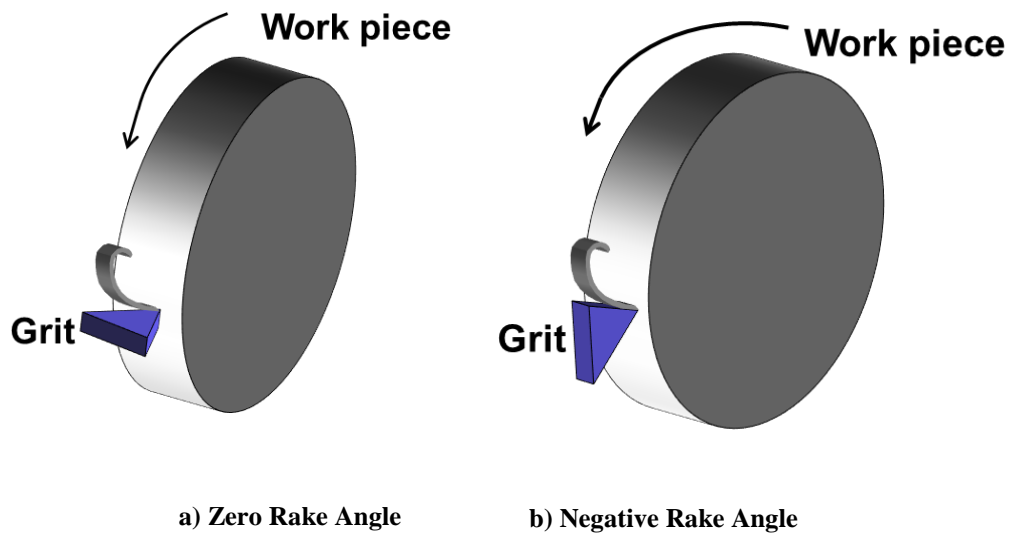


Figure 4-1. Extreme Grit Orientations

4.2 TOOL HOLDER DESIGN

Developing a method to support an individual grit (only 1.3 mm along each side) was an important part of the project. A repeatable mounting technique was needed for grit placement for grits that varied slightly in size. For simplicity the grit holder was equipped with two perpendicular faces to ensure the grit was laid flat and flush against the faces as shown in Figure 4-2. The perpendicular faces ensured grit orientation with respect to the large triangular face and edge of the grit. Originally only a clamping system was used when developing the holder design. However, a firm clamp was found to induce extra stress on the

grit that could result in fracture after attachment. Also a clamp alone would not provide sufficient torsional support for a grit with an irregular surface.

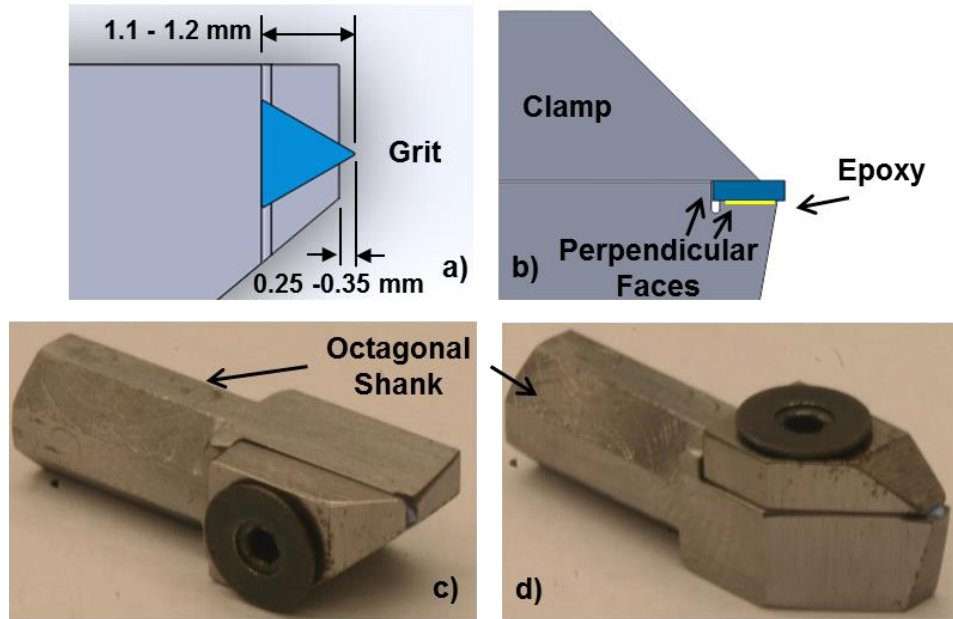


Figure 4-2. Tool Holder: a) Top view and, b) Side view of grit placement with respect to the perpendicular holder surfaces and epoxy placement. c) Grit holder in the negative rake orientation and, d) the Zero rake orientation

The final tool holder used both epoxy and a clamp to hold the grit in place shown in Figure 4-2. The clamp held the grit in compression, resisting possible tensile forces where the epoxy was weak. The epoxy was used to resist twisting and slip in the clamp and would act as shear stress on the epoxy.

The resulting mount left an exposed tip of the grit that hung over the edge of the holder for use in cutting experimentation. The grit extended past the tool holder 0.25 mm to 0.35 mm based on grit size and manual placement as shown in Figure 4-2. The grit was considered unusable when it didn't overhang the edge of the mount. The holder shank also had an octagonal shape to orient the grit at the different grit orientations on a coated abrasive. The

extreme orientations, previously shown in Figure 4-1, could be achieved as well as a position in between the extremes at 45° . The grit orientations changed the tool rake angle as discussed in the following sections.

4.3 NEGATIVE RAKE ANGLE ORIENTATION

The negative rake angle orientation had a nominal rake angle of -30° and was oriented with respect to the workpiece shown in Figure 4-3. It is important to note that the rake angle could be larger than -30° due to localized geometry such as an extremely blunt grit. The center of the grit was vertically aligned with the center of the spindle and workpiece.

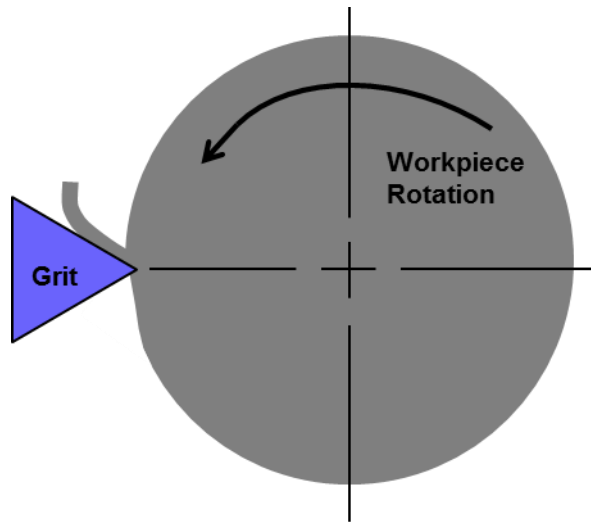


Figure 4-3. Negative rake angle orientation

The negative rake angle geometry was nominally a $300\ \mu\text{m}$ wide tool which could vary depending on the specific grit shape. Figure 4-4a shows a relatively flat grit which would cut along most of the width, depending on the depth of cut. Conversely Figure 4-4b shows irregular geometry with a high spot which results in a narrow contact area that changes as the depth of cut increases. Large irregularities in the grit width for this orientation made the contact area variable for different grit experiments.

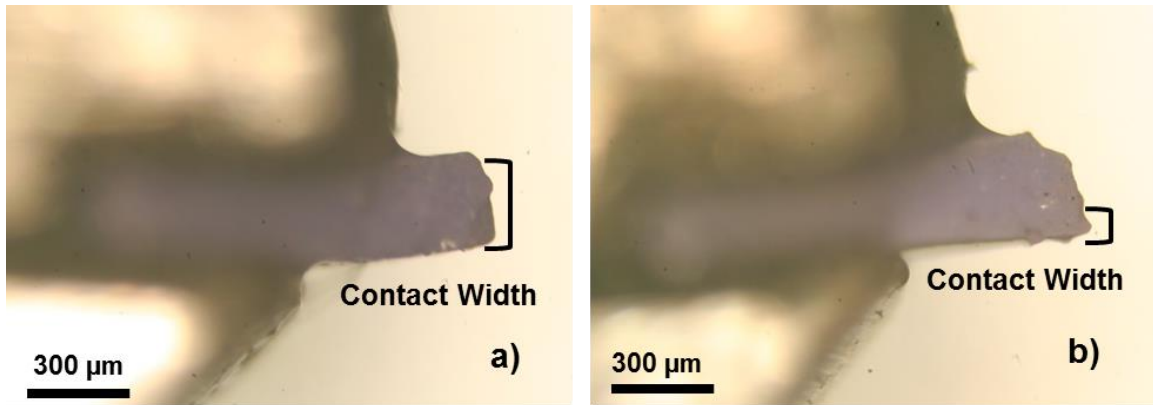


Figure 4-4. Microscope Image of Grit Contact Width for Negative Rake Orientation

4.4 ZERO RAKE ANGLE ORIENTATION

The zero rake orientation had the triangular surface of the grit as the rake face. The overall rake angle, excluding any localized geometry differences, created a zero degree rake angle, shown in Figure 4-5. As with the negative rake orientation, a large cutting edge radius would change the localized rake angle. Another factor that could influence the localized rake angle is if the grit had any characteristics resembling a chamfered or curved edge. However, care was taken in experiments to select grits without such characteristics. The grit cutting edge was aligned to the vertical center of the spindle.

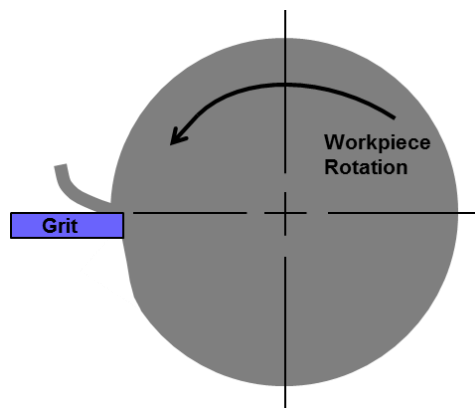


Figure 4-5. Zero rake angle orientation

The tool width in contact with the workpiece had variability between grits, but it was much more repeatable than the negative rake orientation. The average grit had a triangular tip with about a 60° angle before any wear occurred. The variability of the rake face geometry of two different grits is illustrated in Figure 4-6.

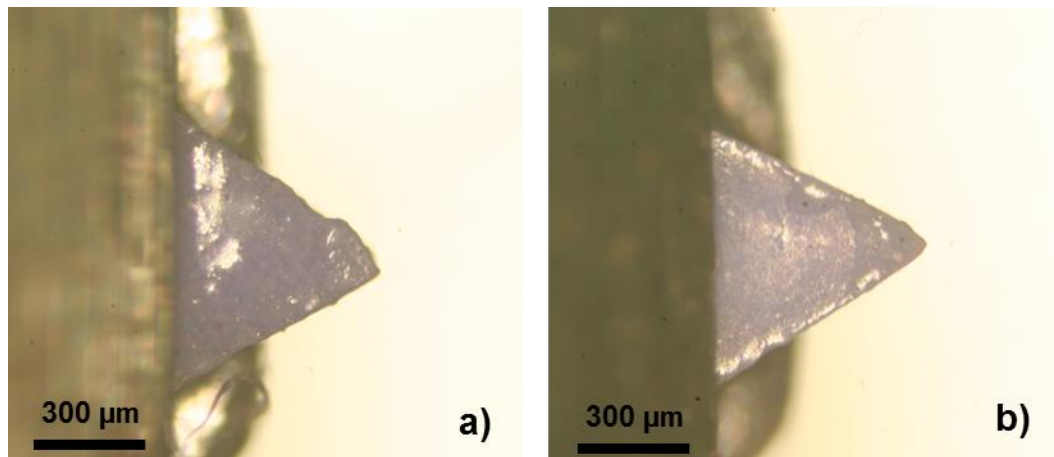


Figure 4-6. Microscope Image of Two Grit Rake Faces for the Zero Rake Orientation

The contact width of the zero rake grits was dependent on the depth of cut. As the depth of cut increased so did the contact width as the triangular edges were moved further into the workpiece. The grits shown in Figure 4-6 were the same grits from Figure 4-4 but in the perspective of the triangular face which is the rake face for the zero rake orientation. The zero rake orientation could be slightly rotated to assist in high speed imaging of the grit. The modified orientation and impact on the video system is described in Section 5.5.2.

4.5 HALFWAY RAKE ANGLE

The halfway rake angle is oriented with the tool holder halfway between the zero and negative rake orientation. The cutting geometry is different from the two previous orientations and the rake faces are now oblique with respect to the cutting direction. To illustrate the two effective oblique rake angles, Figure 4-7 shows two perspectives of the grit.

The arrows represent the material flow along the faces of the grit. The arrow labeled “a” shows the material flow on the rectangular face while the arrow labeled “b” shows the material flow along triangular face. The arrow labeled “a” is on the rake face of the negative rake angle orientation and “b” is on the rake face of the zero rake angle orientation. The left section of Figure 4-7 shows the rake faces from the perspective of the cutting direction while the right gives a top down perspective.

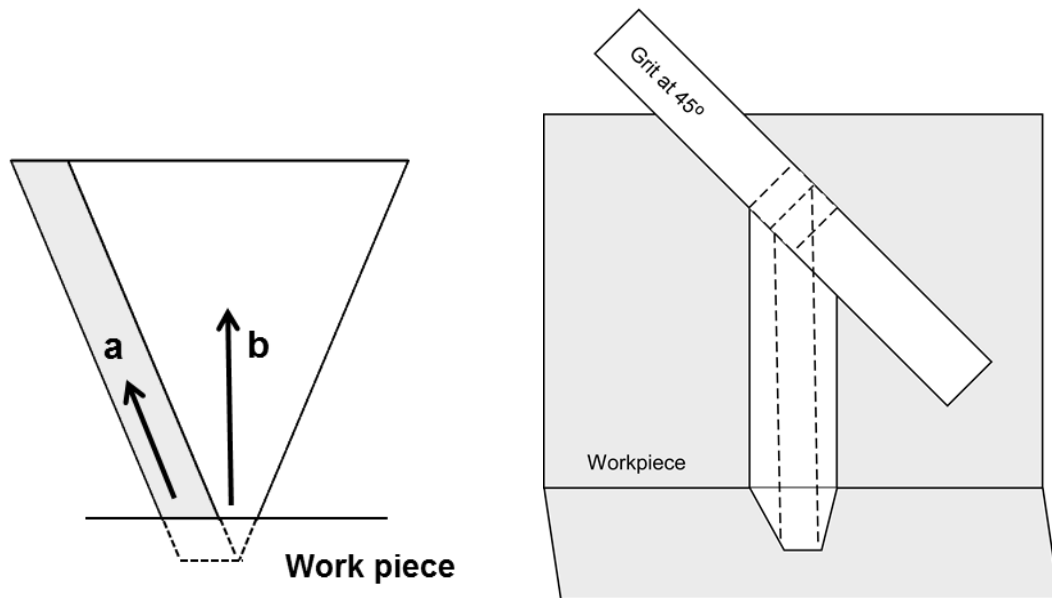


Figure 4-7. Halfway Rake Orientation Oblique Rake Faces: Orthogonal to Cutting Direction (left), Top Perspective (right)

The characteristics of the halfway rake are a combination of the zero and negative rake orientations. An experimental comparison between the rake angles are given in Section 7.3.

5 GRIT CUTTING ASSESSMENT WITH FORCES AND IMAGING

5.1 BACKGROUND AND FORCES

Cutting forces can communicate important information about the cutting process. In diamond turning applications, where very sharp cutting edges are used, the cutting and thrust

forces can be monitored to determine when the workpiece surface finished degrades. The cutting and thrust forces can be related to a model for certain parameters to determine tool edge geometry, as described by Drescher [4] and Arcona [5,28]. This is important with precision machining when the surface finish of a part is a critical parameter. However, after initial experiments it was found that the cutting forces for the alumina grit could not be used to characterize wear with diverse grit geometry.

However, Section 5 was based on the assumption that the grit would cut and wear similarly to orthogonal machining conditions and tools. It was expected that the resulting cutting would produce a steady state force with small variation between experiments due to grit geometry. However results showed that unlike orthogonal machining, there was not a precise steady state force or wear rate. The following sections describe the experiments and results that motivated the development of measurement techniques to compare experimental results described in Section 6.2. The following section describes the process and challenges of using forces to characterize grit cutting.

5.1.1 FEED DIRECTION

The two main cutting methods that were used for cutting experiments were a plunge and a traverse cut. Figure 5-1 illustrates the two methods. In the plunge cut, the tool was fed in the radial direction of the workpiece while the workpiece rotated, but not moving in any other direction. The experiment was characterized by a constant depth of cut and a tool width that increased as the tool plunged further into the workpiece. The increase in tool width was due to non-uniform geometries and high spots. The traverse feed described when the tool was fed along the outer surface of the workpiece or traversed along the workpiece axis. The experiment was characterized by a controlled width and depth of cut. The width of the cut was determined by the traverse feed and only used a small region of the grit to actively removed material. Each technique was used for different objectives and is described in each respective section of experiments. As the experimental procedure progressed, the two cutting methods were eventually combined.

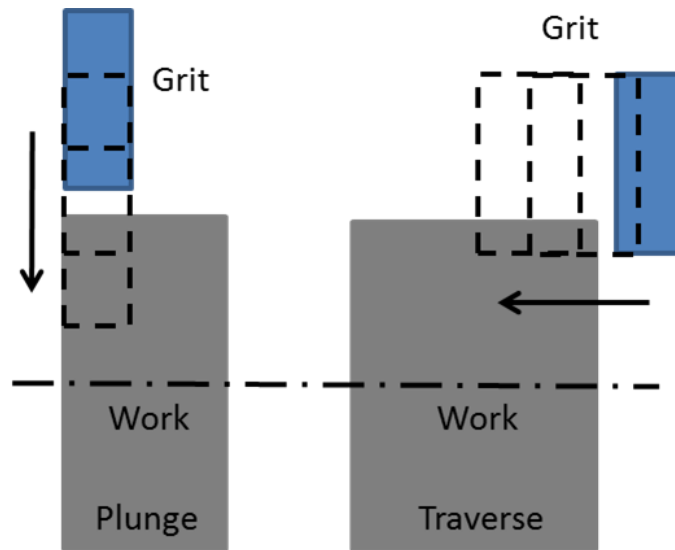


Figure 5-1. Feed Directions

5.1.2 GENERAL EXPERIMENTAL PROCEDURE

The workpieces were prepared prior to experiments by machining with a carbide tool for a consistent surface finish. The feed rate was related to a theoretical surface roughness of 0.1 μm PV (peak to valley). However, it was discovered that the carbide tool and feed rate produced a PV of 1-3 μm for steel workpieces. The geometry of a new carbide tool had a 400 μm nose radius. The cutting speed for each experiment was determined by the spindle speed and workpiece diameter. The workpiece diameter was measured for each experiment and the spindle speed set to the surface speeds described in the experimental results.

5.2 TRAVERSE EXPERIMENTS AND CHARACTERISTICS

The first set of experiments used a traverse feed to move the tool across the workpiece. The traverse feed determined how quickly the grit passed over the surface in the axial direction. For this method the grit had no radial feed but was positioned at a set depth of cut, unless the tool wore. The workpiece moved along its cylindrical axis and rotated as shown in Figure 5-2. The depth of cut was changed for separate experiments to systematically test the grits. The traverse feed determined the contact width of the grit. If the traverse feed was low

enough to produce overlapping cuts, the contact width of the grit used to remove material was determined by the feed distance per revolution of the workpiece. However, if the geometry of the grit was larger than the feed, it could potentially rub the surface that was just cut. If the grit was an irregular shape, the contact area could be at any point along the grit. Overlapping tool paths were used before groove geometry was measured. In most cases, the traverse feed experiment provided a more consistent and controlled workpiece removal rate in than the plunge experiment.

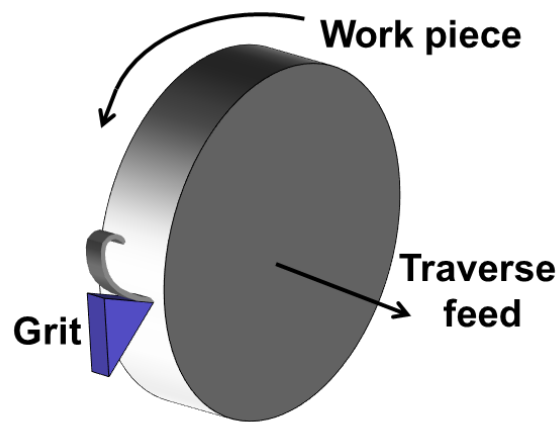


Figure 5-2. Traverse Feed Experimental Representation

5.2.1 TRAVERSE CUT GRIT EXPERIMENTS

The original traverse cut experiment was conducted with a single grit that was used for consecutive experiments. The grit was used until it extended past the tool holder less than 50-100 μm . The depth of cut was set before the experiment began, but the depth of cut could vary if the grit wore, broke or accumulated material pick up at the interface. Grit fracture events and material pickup did occur. After each experiment was performed, the workpiece was faced off with a carbide tool to create a flat surface. Pictures of the grit profile were taken after major fracture events to correlate wear and forces but also to determine common fracture characteristics.

The experiments in Sections 5.2.2 and 5.2.3 were performed with a surface speed of 1 m/s and a traverse cutting feed of 2.38 mm/min. This traverse feed resulted in overlapping tool paths by 12 $\mu\text{m}/\text{rev}$. This only used about 4 % of the 330 μm nominal grit width to remove material for the negative rake orientation. For certain grit geometries, the region of the grit width that was not removing material could rub the workpiece and influence forces. This included grits with flat edges or a large edge radius. Each traverse experiment could potentially reach a cutting distance up to 20 m but could be shortened by fracture or wear.

5.2.2 TRAVERSE CUT CASE STUDY AT THE ZERO RAKE ORIENTATION

The zero rake orientation, described in Section 4.4, was used in a traverse experiment on 304 SS material. Experiments were performed with a surface speed of 1 m/s and a traverse cutting feed of 2.38 mm/min. A traverse feed of that magnitude resulted in overlapping tool paths that corresponded to about 12 $\mu\text{m}/\text{rev}$. There were several cases in which a grit sustained no distinguishable fractures, even after several experimental cutting lengths of 20 m.

Each individual cutting test produced mostly constant forces, averaging at 1.9 N and 1.8 N for cutting and thrust. All experiments were conducted on a single grit at a set 5 μm depth of cut. The average forces and standard deviations are given in Figure 5-3. The data in Figure 5-3 demonstrates the average cutting and thrust forces over the course of eighteen consecutive cuts before the grit fractured beyond use and the first experiment started with an unused grit. Fractures that stopped individual cutting tests early occurred at experiments represented by data points at 180m, 211m and 330m. The same grit was used after the fractures occurred. The experiments had similar cutting and thrust forces. The standard deviation, especially for the thrust force, increased drastically at 232m shortly after a fracture occurred.

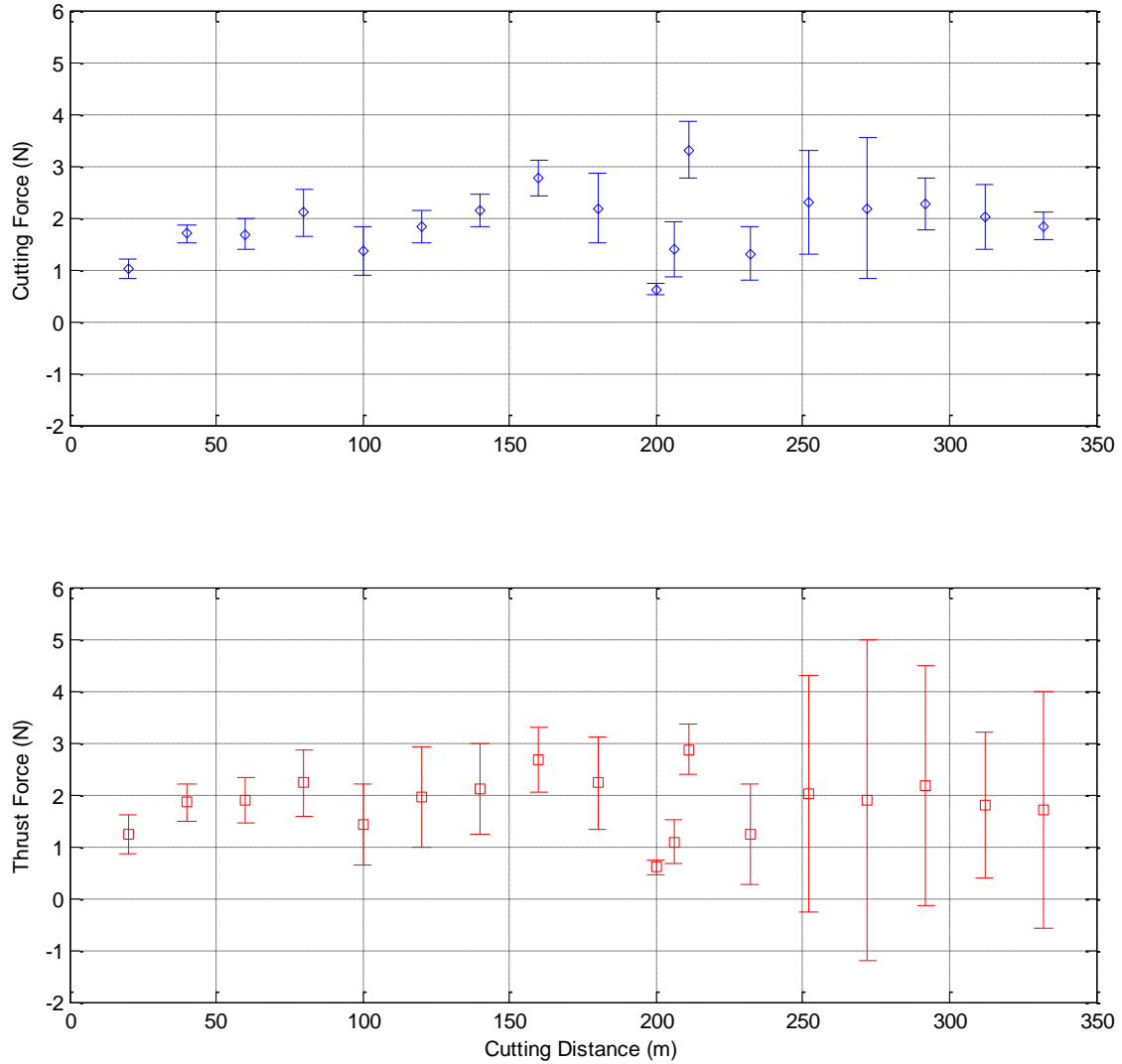


Figure 5-3. Zero Rake: Consecutive Traverse Tests at 5 μ m Depth, 1 m/s Speed, and 12 μ m Feed Using a Single Grit on 304 SS

Data points from Figure 5-3 either represent an average force during a single experiment, or several data points representing distinct forces in a single experiment. For instance, experiments that had distinguishable periods of constant force differences, similar to Figure 5-4, were separated into two force averages. Values at 205 m and 211m in Figure 5-3 are representative of the individual experiment in Figure 5-4 where the average forces from 0 to

6 m and 6 to 13 m in Figure 5-4 were averaged. Material pickup at the cutting interface was hypothesized to be the cause of the rise in forces at 6 m and 13 m in Figure 5-4. The combination of the forces and high speed video that support this hypothesis is given in Section 5.4.3. The experiment eventually ended in a grit fracture at a 10 N cutting force and 8 N thrust force.

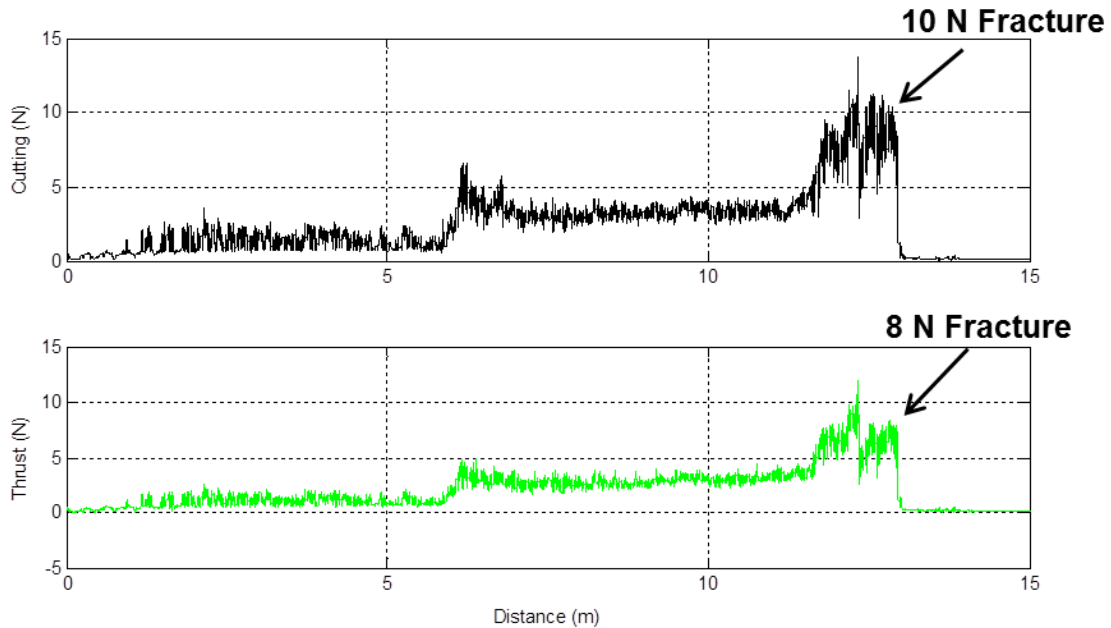


Figure 5-4. Traverse Experiment at 5 μm Depth and 1 m/s for a Zero Rake Grit on 304 SS

Although the forces and standard deviation changed in the experiments, there was nothing to relate the results to, other than assuming the geometry must have arbitrarily changed at fracture. The lack of understanding of cutting geometry involved with the experiments in Figure 5-3 motivated improved experiments described in Section 6.2.

5.2.3 TRAVERSE CUT CASE STUDY AT THE NEGATIVE RAKE ORIENTATION

The negative rake angle orientation, described in Section 4.3, was tested with the same traverse feed parameters described in Section 5.2.1. Experiments were performed with a

surface speed of 1 m/s and a traverse cutting feed of 2.38 mm/min. A traverse feed of that magnitude resulted in overlapping tool paths that corresponded to about 12 $\mu\text{m}/\text{rev}$. The experiments consisted of a series of experiments at both 5 μm and 10 μm depths of cut. The negative rake angle orientation proved to expedite fracture events and had significantly shorter periods of continuous cutting compared to the zero rake orientation. A combination of new grits and grits that had recently fractured were used in the experiments. Experiments for the negative rake orientation had highly variable forces as shown in Figure 5-5.

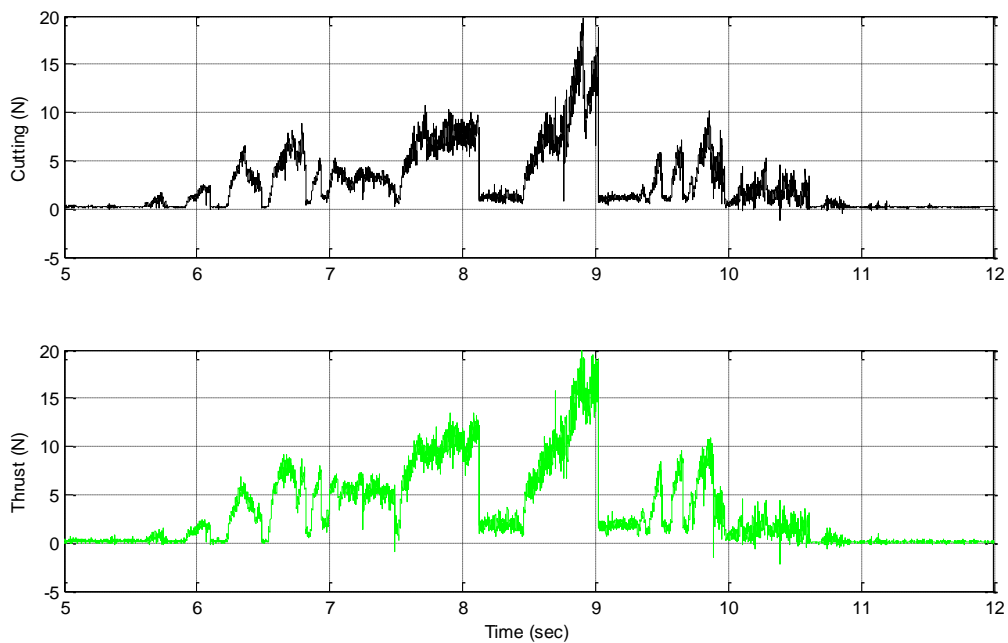


Figure 5-5. Sample Negative Rake Angle Traverse Experiment at a 12 μm Feed and 1 m/s Speed on 304 SS

The irregularity of forces during experiments on the negative rake grit has been partly attributed to material pickup. Visual evidence of material pickup recorded with the high speed video system is described in Section 5.4.3. The data for each trial ended when the grit stopped contacting the workpiece due to a fracture. The overall average force and standard deviation of each test run is given in Figure 5-6 and Figure 5-7 for two grits, one at 5 μm and

one at 10 μm depth of cut. The average force was calculated by averaging all the force data of a single experiment pass, effectively taking an average force for all of Figure 5-5. There were no cases of distinct force differences in an individual experiment like was shown in Figure 5-4.

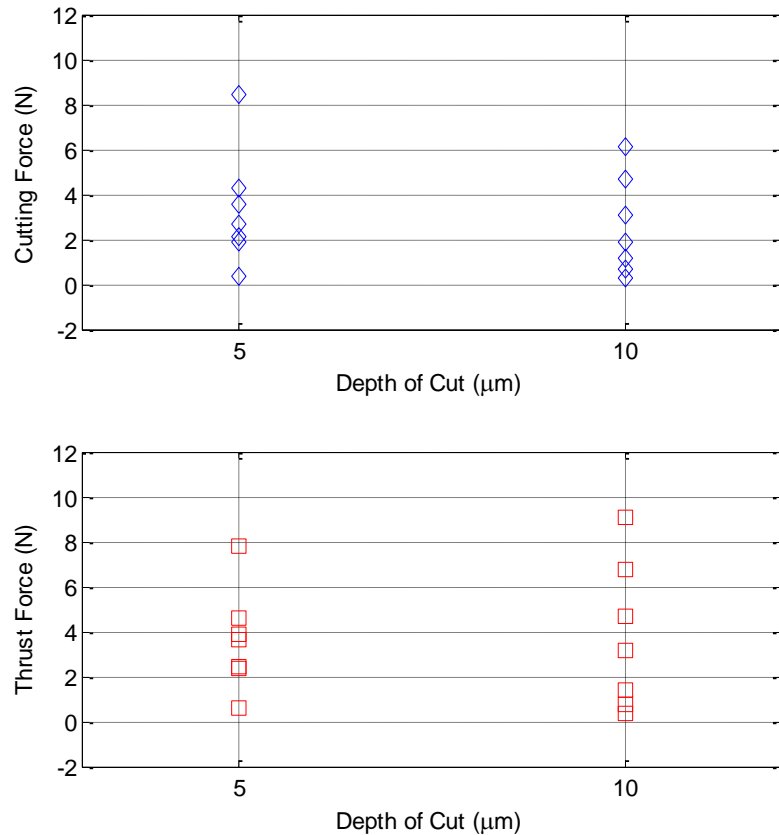


Figure 5-6. Average Cutting and Thrust Forces for Negative Rake Angle Traverse Experiments at a 12 μm Feed and 1 m/s Speed on 304SS

The standard deviation was often larger than the average force due to the large force fluctuations demonstrated in Figure 5-5. The standard deviation data given in Figure 5-7 shows the 5 μm depth experiments, which are the seven experiments shown to the right of the 5 μm mark, and the 10 μm experiments, shown by the five experiments to the right of the

10 μm mark. Consecutive experiments were plotted for each grit (at 5 μm or 10 μm depth of cut). As the grit wore and fractured, the variation of experimental forces increased. The variation was attributed to the effect of fracture and material pickup in combination with the grit geometry changing. Even though the two grits were tested with separate depths of cut, 5 μm and 10 μm , there was no direct correlation between forces and depth of cut. Out of the twelve experiments between the two depths of cut there may have been an average force, but it was indistinguishable with the amount of variation and sample size tested.

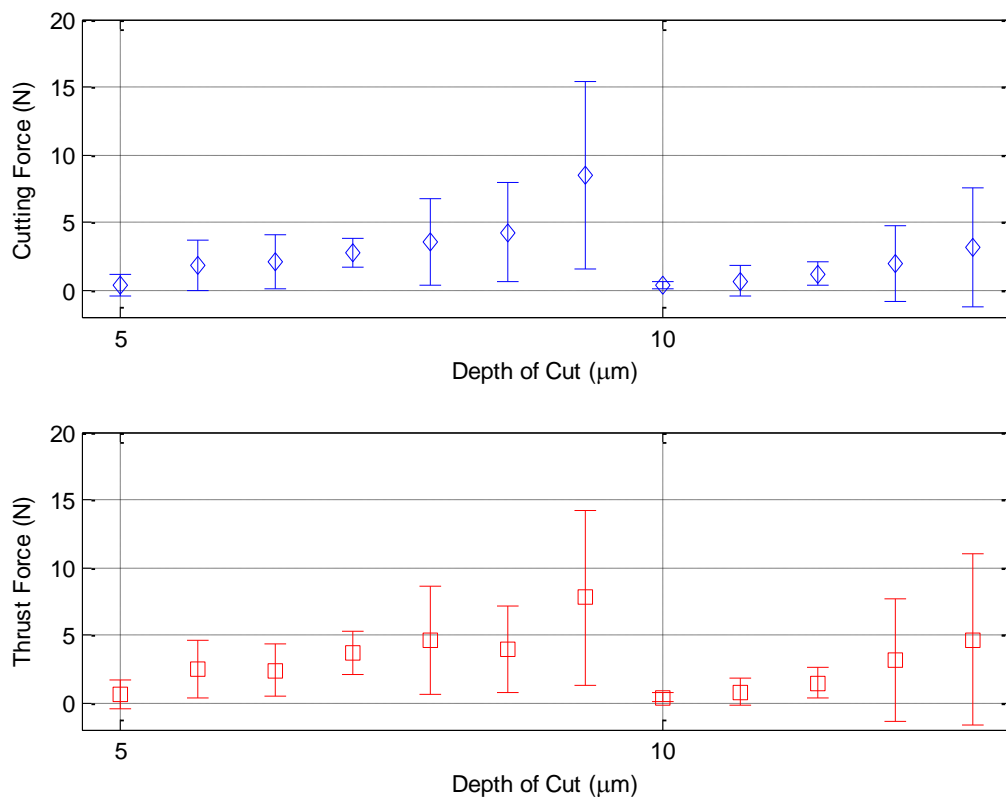


Figure 5-7. Standard Deviation for Cutting and Thrust Forces at 5 μm and 10 μm Depths for Negative Rake Angle Traverse at 12 μm Feed and 1 m/s Speed on 304SS

For each test run the maximum force, in Figure 5-8, was much larger than the average force in Figure 5-6. Figure 5-8 shows the maximum force from each experiment in the negative

rake Traverse experiments. The maximum force did not follow any type of trend but often resulted in a grit fracture. Figure 5-8 shows the cutting and thrust forces for thirteen experiments that lead to fracture. The experiments were for 5 μm and 10 μm depth of cut but there is no correlation between the depth and the fracture forces. The variation in the maximum forces could have been due to variable strength grits in conjunction with material pick up. The variance in forces due to material pickup is discussed further in the use of the video imaging system in Section 5.4.3.

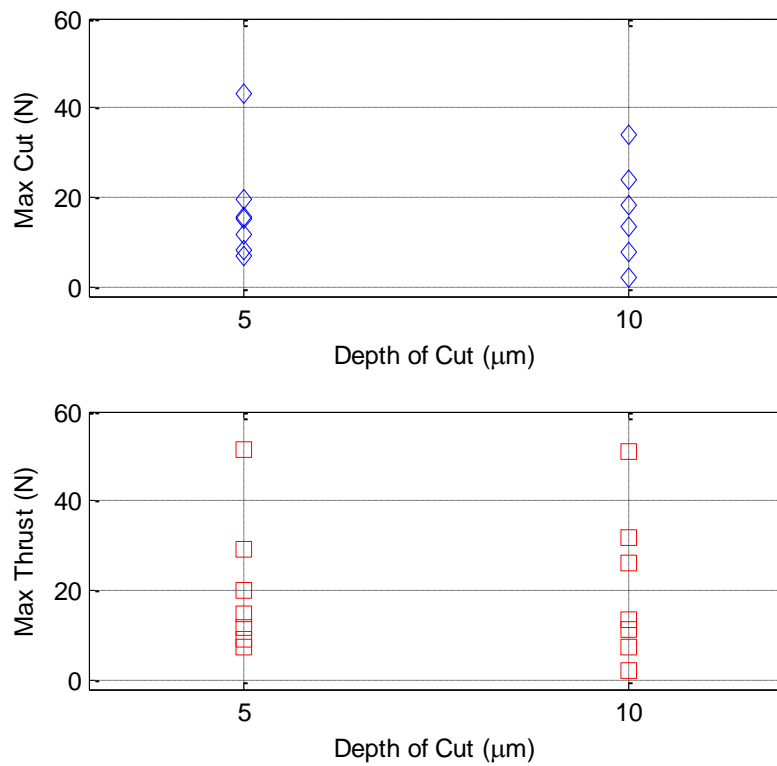


Figure 5-8. Maximum Forces for the Negative Rake Traverse Experiments at a 12 μm Feed and 1 m/s Speed on 304SS

To compare experimental force data with consistency further hypothesis were made regarding the effect of material pickup on forces. In several instances the raw force data

showed points in time which the forces appeared to drop to a steady state value. It was hypothesized that the apparent steady state forces were a base force in which there was no material pickup on the tool. If the hypothesis was correct then material pickup on the tool would go through dynamic states of accumulation on the tool followed by a rapid knocking loose of the material. The rapid change to the base force is highlighted in Figure 5-9, originally shown as Figure 5-5. The base force was a short steady state region in the force data that lasted nearly a second in some cases. The base forces were distinguished by the repetitive and seemingly steady force signature.

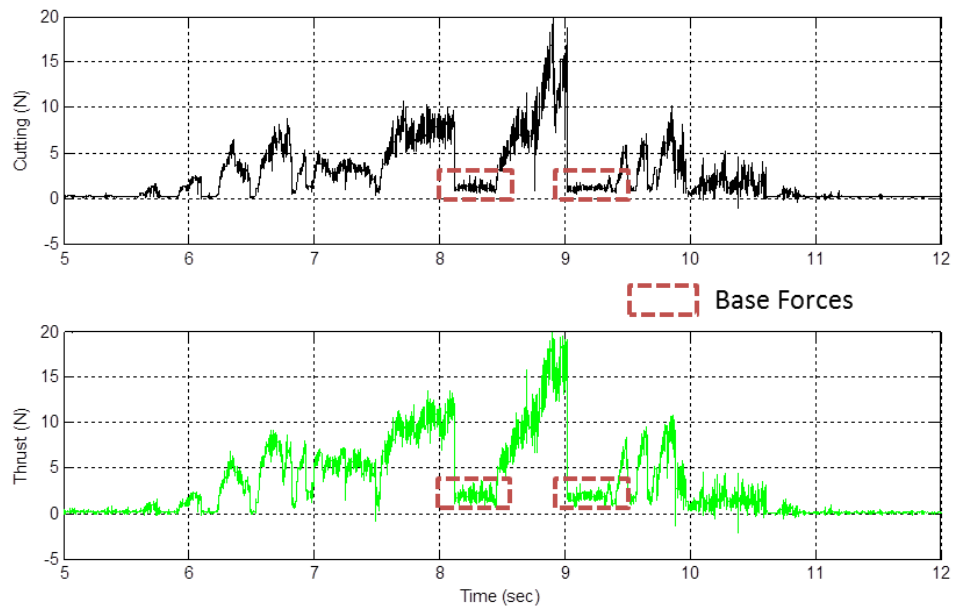


Figure 5-9. 5 μm Depth, Negative Rake Angle: Experimental Data and Base Forces

The base force data for the negative rake angle experimental data was extracted from several experiments and plotted in Figure 5-10. The base forces were present for three of the seven experiments from the 5 μm depth of cut data and four of the five experiments for the 10 μm depth.

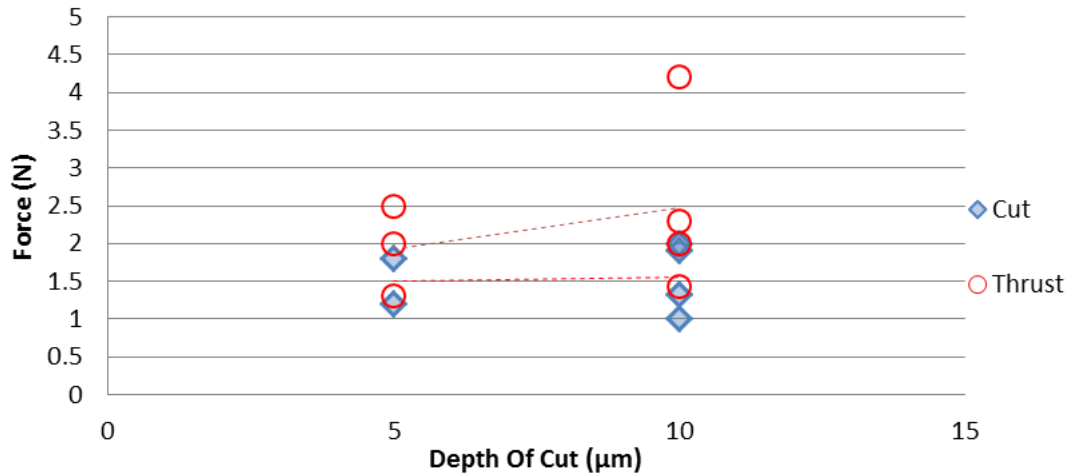


Figure 5-10. Negative Rake Traverse Experiment Base Forces at 12 μm Feed and 1 m/s Speed on 304 SS

Experiment forces were not steady state but rather were characterized by rapidly changing forces leading to fracture. Further methods to characterize forces were explored as described in Sections 6 and 7.

5.2.4 TRAVERSE CUT SUMMARY

The traverse experiments with two grit orientations could be directly compared since a single traverse feed rate was used. The negative rake angle base forces were compared to the zero rake experiments at a 5 μm depth of cut. The forces for both experimental cases were within the same general range but the notable difference was that the negative rake orientation had a lower cutting to thrust force ratio. When comparing only the average force of each experimental orientation (not considering base forces for the negative rake) the negative rake angle average forces were much higher at a 4.8 N and 5 N cut and thrust compared to the zero rake at 1.9 N and 1.8 N cut and thrust. However the grit orientations were influenced by different tool geometry. Recall that the cutting geometry for the zero rake orientation had a nominal 20 μm nose radius while the negative rake orientation had a nominal width of 300 μm .

The overall result of the traverse cutting experiments in both the zero and negative rake orientations was that the experimental data could not be easily related between similar experiments. In fact the actual grit geometry that participated in cutting was unknown. The experimental results revealed the need to define the cutting geometry for each orientation. Defining geometry will improve the basis for which forces can be compared. Later experimental procedures that clarified cutting forces by measuring the grit groove geometry are given in Section 6.

A further outcome of initial experimentation was general grit characteristics were observed which provided initial steps for further testing. A qualitative difference between the orientations was that the negative rake orientation had frequent force spikes which many times resulted in fracture while the zero rake orientation was much more consistent. Another characteristic taken for further experimentation was to use much larger traverse feed rates or non-overlapping traverses. The larger feed rates had a twofold purpose. The first was so tool grooves could be identified but also to increase the overall removed material. The Traverse experiments had a theoretical removed chip area of less than $150 \mu\text{m}^2$ in all conditions and having a larger removed chip area would provide more distinguishable forces between experiments of different parameters.

5.3 PLUNGE EXPERIMENTS AND CHARACTERISTICS

For the plunge cut shown in Figure 5-11 the grit moved radially into the workpiece at a set feed rate and workpiece speed. This produced a nominal depth of cut as long as no wear or fracture occurred. The plunge experiment differs from the traverse experiment in that it has no traverse feed so the entire width of the grit contacts the workpiece material.

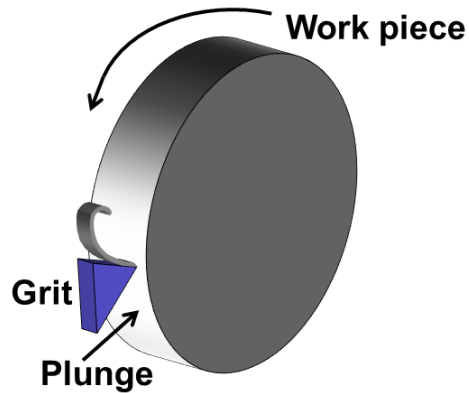


Figure 5-11. Plunge Cut Experiment Representation

The grit depth of cut was set by advancing the grit a specific distance into the workpiece for each revolution. After the first workpiece revolution the depth of cut was constant as the grit advanced further into the workpiece. In most cases the entire contact width of the grit was used to cut the workpiece in the plunge experiments. However, if the end of the grit was not flat, the contact area would grow over several workpiece revolutions. The grit contact area for the end of a non-uniform grit is shown in Figure 5-12 as the grit advanced further in the radial direction of the workpiece.

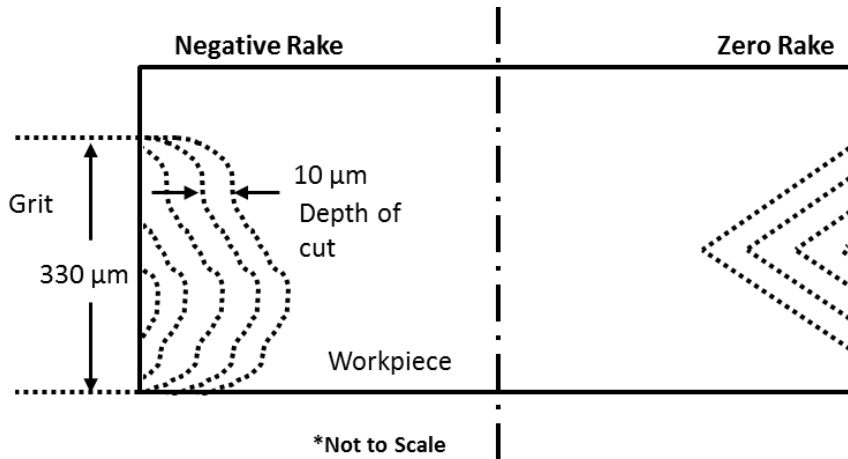


Figure 5-12. Grit Contact Area for Plunge Experiment in the Extreme Orientations

After the entire width of the grit contacted the workpiece, the forces should be able to reach a point in equilibrium for the negative rake orientation. However, the zero rake orientation forces would not reach a steady state. As the grit would feed into the workpiece a larger area of the triangular face would contact the workpiece and cause higher forces. The zero rake orientation was not used for plunge experiments for this reason.

An important benefit of the plunge cut was that a small fracture did not result in the end of the experiment since the grit continued to feed into the workpiece. A fracture would stop cutting for a short period of time until the grit fed into the workpiece the distance of the fracture and contacted the workpiece material again. However, a large fracture would stop cutting if the fracture reduced the grit size more than the overall plunge distance or total depth of the experiment.

5.3.1 PLUNGE CUT GRIT EXPERIMENTS FOR THE NEGATIVE RAKE ORIENTATION

The plunge cut experiments were conducted in the negative rake orientation on 304 SS. The negative rake plunge experiments were characterized by large force increases as cutting progressed into the workpiece. Often the experiments lasted only a few seconds before the forces increased rapidly and the grit fractured. In most cases a different grit was used in each experiment, there were a few exceptions when grits sustaining small fractures were reused for another experiment. The plunge cut experiments were set to feed the grit into the workpiece to create a 10 μm cutting depth. The depth may have varied due to uncontrolled material pickup on the grit, which would give a higher apparent depth of cut.

Figure 5-13 gives four experimental tests of the rise and drop in forces for the negative rake experiments. Each experiment shown in Figure 5-13 represents a different grit. Each experiment showed different force patterns when cutting 304 SS workpiece material with a 10 μm nominal depth of cut at a 0.1 m/s or 1 m/s cutting speed. In Figure 5-13a the force dropped to zero after a fracture occurred in the experiment before 0.5 s. The remaining section of the grit began cutting again right before 1.5 s. Figure 5-13b to Figure 5-13d showed forces for grits that varied due to material build up and small fractures. Fractures that only removed small sections of the grit active in removing material would result in a

drop in forces without completely stopping cutting. Alternatively a drop in forces could be due to material pickup falling away from the cutting interface. The difficulty of comparing multiple experiments is further shown in the figure. It was determined that the characteristic force rise in separate experiments did not follow a specific pattern. However, there was a qualitative characteristic rise in forces that was linked to material build up at the cutting interface. This was observed with the high speed imaging system described in Section 5.4.

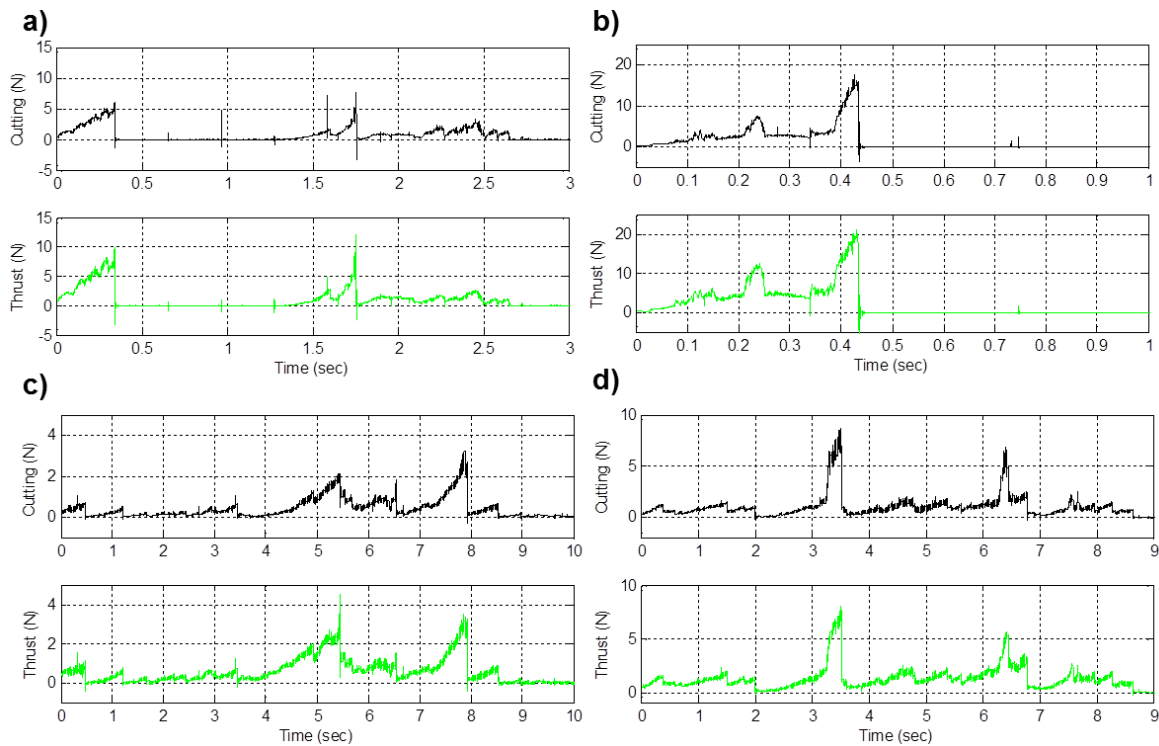


Figure 5-13. Negative Rake Plunge Experimental Forces for Four Experiments at 10 μm Depth of Cut on 304 SS: 1 m/s in a) and b) while 0.1 m/s in c) and d)

The average experimental forces for fourteen experiments at 0.1 m/s, 0.5 m/s, and 1 m/s speeds and at 10 μm depth of cut are given in Figure 5-14. The average force was calculated by taking the average force during a single experiment like was done with the negative rake traverse experiments. Much like the traverse experiments there was a large variation in

average forces as shown in Figure 5-15. The standard deviation plot is separated into the first six experiments at 0.1 m/s, six subsequent experiments at 0.5 m/s and the last two experiments at 1 m/s. Various cutting speeds were used in the plunge cut experiments to reduce motion blur and increase video quality using a shutter speed of 20 μ s. When speed was varied there was no distinguishable force trend. The average cutting force for all of the experiments was 2 N and the average thrust force was 2.5 N.

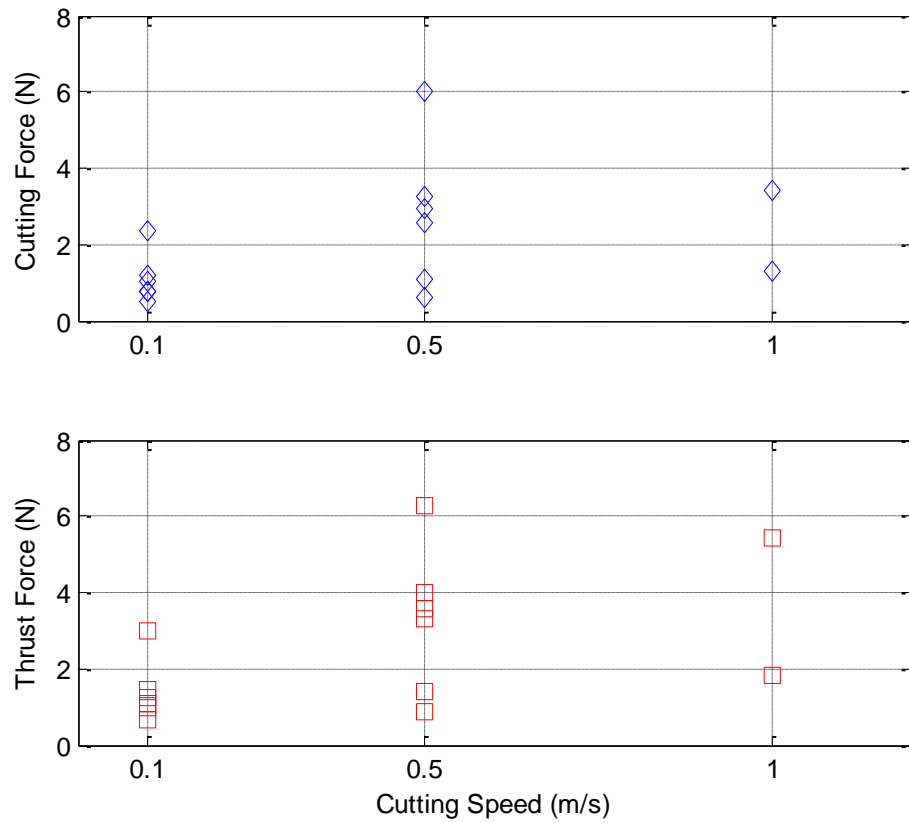


Figure 5-14. Average Forces for Negative Rake Plunge at 10 μ m Depth of Cut on 304 SS

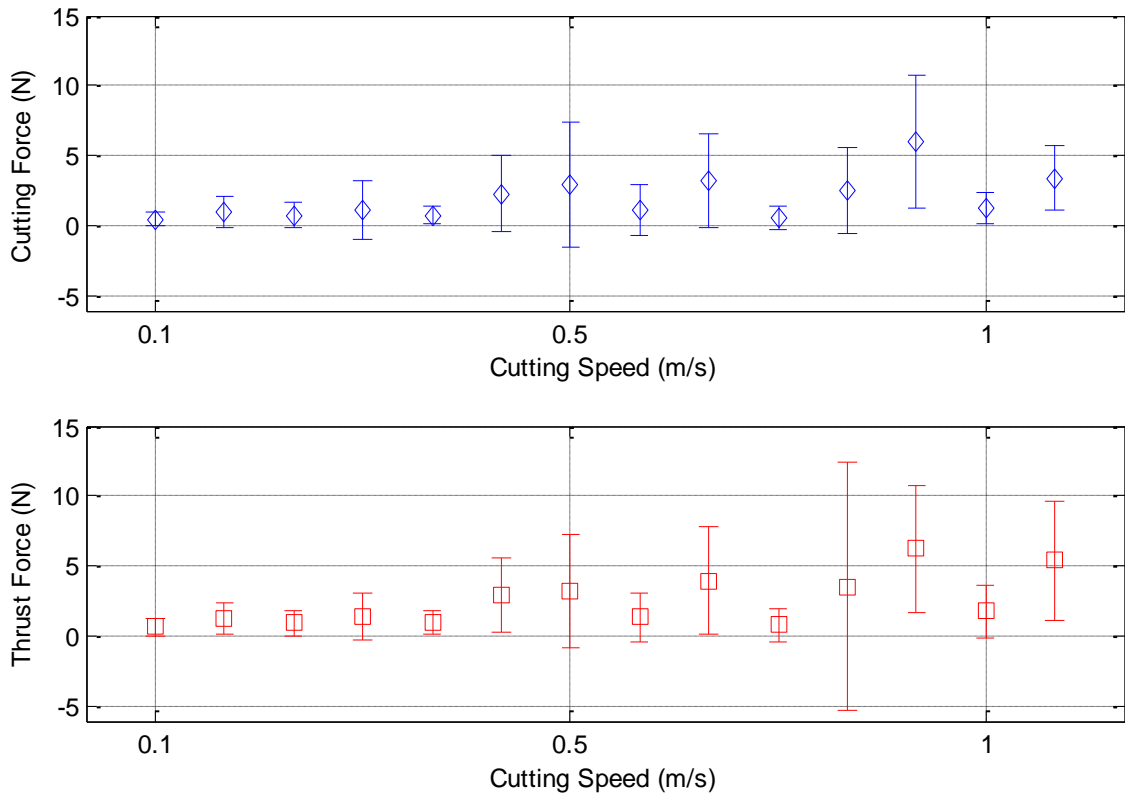


Figure 5-15. Average Force and Standard Deviation of Negative Rake Plunge at 10 μm Depth of Cut on 304 SS

The force plots of the plunge experiments from Figure 5-13 were characterized with consecutive fractures where fractures normally occurred at the maximum force. The maximum forces for the experiments are plotted in Figure 5-16. The large force difference illustrates that the nominal cutting parameters could not be used to explain the forces.

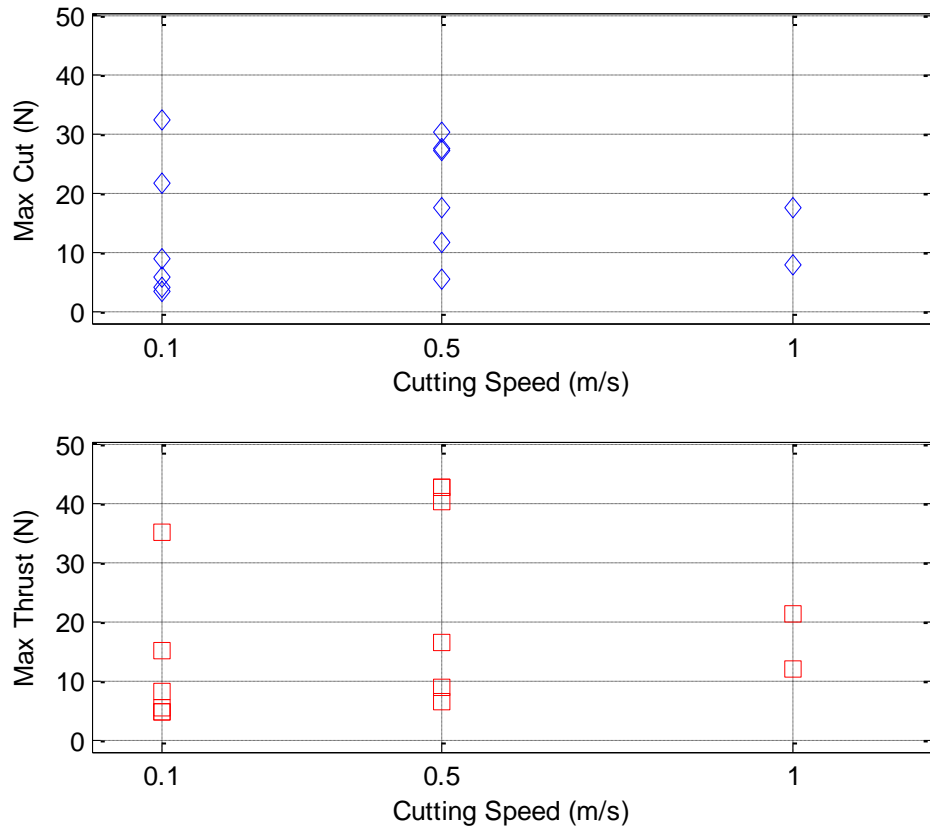


Figure 5-16. Maximum Forces for the Negative Rake Plunge Experiments at 10 μm Depth of Cut on 304 SS

5.4 HIGH SPEED CAMERA IMAGING

5.4.1 IN PROCESS VIDEO

Recording real time video and force data provided key insights to both grit fracture and cutting, especially events that happened in fractions of seconds. The video footage captured during the grit cutting had great value to it; however the resulting still frame images were of lower quality compared to similar stationary optical microscope images like Figure 4-4 and Figure 4-6. The value of the video was in the rapid accumulation of images at speeds up to 6006 FPS. The video and force measurements were triggered simultaneously when the thrust force signal reached 0.12 V which is equivalent to about 0.5 N. The force and video data were used to correlate effects of material build up, chip formation, and grit fracture. The

high speed video camera shutter speed was set to 20 μs for experiments. In a few experiments in Section 7 the shutter speed was set at 10 μs or 15 μs , where video quality permitted.

The traverse cut experiments produced overall poor video quality compared to the plunge cuts. The workpiece in traverse experiments was out of focus in most videos because it moved in the direction corresponding to the camera focal depth. This resulted in a blurred workpiece image and grit/workpiece contact in the majority of recorded videos. Plunge cut experiments were used to improve the video quality of grit cutting. The plunge cut enhanced cutting visualization because both the grit and workpiece were focused on the camera in the negative rake orientation. The front face of the grit was aligned with the front face of the workpiece by focusing the grit surface on the high speed video camera and then moving the workpiece axis until it was also in focus. This provided the best chance for a clear video of the grit/workpiece interaction. However, motion of the chips would sometimes obstruct the viewpoint of the tool and workpiece. Grit geometry also had a pronounced impact on the video image quality as discussed in the following sections.

5.4.2 VIEW OF GRIT AND FOCAL DEPTH

The quality of the video image is influenced by the depth of field of the camera. The depth of field is a measurement of how much an object would appear to be in focus. The optical lens' relatively small focal depth, $\pm 15 \mu\text{m}$, in comparison to the geometry of the grit created issues with capturing focused images. Grit orientation played a big role in recording focused video, drastically changing the video quality. A still picture taken from the video camera at the extreme grit orientations is shown in Figure 5-17. A grit representation is provided to clarify the orientation. The viewing window of the camera was 440 μm by 330 μm which showed most of the grit that overhung the holder. In all video images the workpiece is shown on the right moving down, corresponding to a counter clockwise spindle direction. This resulted in the chip formation on the top side of the grit, or top side of the localized geometry.

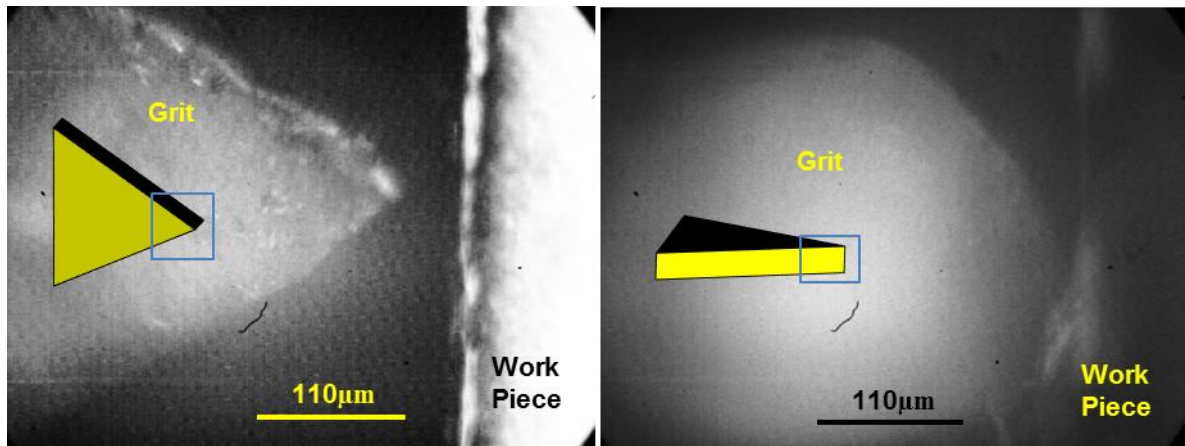


Figure 5-17. 42x Grit Video at 20 μ s Shutter Speed: Negative Rake (left), Zero Rake (right)

The negative rake orientation provided a flat, broad face for the focal plane of the video image. Video and images taken during cutting provided a view of events that happened on the front triangular face of the grit. However, the grit width, about 300 μ m for the negative rake orientation, was much larger than the focal depth of the optics. This limited the camera focus to the front surface of the grit and only events that were happening near the front surface could be recorded. Inferences on material build up and chip formation along the entire cutting width of the tool contact was not possible.

The 30° angle of the face of the zero rake orientation resulted in a blurred outline of the grit. The zero rake images were focused on a diagonal edge running through the depth of field, and only a blurred outline of the rounded top edge could be seen. With either orientation the camera was focused on the tip of the grit so part of the contact area of the grit was recorded; camera focusing techniques are provided in Appendix 10.2. Even though the entire grit may not be in focus in the zero rake orientation, the cutting interface and chip formation would be recorded with careful focus on the potential contact region.

Figure 5-18 shows a negative rake oriented grit that was focused on the front face but does not appear to be in contact with the workpiece. The grit was in contact with the workpiece at some point which was out of the focal plane. The grit geometry has been outlined to assist

visualization of the cutting contact region which could not be seen. Although the grit was in focus, the workpiece contact was not, preventing a view of the chip formation. While grits with this type were not ideal candidates for chip video, they may be beneficial for capturing grit fracture if it occurs at the front of the grit. Further optimization of the grit imaging is given in Section 5.5.

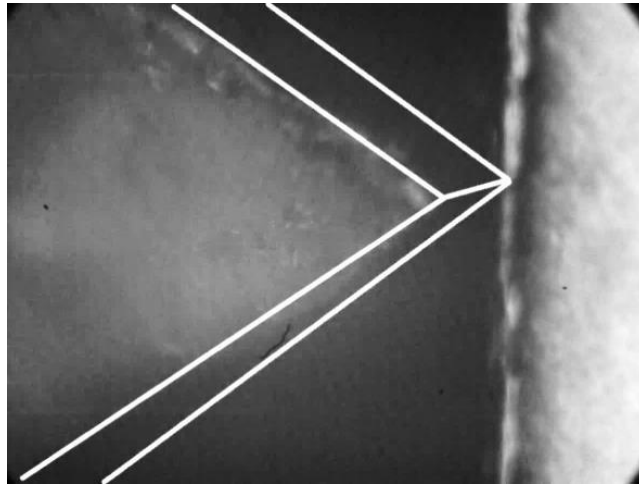


Figure 5-18. Grit Variation and Focal Depth at 20 μ s Shutter Speed

5.4.3 MATERIAL BUILD UP AND CHIP FORMATION

Qualitative observations of the chip formation and fluctuation were observed during the experiments. Quantitative observations on chip speed were made and related to the shear angle in Section 7.5. The view of the chip was sometimes unclear due to motion blur or the chip flowing out of the view of the camera. When the chips moved into and out of focus it sometimes showed different aspects of the chip. Some serrated edges were observed on the chip, but such detail was only viable for general observations. The videos sometimes showed continuous chip formation but would also lead to events where material and chips clustered together and obstructed the cutting interface. Figure 5-19 demonstrates both chip formation and material build up.

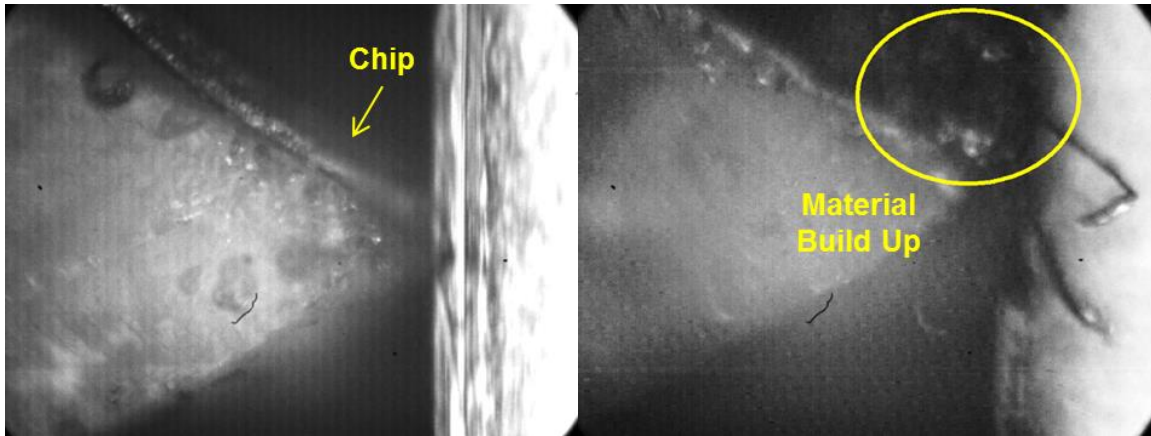


Figure 5-19. Chip Formation (left) and Material Build Up (right)

Chip formation varied slightly based on grit orientation. In most cases of the negative rake orientation, shown in Figure 5-19, the chip had a defined side edge that was in line with the triangular face of the grit. The chip also has a slight rounded top to it which is out of focus of most videos. The zero rake orientation chips were generally a triangular shape with a vertex pointing away from the grit rake face. The vertex of the chip was in line with the tip of the grit that was removing material. In most videos of the zero rake orientation only the tip of the chip was in focus but it depended on the focusing location. Camera focusing techniques for each orientation is given in Appendix 10.2.

The material build up in Figure 5-19 sometimes appeared to completely stop all chip flow in the view of the camera. It was not clear if chip formation had completely stopped or if chip formation was out of the view of the camera. The high speed imaging system aided in recognizing some characteristics in the forces. Several key videos showed the chip flow accumulated, ceased, or slowed down; followed by an increase in forces. However all force rises were not validated by a video that showed the chip flow stop or accumulate. The videos that did not show chip flow, but documented a rise in force, were attributed to the event happening out of the view of the high speed camera.

Figure 5-20 shows a negative rake plunge at 0.5 m/s with 10 μm depth of cut when a chip was flowing freely in Figure 5-20a, but the chip formation started to slow down and broaden before leading to it being relatively stationary in Figure 5-20b. Shortly thereafter, the chip built up at the cutting interface and a fracture occurred. The built up chip can be recognized in the still frames by noting that there is a dark empty space above the chip in Figure 5-20a, while Figure 5-20b shows material surrounding the entire cutting interface.

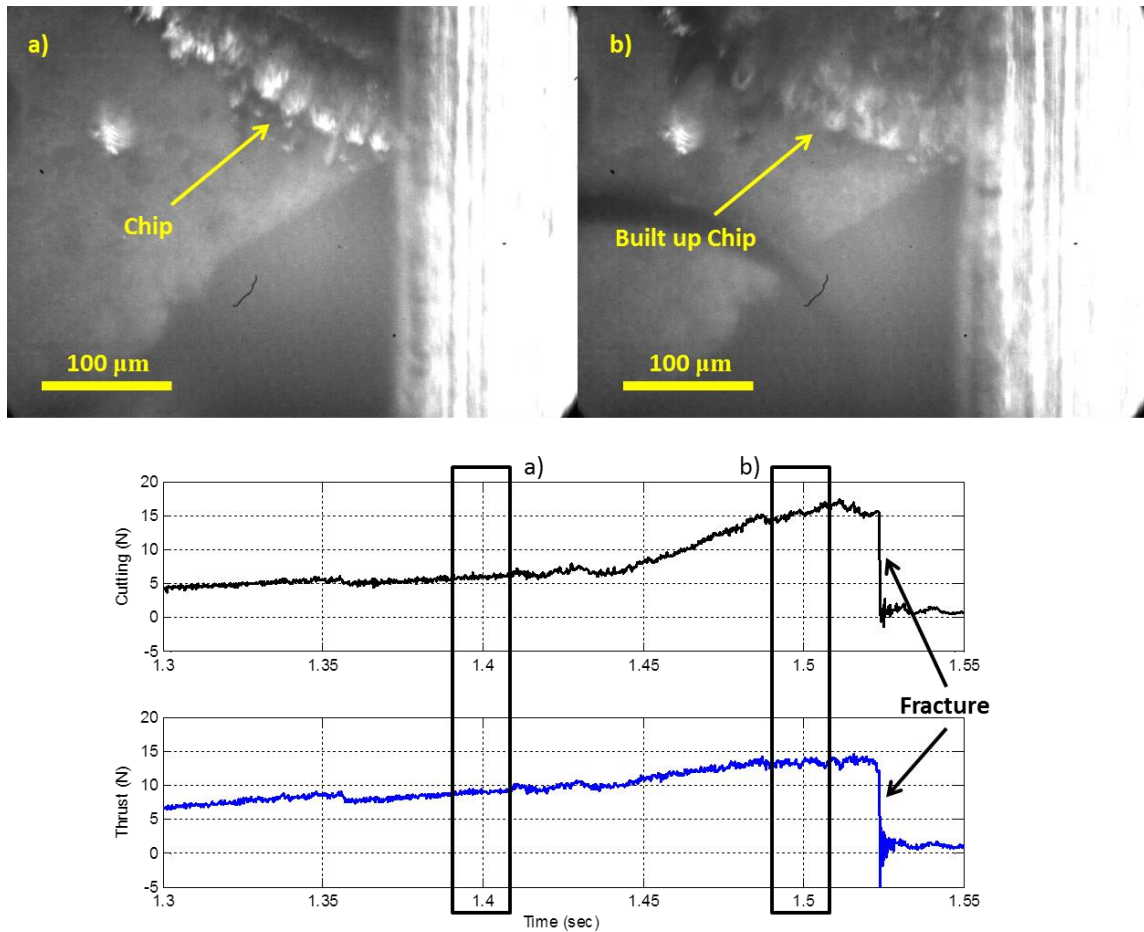


Figure 5-20. Material Build Up and Resulting Force Increase

Figure 5-21 shows images from a 0.5 m/s cut at a 10 μm depth of cut. Figure 5-21a shows chip progression which was out of focus on the camera and barely seen, but the material

eventually built up in Figure 5-21b. A chip then began to flow from the apparent location of the built up material in Figure 5-21c and Figure 5-21d. However, the material once again began to build up in Figure 5-21e and Figure 5-21f before a fracture occurred, shown by the large drop in forces.

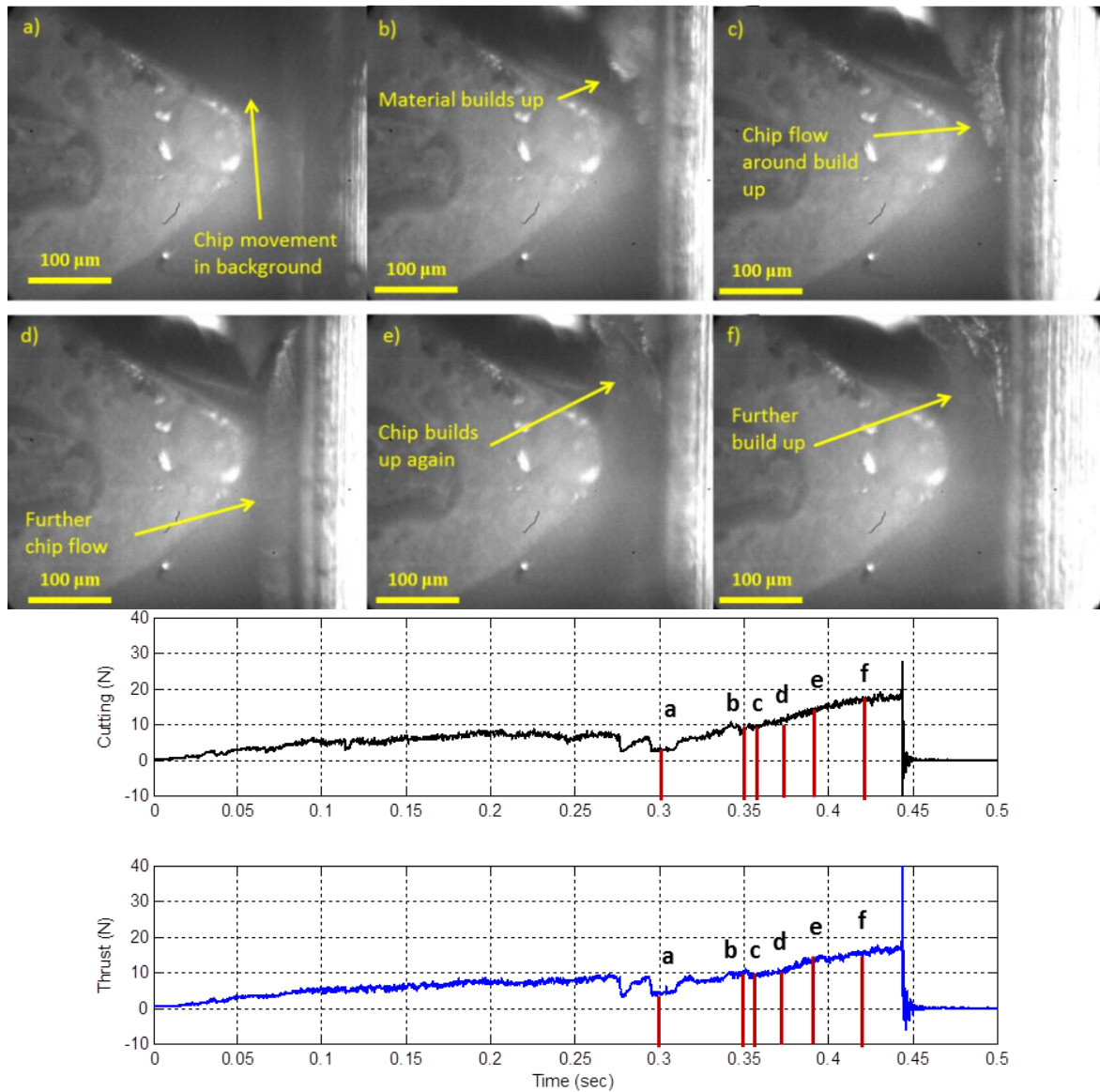


Figure 5-21. Buildup progression of a Negative Rake Plunge at 10 μm Depth and 0.5 m/s Speed on 304 SS at time: a) 0.300 s, b) 0.350 s, c) 0.353 s, d) 0.368s , e) 0.389 s, f) 0.420 s

Figure 5-20 and Figure 5-21 illustrated chip build up cases that resulted in fracture; however this was not always the case as shown in Figure 5-22. Here the material built up produced a rise in forces and then fell away. It was a 1 m/s cut at 2.5 μ m depth. The chip is partially seen in Figure 5-22a and it accumulated at the cutting interface in Figure 5-22b. Eventually the clump of material fell away from the cutting interface at Figure 5-22c and a chip continued to form in Figure 5-22d. The chip in Figure 5-22d was partially out of range of the camera so it was blurred and is hard to see in a still frame image. The conditions that lead to chip build up that fell away from the cutting interface were unknown. However these experiments showed that material build up or chip accumulation at the cutting interface could cause the forces to rise which could lead to fracture.

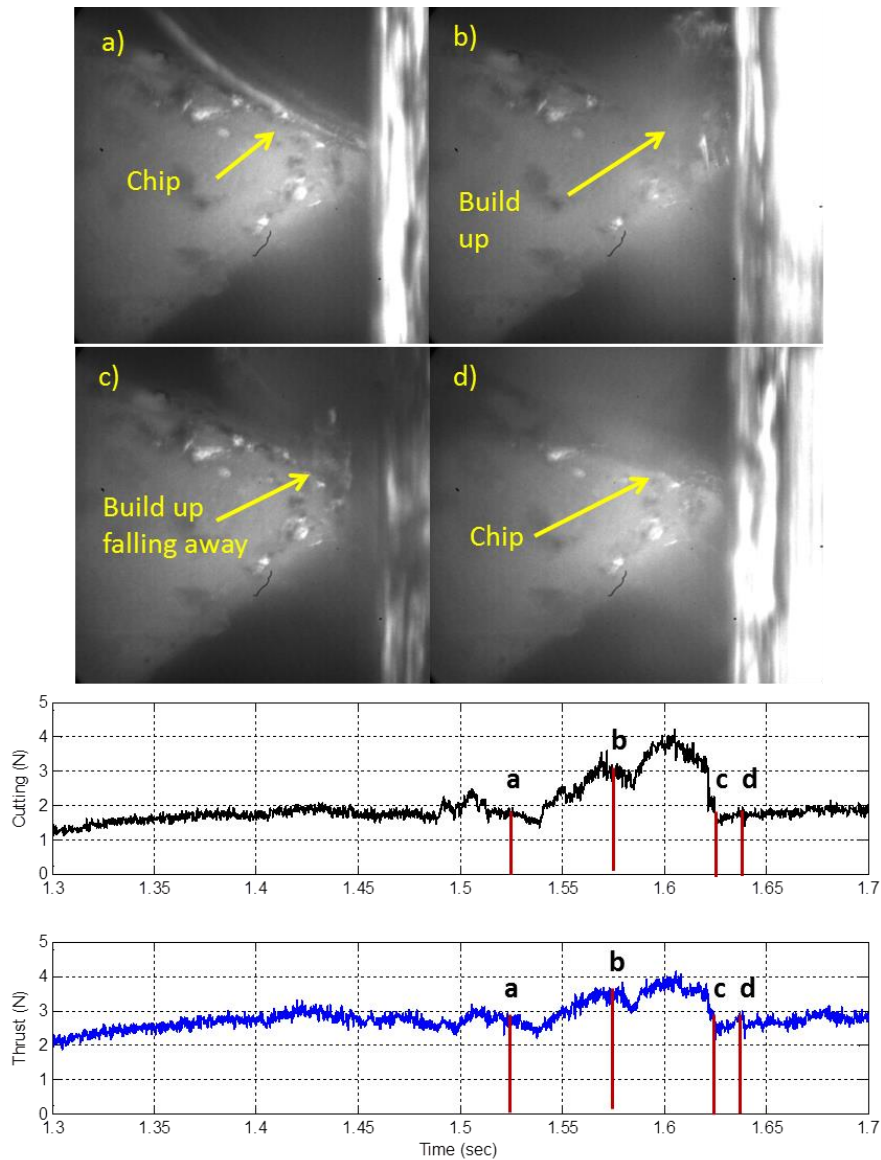


Figure 5-22. Buildup progression of a Negative Rake Plunge at 2.5 μm Depth and 1 m/s Speed on 304 SS at time: a) 1.524 s, b) 1.575 s, c) 1.625 s, d) 1.637 s

5.4.4 HIGH SPEED VIDEO CONCLUSIONS

The plunge cuts provided good cutting images and showed many cases of chip build up and fracture. The chip build up at the cutting interface was found to raise forces which could lead to fracture of the grit. The highly variable cutting conditions and possibility of material build

up and fracture demonstrated how inconsistent similar experiments appeared. Although the grit geometry and parameters had some impact on individual results with the experimental setup, the impact was indistinguishable when only using forces and video to characterize cutting. To understand the grit cutting process work was done to better define the actual cutting conditions, such as how much material was removed. This would also assist in obtaining quantifiable results.

5.5 GRIT PREPARATION FOR VISUALIZATION

5.5.1 GRIT PRE-SELECTION

Over the course of experimentation, it was observed that certain grit characteristics permitted better visualization. The best video was produced by grits that had a flat triangular face, a uniform width, and a small cutting edge radius between the face and width. The flat face allowed a large part of the grit to be in 30 μm depth of focus of the video system. To maximize the quality of the video, grits with these characteristics were selected.

A sharp cutting edge on the front face of the grit produced a chip formation that was more likely to be within the depth of field of the camera. The chip could change directions and thicknesses throughout the video but having a clear view of the interface would ultimately lead to a better understanding of cutting. However the sharp front cutting edge did not always keep the chip formation uniform and the chip could still impede the camera view.

5.5.2 GRIT SURFACE PREPARATION AND POLISHING

Instead of just selecting the best grits for use, grits could be physically altered to improved video quality. Several grits were polished by hand with fine grain sandpaper to improve the front surface of grits but it also rounded the edges. A more efficient method of polishing the grit surface was performed by an outside company using techniques already developed. The polishing made the grit significantly thinner but had a visually bright and flat front surface. The polished grits were then selected for the sharp cutting edges to create videos with crisp edges and bright surfaces. The video clarity for the polished grit is shown in Figure 5-23.

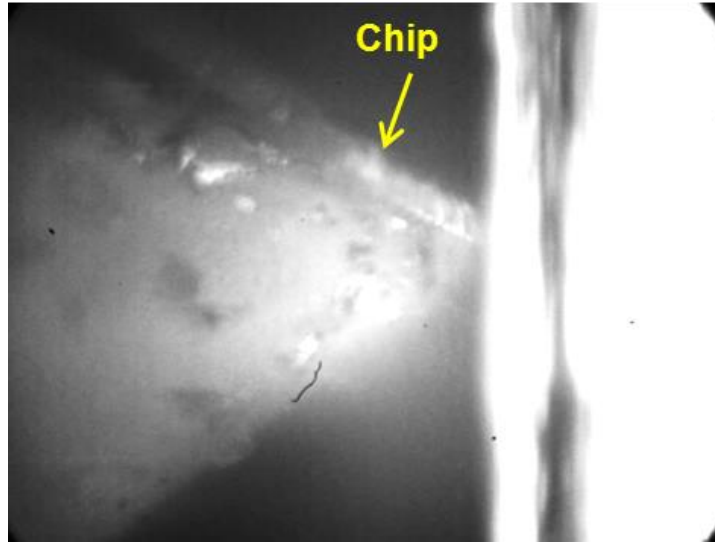


Figure 5-23. Polished Grit Cutting 304 SS at 1 m/s

However, no amount of polishing improved the quality of the grits at the zero rake angle orientation. The zero rake angle grits were imaged by looking at the diagonal side where most of the grit was out of focus. To improve on the zero rake orientation, the grit was manually rotated in the tool holder. Thus the bottom surface of the grit on the left in Figure 5-24 was close to parallel to the camera, shown in the image on the right. The slight change in grit orientation provided a method for recording video of the zero rake cut. The rotation did not change the zero rake angle but could have changed how the grit width interacted with the material flow and chip shape. The altered zero rake orientation was only used in experiments to determine the effect on visual quality. The resulting forces were similar to experiments in Section 5.3.

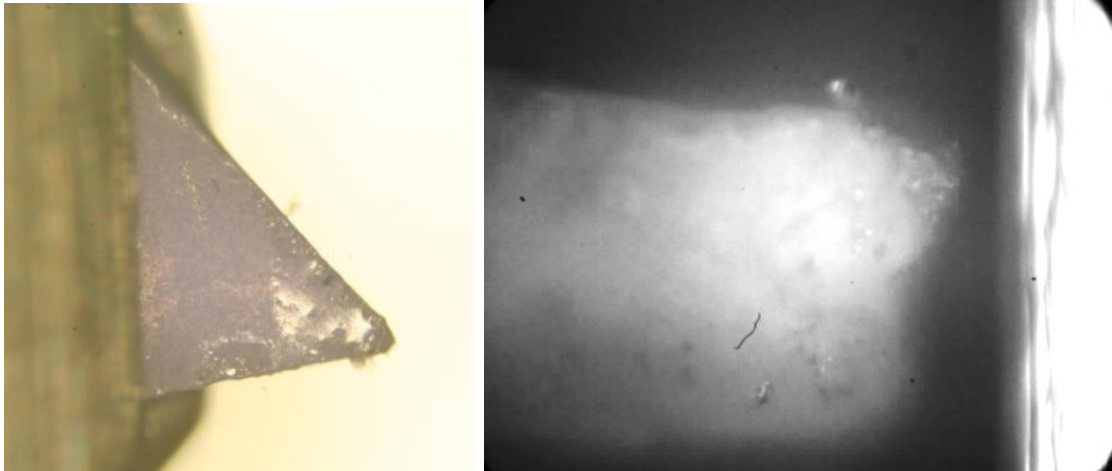


Figure 5-24. Grit at Zero Rake Orientation: Top down view of the rake face (left), Video Image of the side of the grit (right)

5.5.3 CUTTING INTERFACE PREPARATION

Another method to prepare the grit for cutting videos was to prepare the cutting edge of the grit in a method similar to the dressing of a grinding wheel. The technique used depth of cuts under $2.5\ \mu\text{m}$ to shape the cutting edge of the grit into a flat surface. The grit was traversed across the width of the 304 SS workpiece in the negative rake orientation at slow feed rates to wear the grit flat and avoid large scale fracture. The traverse cuts had a depth of cut of $1\text{--}2.5\ \mu\text{m}$, a feed of $2.95\ \text{mm/min}$ or $5.91\ \text{mm/min}$ and a surface speed of $2.5\ \text{m/s}$ or $5\ \text{m/s}$. Both feed rates and surface speed corresponded to a feed that was about $15\ \mu\text{m/rev}$. The small depths of cut and traverse feed slowly wore the tool without inducing large scale fracture. Figure 5-25 shows the gradual wear of the high spot of a grit into a relatively flat cutting edge after multiple low depths of cut passes.



Figure 5-25. Grit Wear Shaping Method: Original (left), after seven passes (right)

The goal of the cutting interface was to prepare a more uniform cutting edge instead of selecting a flat grit. However, the cutting interface shaping was abandoned as a viable technique due to the time and effort needed to shape the grit. It was determined that a similar effect of improving the cutting videos was obtained by using the previous technique of grit selection and was a more practical method to improve video quality.

6 DEFINING GRIT CUTTING GEOMETRY

6.1 TOOL FORCE MODEL

6.1.1 MOTIVATION

The first experimental sequence in Section 5 described the challenges of comparing experimental parameters to unknown grit geometry. Tool force models were used as a guide to further define forces. In many models the forces were calculated based on contact areas and geometries of a tool. The challenge was that the geometry of each grit was unknown, so Section 6 sought methods to define contact geometry during each experiment.

Tool force models were used to approximate grit cutting mechanisms that occur in grinding. However, the models are only as accurate as they were able to represent grinding characteristics and how grits interact on a grinding wheel. Chen [19] describes a model for grinding by using a spherical grit. His model expands on an assumption by Shaw in representing grits as a spherical shape. The model approximates the cutting and friction

actions on a grit by relating the contact to an indentation force, similar to the force in a Brinell or Meyer hardness test. However this model depends on the grit shape and in the case of the shaped abrasive grits in this study, a simple spherical model would not be sufficient. A tool force model for single point turning applications and based on tool geometry was developed by Drescher [4] and further expanded by Arcona [5,28]. The model uses the tool geometries and workpiece properties to predict forces using modeled relationships of material springback and friction. The Arcona model was also used in force predictions in a ball end milling operation by Miller [29]. In the context of this thesis, the Arcona model was used as a guideline to develop measurement techniques and methods to compare cutting and thrust forces.

6.1.2 ARCONA TOOL FORCE MODEL DESCRIPTION

The Arcona model makes three major assumptions. “First, the material is regarded as elastic-perfectly plastic. Second, the normal stress acting on the shear zone, σ_s , is taken as the uniaxial material flow stress, or one-third the material hardness. Finally, a von Mises failure criterion is employed so that the shear stress, τ_s , is given by Equation (6-1) [5].”

$$\tau_s = \frac{\sigma_s}{\sqrt{3}} \quad (6-1)$$

The tool geometries, workpiece hardness, modulus of elasticity, friction, and shear angle are needed for a model prediction. The cutting and thrust forces are given in Equations (6-2) and (6-3).

$$F_c = \frac{HA_c}{3} \left(\frac{\cot(\alpha)}{\sqrt{3}} + 1 \right) + \mu_f A_f \left(0.62H \sqrt{\frac{43H}{E}} \right) \quad (6-2)$$

$$F_t = \mu \frac{HA_c}{3} \left(\frac{\cot(\alpha)}{\sqrt{3}} + 1 \right) + A_f \left(0.62H \sqrt{\frac{43H}{E}} \right) \quad (6-3)$$

where

H = hardness of workpiece material (GPa)

E = elastic modulus of the workpiece material

A_c = face area of chip (removed chip area)

A_f = flank contact area of the tool

μ = friction coefficient at the interface between the rake face of the tool and the workpiece

μ_f = friction coefficient at the interface between the flank face of the tool and workpiece

α = shear angle of the chip

F_c = cutting force

F_t = thrust force

A sketch of the geometry and force components for the Arcona cutting model is given in Figure 6-1. The cutting force is made up of the force of the material on the chip face area, F_{Ac} , and the friction force from the flank area, μF_{Af} , while the thrust force is the elastic springback force on the flank contact area of the tool, F_{Af} , and the friction force from the chip face area, $\mu_f F_{Af}$.

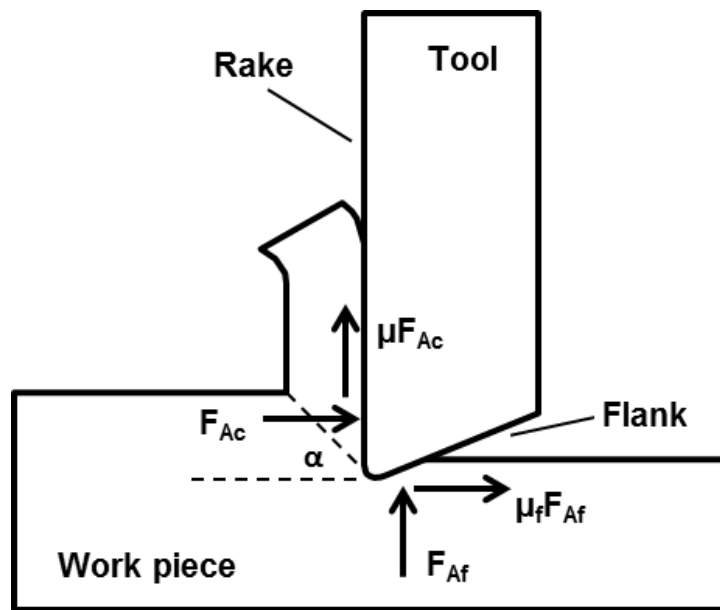


Figure 6-1. Sketch of forces for the Arcona model

The material properties in the Arcona model are not related to operating conditions such as speed or temperature. The workpiece and chip speeds could indirectly affect the flank and rake face friction factors or even workpiece material properties. The actual values of the friction coefficients are unknown and are the only largely undefined parameters in the model.

6.1.3 MODEL FORCE COMPONENTS

The contact areas were not measured in the previous cutting experiments and made it hard to compare individual cutting experiments. The Arcona model was used to compare experimental forces with the modeled forces according to the measured experimental flank and chip contact areas. It was also used to develop methods to measure grit contact and cutting areas and explain the seemingly variable forces discussed in Section 5. The measurement techniques in Sections 6.2, 6.3 and 7.5 were used to measure the face area of the chip, flank area of the tool, and shear angle for use in the Arcona model.

6.2 MEASURING REMOVED WORKPIECE MATERIAL

6.2.1 INCREASING DEPTH SPIRAL

Since individual grits have dissimilar geometry, a method was developed to determine the geometry of the grit based on the groove left in a workpiece after cutting. A non-overlapping traverse tool path was used to distinguish the grit groove. The idea is like looking at a negative image of the grit to determine the actual depth of cut and removed chip area from the workpiece. The removed chip area, or cutting area, is synonymous to the uncut chip area for well-defined tools. The removed cutting area provides an independent measurement parameter to compare measured forces. Since each cut area can be directly correlated to that individual experiment, cutting and thrust forces for grits with different localized geometries could be directly compared.

The spiral cut started off as a non-overlapping version of the traverse cut but was then combined with the plunge cut to test grits more efficiently. The spiral cut had both a plunge feed and traverse feed as shown in Figure 6-2. The translation or traverse feed was large enough ($>300 \mu\text{m}/\text{rev}$) to produce non-overlapping cutting grooves. The experiment was set up to increase the depth of cut continually to produce a range of cut chip areas; thus the

experiment was named an increasing depth spiral. This testing method supported measuring removed chip area trends that were then compared with forces for various grits, regardless of localized geometry.

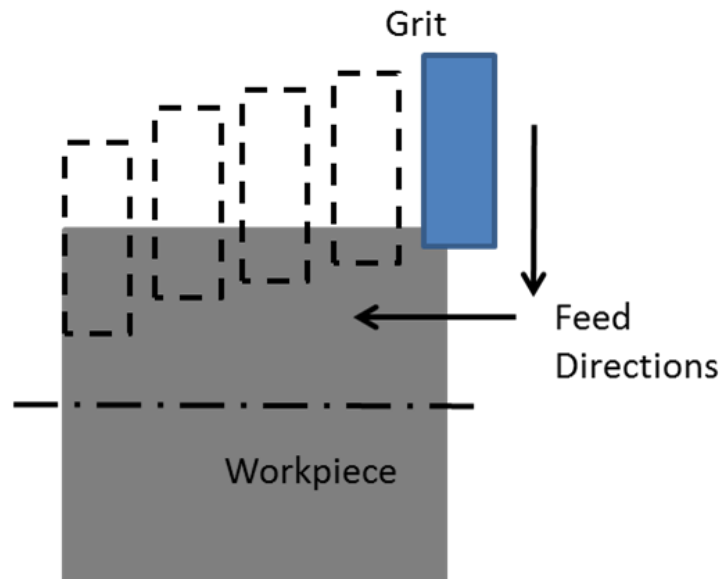


Figure 6-2. Increasing Depth Spiral Experiment with grit profiles every revolution

6.2.2 POLARIS PROFILE MEASUREMENTS

The Polaris machine was a spherical CMM (coordinate measuring machine) that used a white light probe to measure surface features. The Polaris was built to measure surfaces of cylindrical and spherical like objects that may have complex curvature. However the diameters of most objects that have been measured to date are significantly smaller than the workpiece diameters. The optical measurement and light probe used for measurements was a Precitec Optronik, CHRcodile S with a spot size of 5-6 μm^2 . The system is a white light chromatic aberration probe with a $\pm 30^\circ$ angular range and 300 μm linear range from a surface perpendicular to the probe. However, due to material finish or roughness, the probe range could diminish.

A brass workpiece mounted on the Polaris spindle is shown in Figure 6-3 with the light probe in range for measurement. The Polaris can measure three dimensional profiles of the workpiece and tool grooves over many revolutions. To demonstrate this capability a workpiece was measured on the Polaris machine and the machine axes were moved to record the shape of the cylindrical surface of the workpiece. A profile could be recreated using the measured points and interpolated to create a complete surface. A measured cylinder example in Figure 6-4a could then be unwrapped into a planar surface in Figure 6-4b and further examined to measure distinct groove geometries.

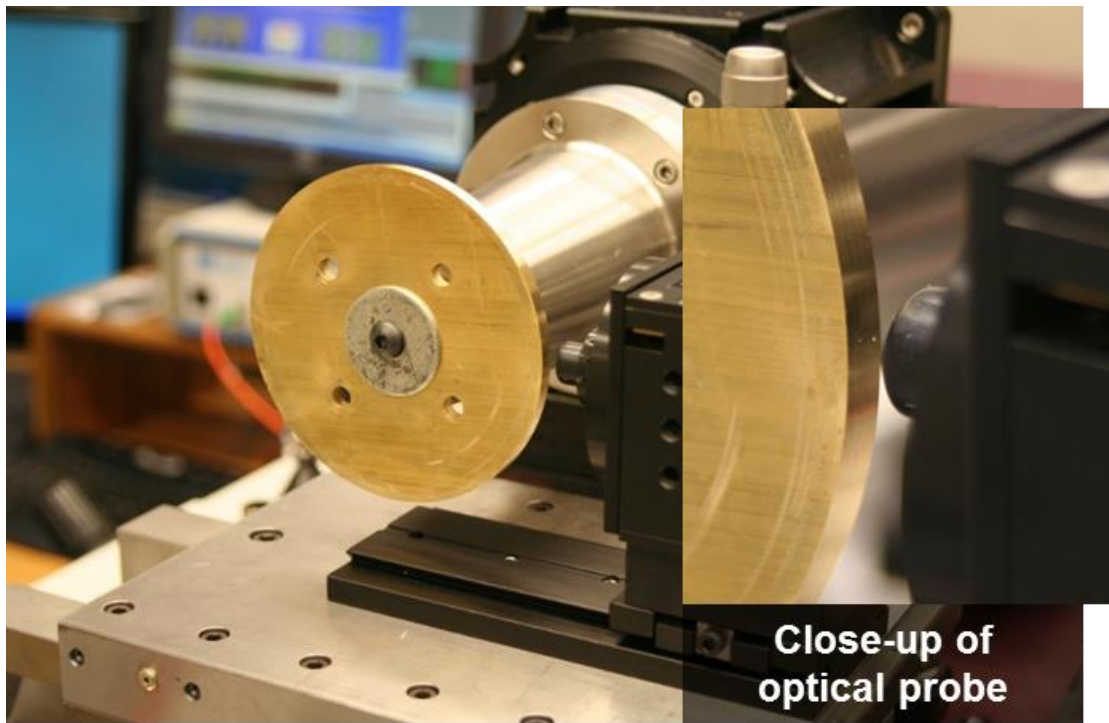


Figure 6-3. Polaris CMM and Optical Probe

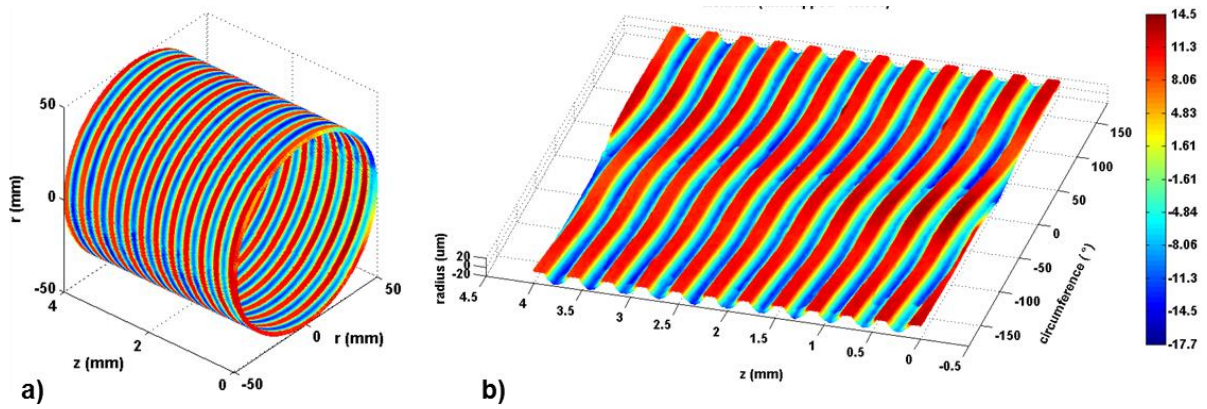


Figure 6-4. a) Polaris Cylinder Measurement and b) Unwrapped Polaris Surface

The groove geometries created by the grit could then be correlated with respect to measured experimental forces. A section of an unwrapped workpiece is shown in Figure 6-5, where the right edge is the front of the workpiece and the top and bottom edges could be reconnected to form a cylinder again. The left side of Figure 6-5 is cut off to show the detail of a few grooves. Some burring exists at the front of the workpiece, shown by higher regions of the profile. Unfortunately the surface had higher slopes (especially for the zero rake angle tool) that were beyond the angular range of the probe.

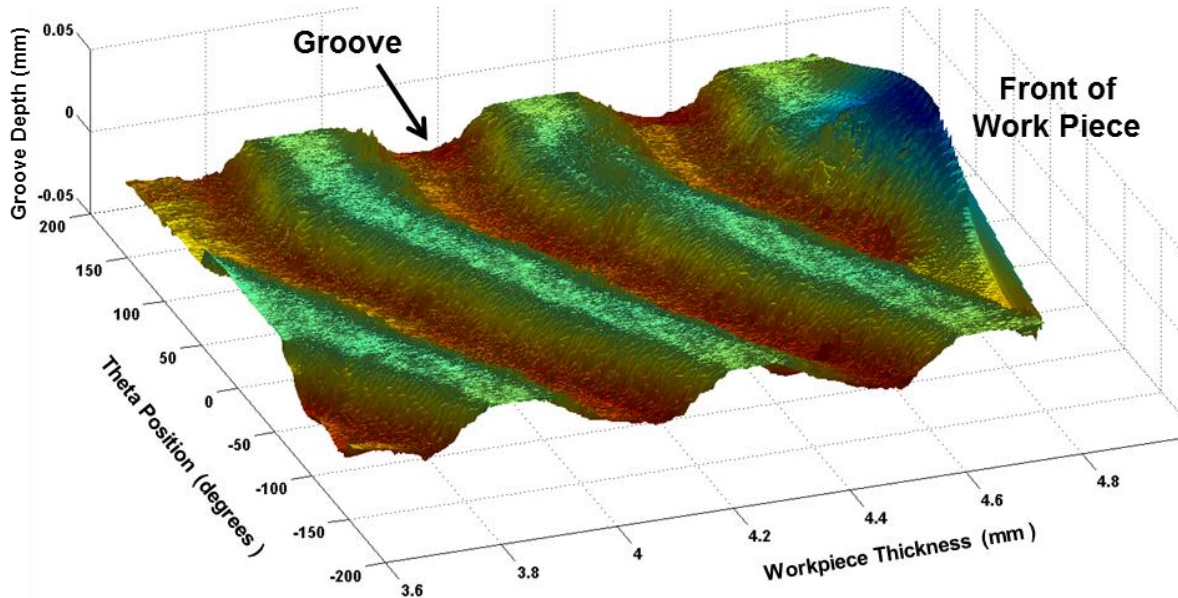


Figure 6-5. Close up Unwrapped Polaris Measurement for Workpiece Grooves

With regards to interpolation, data was taken at a rate of 752 Hz from the light pen while the z-axis, axial direction on workpiece, was moved at 6 $\mu\text{m}/\text{revolution}$. At a spindle speed of 60 RPM for a 100 mm diameter disk the data density would be 399 points/ mm^2 . However the data would be 6 μm apart along the axial direction and about 418 μm in the circumferential direction. In order to create a smaller data density the data would either take much longer to collect or a large interpolation would misrepresent the profile of the grooves as shown in Figure 6-6. Better data densities took an upwards of 30 minutes to an hour but were still affected by data dropout at steep grooves that were larger than the probes nominal $\pm 30^\circ$ range. Some dropouts also occurred at roughly cut edges where burrs and very thin features created drop outs in the data. The ten equally spaced grooves in Figure 6-6 follow up a single revolution of a workpiece groove and the profile measurements were 36° apart from each other.

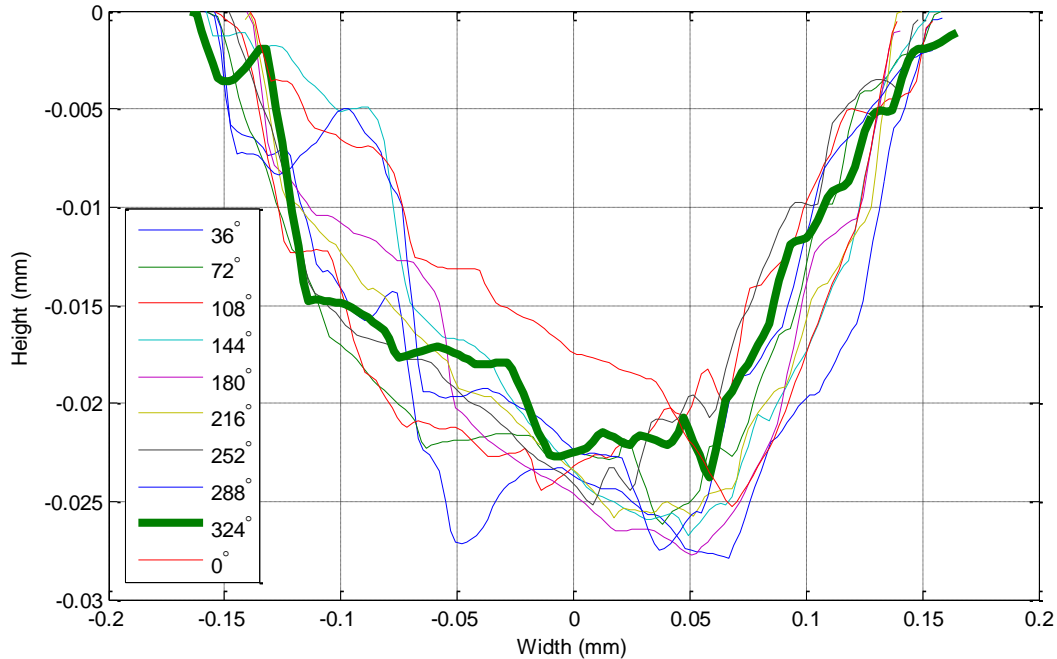


Figure 6-6. Polaris Groove Profiles that were Distorted by Interpolation of Poor Data Density and Probe Drop Out

The combination of data dropout at steep grooves and data density issues resulted in replacing the Polaris with a contact probe for groove measurements. However, a more versatile light pen could potentially improve the quality of the Polaris measurements for the complex geometry of the workpiece grooves. The contact probing technique that replaced the Polaris measurements could record 2D profiles of the groove geometries.

6.2.3 TALYSURF GROOVE MEASUREMENT

A Taylor-Hobson Talysurf Series 2 contact probe was used to measure the workpiece grooves. This provided the cutting profile, or removed chip area, of the grit. The profiles were taken along the axial direction of the workpiece, so each groove corresponded to a consecutive revolution of the workpiece; as long as a non-overlapping axial feed was used. An example of an axial profile with the Talysurf is given in Figure 6-7. Multiple axial measurements can be taken at various theta orientations around the workpiece if the profile groove changed drastically within a few revolutions. This allows a glimpse of cutting while

the grit wears, or if it wears at all. Various changes in the forces could also be compared with the change in the groove profile.

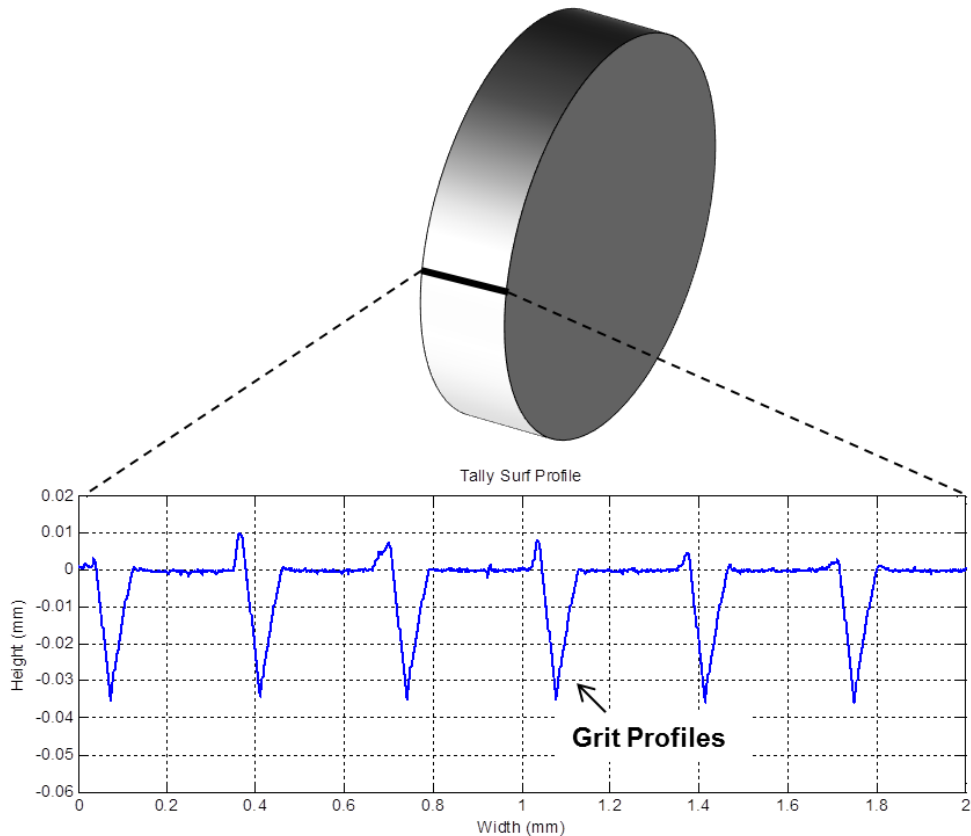


Figure 6-7. Axial Grit Profile with the Talysurf

The Talysurf contact probe has a diamond with a $2\ \mu\text{m}$ tip radius and 60° inclined angle from the tip of the diamond. Features below $2\ \mu\text{m}$ radius could not be measured due to the limitations of the contact probe tip radius. Since both the diamond probe tip and groove angles were nominally 60° at the zero rake orientation, small features could be distorted. The resolution of the stylus arm, measuring vertical displacement, can be as low as $16\ \text{nm}$.

The 0° spindle position was marked on the workpiece before the workpiece was removed from the spindle for measurement to relate the forces to spindle position. A rotary index on

the Talysurf was then used to align the workpiece 0° mark with the contact probe within a few degrees. The workpiece was then rotated with the rotary index for subsequent measurements at specific spindle positions. Profile measurements were taken at the 0° and 180° spindle theta position for the zero rake experiments while the negative and halfway rake experimental measurements were taken in increments of 60° around the workpiece. The zero rake experiments had little change between revolutions and only two measurements per revolution were necessary, while the negative rake experiments changed more frequently and required a larger number of profile measurements for good force correlation. The rotary index measurements were related within 1-2 ° of the spindle position. A picture of the Talysurf and rotary index is given in Figure 6-8.

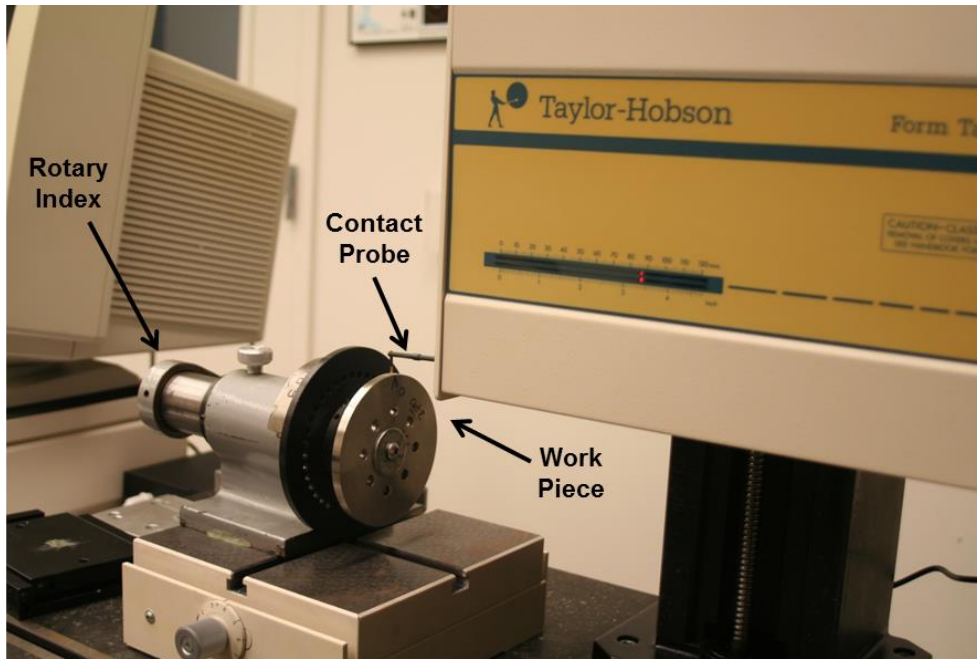


Figure 6-8. Talysurf and Rotary Index Setup for Axial Profile Measurements

6.2.4 RELATING GROOVES TO FORCES

The workpiece groove measurements were correlated with a force at a specific point in time. Also the tool path needed a distinct non-overlapping path to distinguish the removed

workpiece material for each workpiece revolution. Since the DTM spindle theta position was recorded simultaneously as the cutting forces, the first groove on a Talysurf profile corresponded to the forces for the same spindle theta position. This applied to the subsequent grooves and corresponded to the force at the same theta position but one workpiece revolution later. The reference mark has some inherent error within a few degrees because it was marked by hand and was then lined up again on the Talysurf for measurements. To prevent the inherent error from distorting data the force data was averaged with 19 adjacent data points. At a 1 m/s surface speed this corresponded to an average force over a 4° theta range. This same technique was used for higher speeds, but corresponded to a larger theta range. Figure 6-9 gives a graphical representation of how the forces were correlated to the measured workpiece theta position. The spindle theta position, cutting force, and thrust force were triggered simultaneously so the data was related by the time the data was recorded. Figure 6-9 shows the correlated cutting and thrust forces for the first measured workpiece groove at 0° and for the subsequent revolutions.

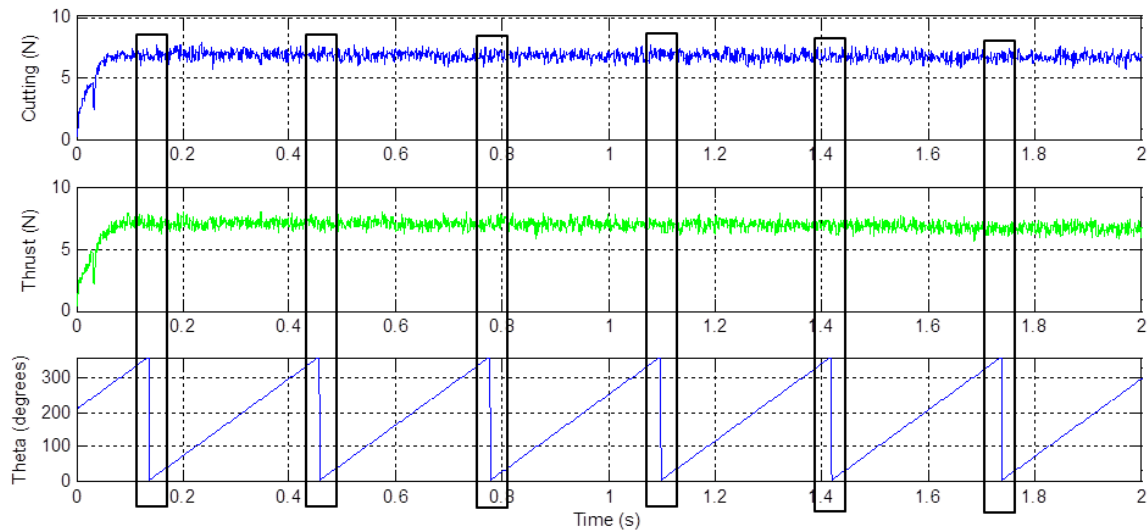


Figure 6-9. Relating forces to workpiece grooves at 0° spindle position (theta)

6.3 MEASURING FLANK CONTACT AREA

6.3.1 FLANK CONTACT INTRO

The flank contact area contributes to cutting and thrust forces according to the Arcona model in Equations (6-2) and (6-3) in Section 6.1.2. The flank contact area gives further incite to the origin of experimental forces. The flank area was measured from a picture of the grit and not from the workpiece like the chip area. Measurements were used in force calculations for the Arcona model forces to compare with experimental forces. Both flank and chip contact areas were needed to fully define forces from the Arcona model.

6.3.2 OPTICAL MICROSCOPE MEASUREMENTS

An optical microscope was used to measure grit flank areas by taking pictures of the grit before each experiment was conducted. The flank area measurement was determined through post image processing. A 100x and 200x objective were used to view the grit. Pictures of two orthogonal views were taken before and after a cutting experiment. Figure 6-10 shows the top and side view of a mounted grit. A high contrast background was used to ensure the profile was defined. In each picture only about 600 μm of the grit is shown ($\sim 300 \mu\text{m}$ of overhang), the grit mount covers the unseen portion.

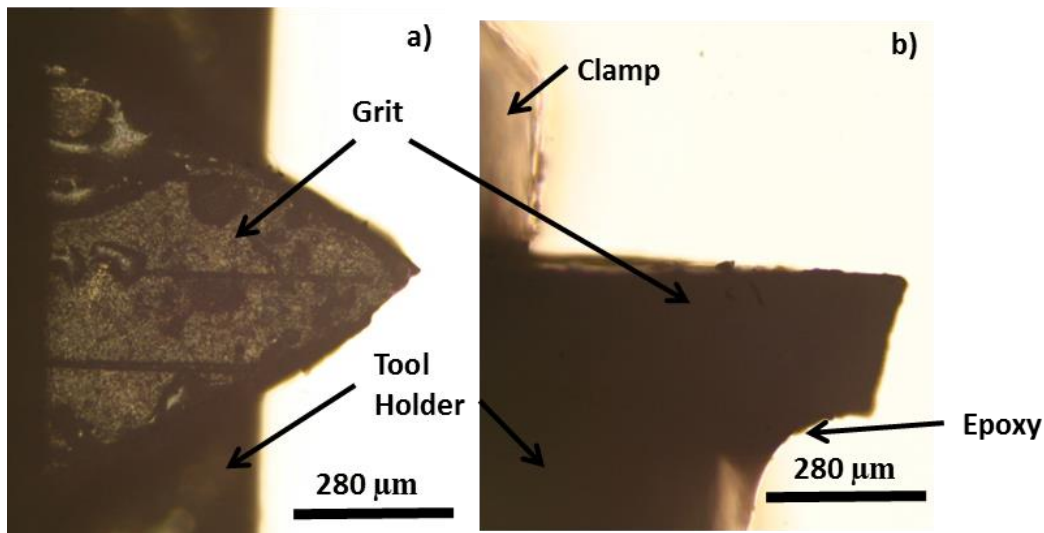


Figure 6-10. Grit Profile: a) Top View, b) Side View

A modified MATLAB program, Digitize13¹, was used on the optical microscope images to relate the pixel distance to physical size through use of a calibration factor. The calibration factor for a 100x image was 0.00066034 mm/pixel and 0.00033328 mm/pixel for a 200x image. A user selected the measurement area by placing markers on the profile of the object. Once the user had defined the region with markers, the area enclosed within the markers was determined using MATLAB's *polyarea* tool. The optical microscope could also be used to measure overall grit size changes. Wear could be measured by comparing the profile change of a grit before and after fracture occurred.

6.3.3 GRIT FLANK CONTACT AREA MEASUREMENTS: ZERO RAKE ORIENTATION

The optical microscope was used to determine the flank area and geometry of a grit in contact with the workpiece to be used with the Arcona force model in Equation (6-2) and (6-3) in Section 6.1.2. The grit flank area is shown in Figure 6-11 for the zero rake orientation and the side view of the grit, Figure 6-11b, is used to measure the flank area. However, there were two faces of the grit that contain the flank area and are shown as the edges forming a horizontal "V" on the grit in Figure 6-11a. The grit was assumed symmetric and the measured flank area was multiplied by two. The flank face was assumed to be planar so the entire flank face would be in contact with the workpiece. Depending on specific grit geometries, areas of the flank face could potentially be in contact with the workpiece while areas next to a high spot may not be in contact.

¹ Digitize13 was a program created by Ken Garrard of the Precision Engineering Center for image measurement. The program used a freeware MATLAB code that imports pixel values into matrices.

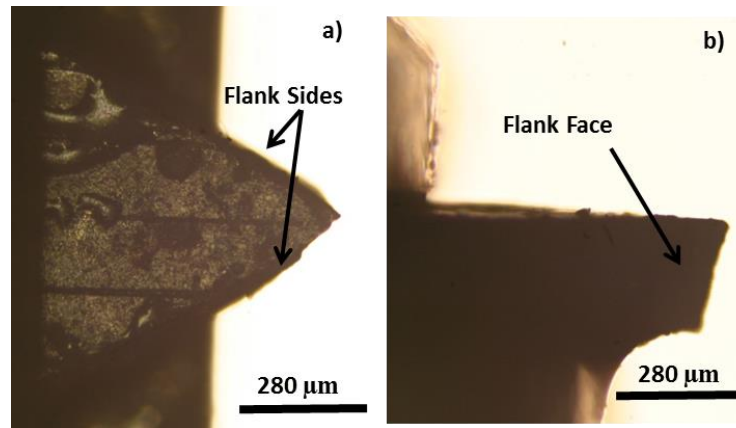


Figure 6-11. Zero Rake Flank Faces a) Top view and the two flank face edges, b) Side view and the flank face

Since the flank edges were oblique to the viewing plane of the microscope in Figure 6-11b, the image was corrected in a similar method to Lane [23] and Shi [25] which was used in diamond tool wear images. Using the geometrical relationship between a foreshortened, or tilted, length to an actual length, the true size of the grit length was determined. If an image has a known length of L and is then foreshortened by an angle, the relationship between the two lengths is $L = \frac{L'}{\cos(\theta)}$, shown in Figure 6-12.

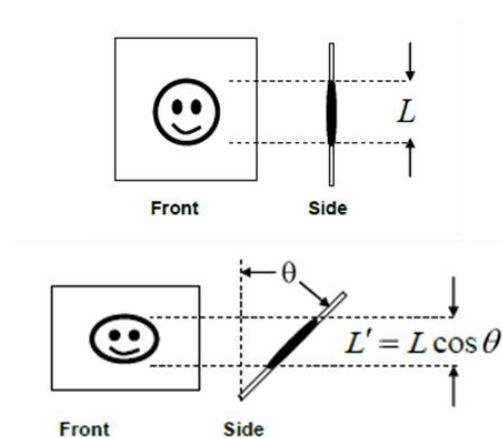


Figure 6-12. True height measurement for a foreshortened surface [23]

The oblique flank face of the grit was tilted at a 30° angle with respect to the microscope image, assuming the each grit was an equilateral triangular prism. The image was stretched by a factor of 1.155 or $1/\cos(30^\circ)$ in the horizontal direction, demonstrated in Figure 6-13.



Figure 6-13. Original and Stretched Flank Face Images

The depth of cut influences the width of the grit in contact with the workpiece and is necessary to determine the flank contact area. The depth of cut was determined by the Talysurf surface profile measurements described in Section 6.2. The flank area was measured at a specific depth of cut with Digitize13 by selecting the profile of the grit and eliminating x axis points greater than the depth of cut. A traced flank area measurement is shown in Figure 6-14. The flank face area was measured at several depths of cut to produce a trend line between contact area and the depth of cut. From the best fit trend line the flank area could be related for all of the depths of cut measured from the workpiece profile measurements. Either a linear, exponential, or power fit line was used, depending on the

localized flank area and which fit with a lowest residual. Because there was a flank area on each side of the grit, the grit was assumed symmetric and the measured flank area was multiplied by two. This overall flank area was then used in the Arcona force model, as described in Equations (6-2) and (6-3) in Section 6.1.2.

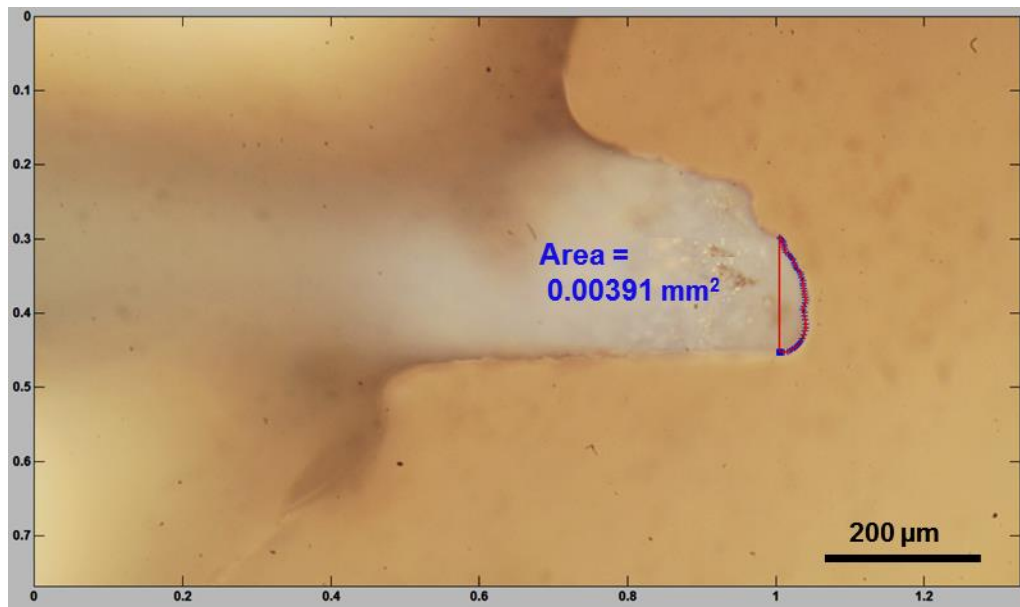


Figure 6-14. Flank Area Measurement

6.3.4 GRIT FLANK CONTACT AREA MEASUREMENTS: NEGATIVE RAKE ORIENTATION

The flank area measurement for the negative rake orientation was very similar to the zero rake orientation but the image was transformed differently. Because the grit does not come to an infinitely small tip but has some edge radius, the flank contact area includes the portion of the grit radius that contacts the workpiece as well as part of the rake face. The flank contact area is projected from the rake face contact shown in Figure 6-15c. The rake face is projected normal to the surface of the workpiece from the point on the rake face that is at the depth of cut to the grit radius. The flank contact due to the grit radius is projected normal to the workpiece. The rake face can also be projected tangent to the work piece to make up the

rake face contact area, shown in Figure 6-15a. The front view of the cutting process is depicted in Figure 6-15b.

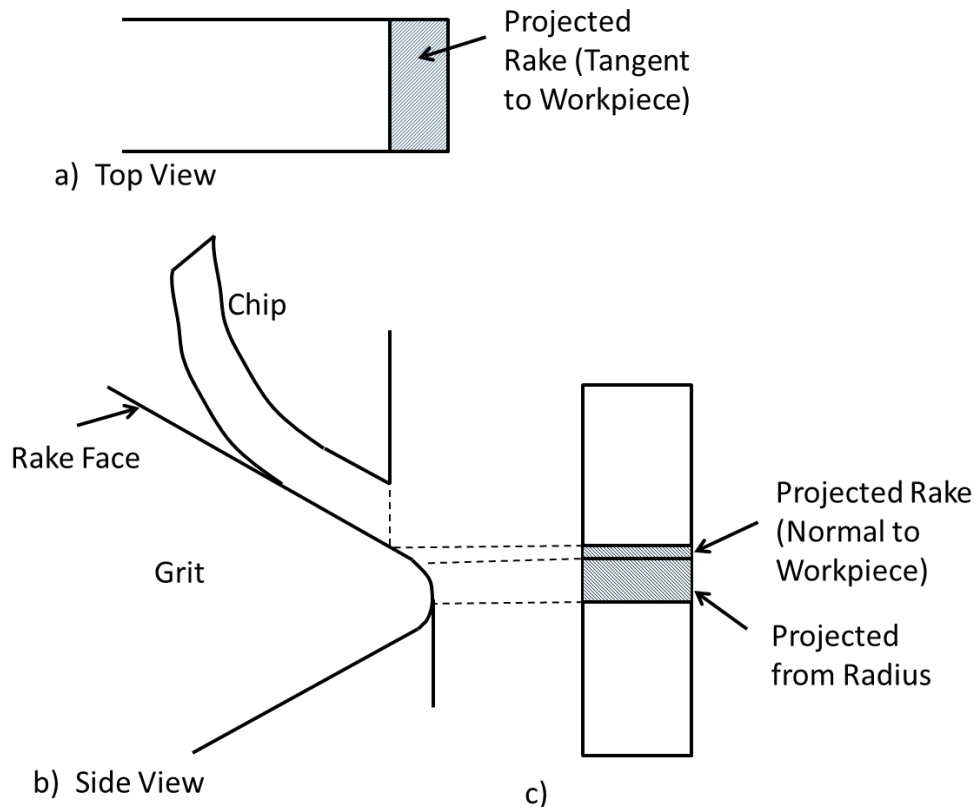


Figure 6-15. Negative Rake Flank Area a) Top View and projection of rake area, b) Front view, c) right side view and projection of flank area

The area along the rake face can be measured in the same method used to stretch the image for calculating the zero rake flank area. However, the measured area from the stretched image (shown in Figure 6-14) must be projected to represent only the flank contact area by multiplying the image area by $\sin(30)$. An alternative method can be accomplished without stretching the image by measuring the original projected rake area from Figure 6-13, and then multiplying it by $\tan(30)$ to make it the projected flank area. This effectively projects

the measured area normal to the workpiece, instead of tangent to the workpiece. Otherwise, the flank area was related to the depth of cut in the same manner as the zero rake orientation. The contact area was measured over several depths of cut and related to a best fit model so the flank area could be determined for each experimental groove profile.

7 GRIT CUTTING RESULTS

7.1 CUTTING SPEED COMPARISON: 304 SS

The effect of cutting speed was explored for the 304 stainless steel material. Several grits were investigated at 1 m/s, 4 m/s, and 8 m/s cutting speeds with the increasing depth of cut spiral experiment. The grits were positioned in the zero rake tool orientation, described in Section 4.4. The groove geometry was measured with the Talysurf to determine both the area of removed material and the depth of cut described in Section 6.2. The chip area was measured twice per revolution and the force data was correlated to the grooves at those two locations. The forces for each speed are plotted in Figure 7-1 as a function of measured cut chip area. The number of data points collected varied based on the length of cut before the grit fractured. A new grit was used in each experiment and is represented by a separate symbol in Figure 7-1. Each speed is separated by color to recognize overall trends and each speed trend is outlined in Figure 7-2. Individual experiments are plotted in Figure 7-1 and demonstrate experimental variation at the same parameters. Two experiments were conducted at a single depth of cut, nominally set at 40 μm , and are labeled with two asterisks (**). The single depth experiments are located between 1200 to 1400 μm^2 cut chip area.

Figure 7-1 shows a small data spread in experiments that were conducted at the same cutting parameters and cutting speed. The data deviates from a single trend line most likely due to a variation or mismatch between the measured removed chip areas and forces. The experiments conducted at a single depth of cut also illustrate the variation of forces in the experiments. Even with a small variation, measuring the removed chip area provides a large improvement in describing cutting trends.

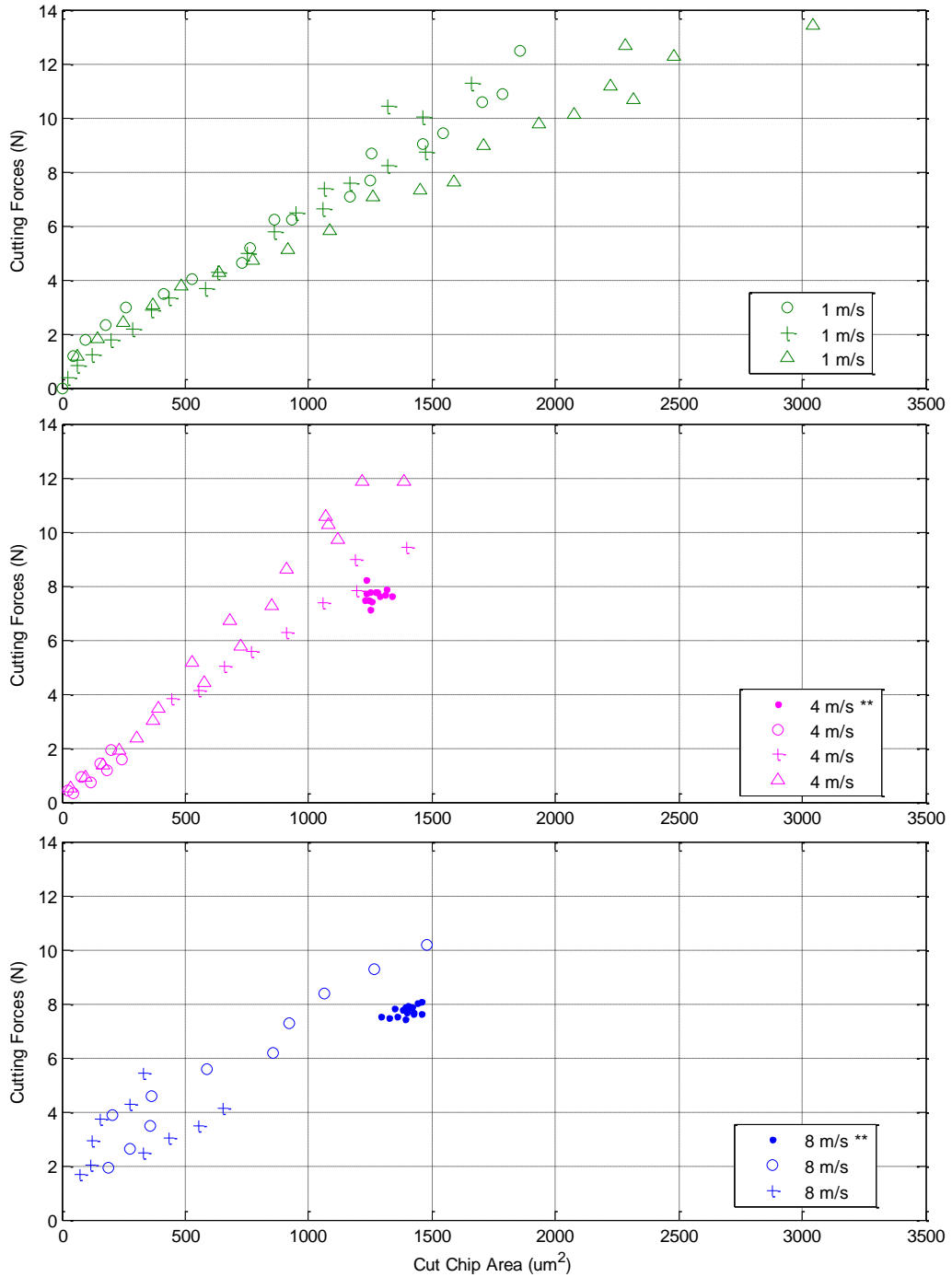


Figure 7-1. Ten Increasing Depth Cutting Experiments at Different Cutting Speeds with Zero Rake Tool on 304 SS (** Experiments were at a Single Depth of Cut)

Figure 7-2 and Figure 7-3 describe the overall trends between the three cutting speeds. The experiments plotted in Figure 7-1 are combined for each cutting speed and plotted in Figure 7-2 for cutting forces and Figure 7-3 for thrust forces. The overall trend for each speed is overlaid on the data to distinguish the parameters. The 4 m/s force trend has the highest forces followed by the 1 m/s forces. The 8 m/s force trend is different than the two lower speeds. It starts off at a higher force at lower removed material areas and drops below the 1 m/s and 4 m/s trends at higher removed chip areas.

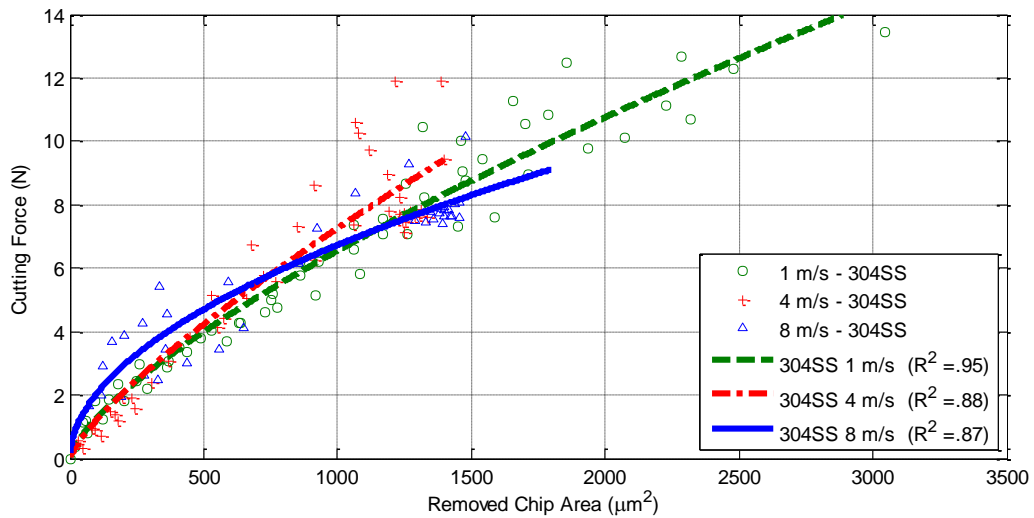


Figure 7-2. Zero Rake Speed Comparison for Cutting Forces on 304 SS

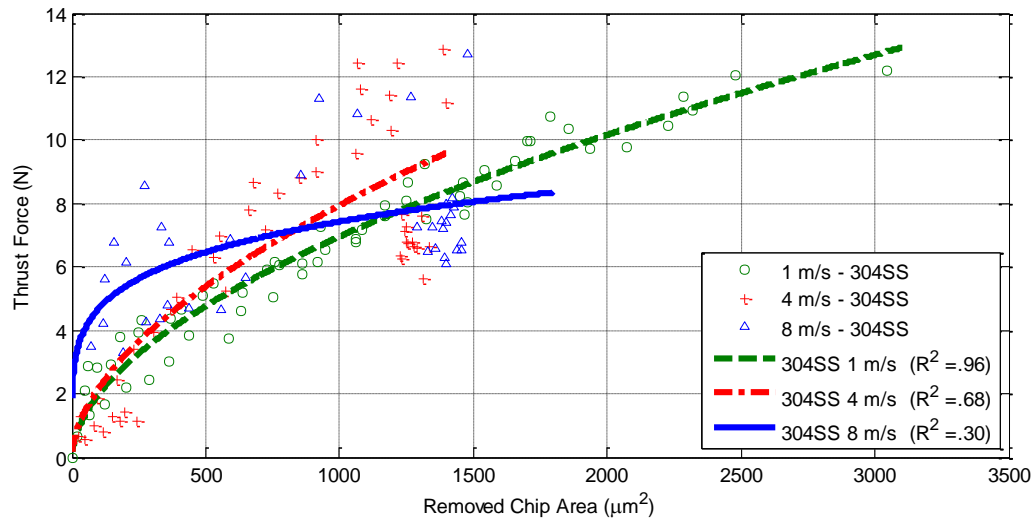


Figure 7-3. Zero Rake Speed Comparison for Thrust Forces on 304 SS

Comparing Figure 7-2 and Figure 7-3 shows the cutting forces were correlated to the removed chip area more than the thrust forces. This suggests that some of the variation in the forces between experiments may be due to an effect of the flank contact area of the grit. The experiments were compared by only using chip area but the flank contact and friction on the flank face are important (the flank and chip contact area impact forces in the Arcona model described in Section 6.1). The variation could also be due to differences in the grit geometry that diverges from a geometrically planar shape. The measurement techniques, such as removed chip area, assumed that each grit was planar and contacted the workpiece in the same way. These assumptions do not take into account the differences of the grit roughness or localized shape on the rake and flank faces. The data spread is shown by the data points that do not lie along the fitted trend line. The absolute cause of the data spread was not identified, but has been taken to be a characteristic of the experiments within the discussion of single grit testing.

7.2 WORKPIECE MATERIALS

7.2.1 BACKGROUND ON MATERIALS

Materials were used to study grit performance. A range of steel materials were used to compare the workpiece impact, including 304 SS, 4330V alloy steel, low carbon 1215 steel and 52100 bearing steel. The workpiece properties are given in Table 7-1. The Vickers hardness was directly measured from the workpieces and converted into the hardness, in GPa, that was used for the Arcona [5] model in Section 6.1.2. All other material properties are published values from MatWeb [30] given for reference.

Table 7-1. Workpiece Material Properties

Steel Type	Hardness (GPa)	Elasticity (GPa)	Thermal Cond. (W/m-K)
304 SS	2.202 (224Vhn)	193*	16.2 *
4330V	2.740 (279 Vhn)	200*	44.4 ⁺
1215	1.85 (189 Vhn)	200*	51.9*
52100	8.224 (838 Vhn)	210*	46.6*

* properties from MatWeb [30]

⁺ properties for 4340V

The steels had a variety of hardness values which, according to the Arcona [5] model, should affect the overall magnitude of forces for each material. The experiments were performed to determine the impact of the workpiece hardness and determine if there were other distinguishable grit cutting characteristics.

7.2.2 EXPERIMENTAL COMPARISON OF STEELS

Several experiments were conducted on a variety of steel workpieces at 1 m/s surface speed with the increasing depth of cut spiral discussed in Section 7. Experiments were conducted in the zero rake orientation, Section 4.4, and the removed chip area was measured per Section 6.2. Figure 7-4 to Figure 7-6 shows 4330V, 1215, and 52100 steel experiments. The figures

show the difference between individual cutting experiments at similar experimental conditions. The exception is the experiment labeled with two asterisks (**) was conducted at a uniform depth of cut. The variation with both the measured forces and contact areas between individual experiments can be noted within these experiments. A separate grit was used in individual experiments and is plotted with different symbols in Figure 7-4. The difference between experiments shows the effect of individual grits on forces. The last data point for each experiment in Figure 7-4 to Figure 7-6 is outlined with a square to represent the force before grit fracture. The typical fracture force occurred within about 2-3 N of the last, and usually highest, recorded force.

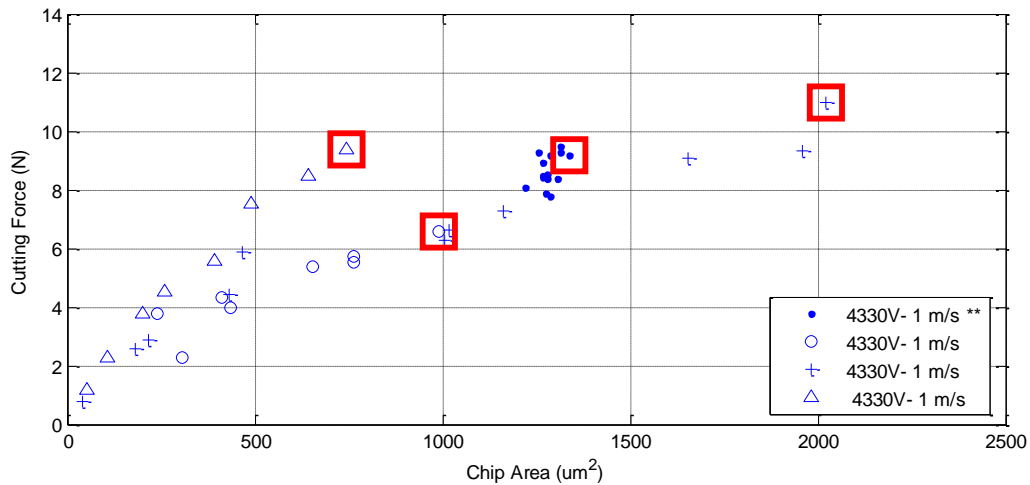


Figure 7-4. 4330 Steel Experimental Cutting Forces with Respect to Chip Area (** Experiment was at a Single Depth of Cut)

The 4330V steel had forces that were lower than expected based on the published hardness. This may have been due to inconsistent workpiece properties. The lot from which the 4330V workpiece samples were taken had a measured Vickers hardness of 412 Vhn (4.04 GPa) while a hardness test of the specific workpiece was only 279 Vhn (2.74 GPa). This disparity in hardness brings uncertainty in the analysis of the 4330V alloy steel. The experimental data forces were representative of the measured workpiece hardness of 279 Vhn.

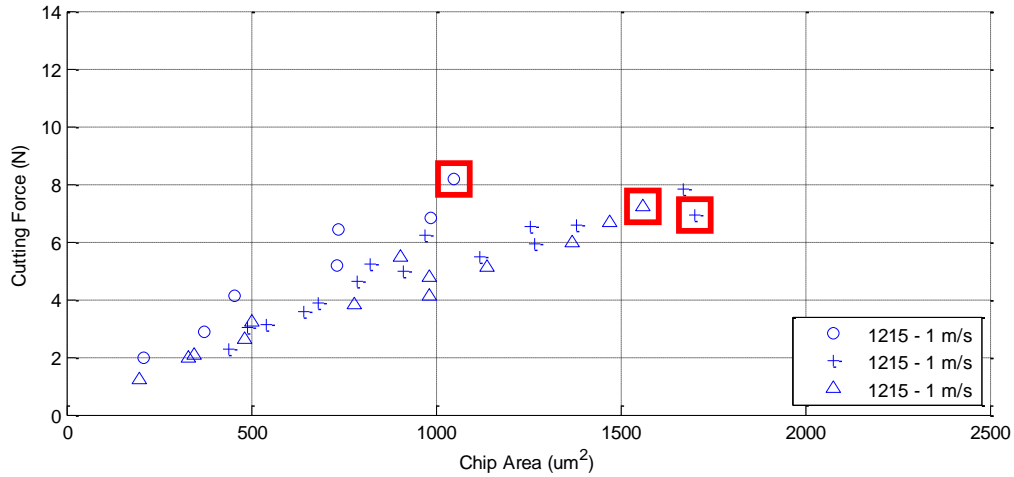


Figure 7-5. 1215 Steel Experimental Cutting Forces with Respect to Chip Area

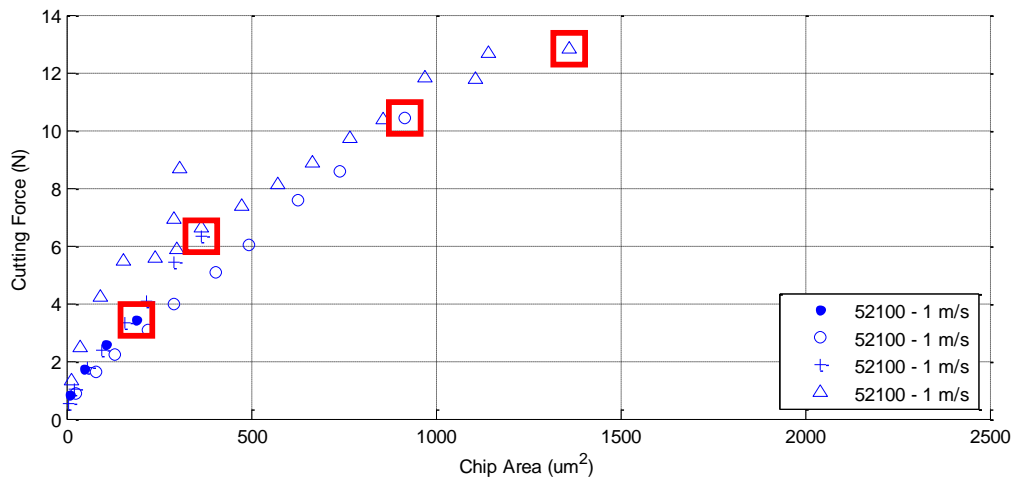


Figure 7-6. 52100 Steel Experimental Cutting Forces with Respect to Chip Area

The steel material experiments each followed distinguishable trends for separate grits and each material had a combined overall trend for the grits. Individual sets of experiments prove that relating forces to the removed chip area can be used as an analysis method to further define force characteristics. A comparison between all of the materials is given in Figure 7-7 and Figure 7-8. The forces for the 304 SS at 1 m/s surface speed were included in

the comparisons. Experimental data for the material comparison overlaps each other in the figures, so each material is plotted with a best fit line for clarity. The trend fits the overall data trend within the curve fit residuals noted in the legend.

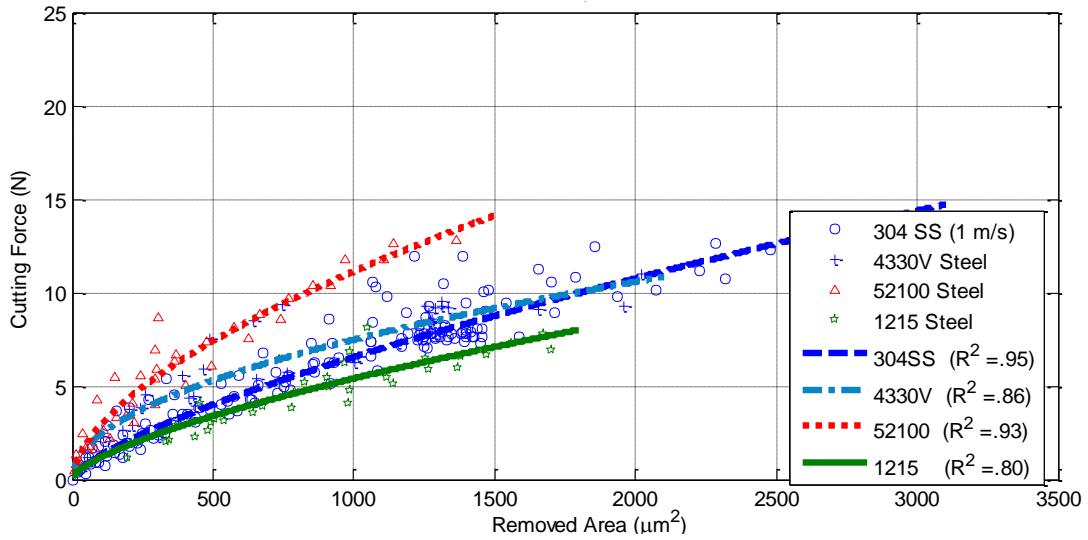


Figure 7-7. Cutting Force Comparison for Steel Materials at 1 m/s Surface Speed

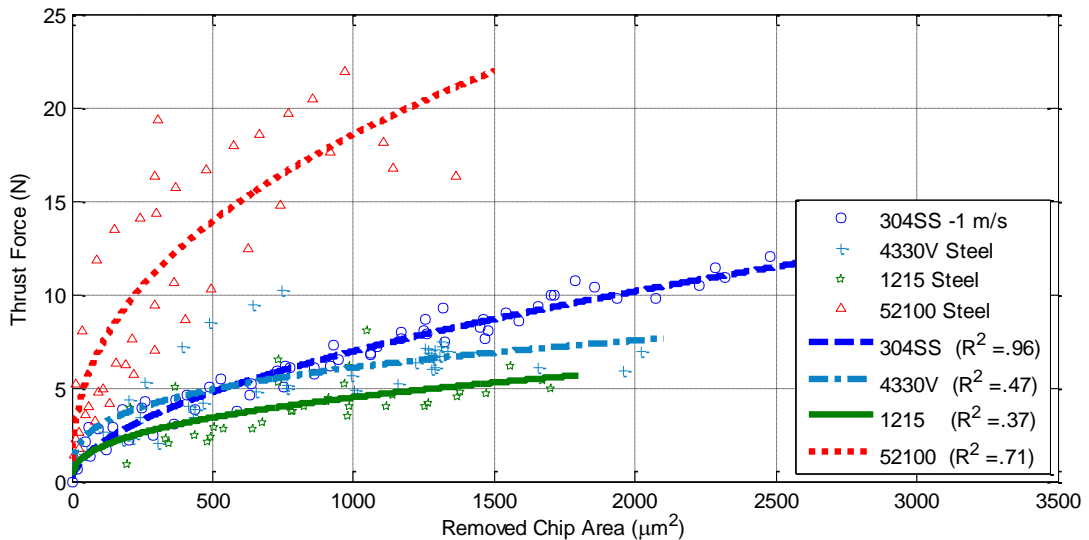


Figure 7-8. Thrust Force Comparison for Steel Materials at 1 m/s Surface Speed

Figure 7-1 through Figure 7-6 can be referenced to clarify individual material experimental data for the cutting force. Figure 7-7 and Figure 7-8 show the distinct difference in forces for the variety of steels over the range of removed chip areas. The 4330V forces were on average 18% larger than 304 SS cutting forces and 6% lower for thrust forces. The experimental data for 1215 steel was close to the 304 SS material trend. The 1215 steel forces were 8% and 14% lower than the 304SS cutting and thrust forces. The much harder 52100 steel had average forces that were 116% and 285% higher than the 304SS cutting and thrust forces.

In the material comparison, the thrust forces followed the same general material hardness trend as the cutting forces except the thrust forces had a larger variation from the average trend. The larger variation is most likely because the thrust forces are impacted more by the flank area, and the data was plotted according to the removed chip cutting area. Also for both the 1215 and 304SS materials, the cutting forces were larger than the thrust forces but the 52100 steel experiments resulted higher thrust forces than cutting. For the given grit geometry the thrust force was not higher than the cutting force until the hardest workpiece material was used.

Overall the material experiments followed a trend for material hardness. The increase in material hardness correlated to higher forces for the same chip area, as suggested by Arcona [5]. However it must be noted that correlation does not necessarily lead to causation.

7.2.3 EXPERIMENTAL VARIATION IN RELATED FORCES

Experiments for both the cutting speed and material type showed variation within individual experimental conditions. One thought on the variation of forces within experiments is that the flank area is relatively uncontrolled and is a factor in the force variation. Presumably a larger flank area would increase forces while a lower flank area would have smaller forces. The small variation in related forces could have masked the impact of speed in Section 7.1 while the material impact experiments provided more distinct trends.

Relating the forces to the grit geometry measurements of the removed chip area provided more consistent results than assuming similar grit geometry in Section 5. However it does not completely eliminate all geometry effects of grits. The experimental result from relating forces to a removed workpiece area demonstrates the value of defining the origin of forces. A further improvement of the techniques to measure and relate forces, or even new methods, could result in more accurate comparison of parameters during single grit testing.

7.3 GRIT ORIENTATION EFFECT

7.3.1 ORIENTATION IMPACT ON FORCES

The grits were tested in the zero, negative, and halfway rake orientations to determine the impact of randomly oriented grits on a coated abrasive product. The grits were oriented in the respective overall rake angle with the octagonal tool holder. Recall the halfway rake orientation was halfway between the zero and negative rake orientations. The grit orientations were described in Sections 4.3, 4.4, and 4.5. The removed chip area was measured per Section 6.2. The orientation experiments were conducted on a 304 SS workpiece at a 1 m/s surface cutting speed with an increasing depth spiral cut per Section 6.2.1. The impact of the grit orientation on the cutting and thrust forces with respect to the measured removed chip area is shown in Figure 7-9 and Figure 7-10.

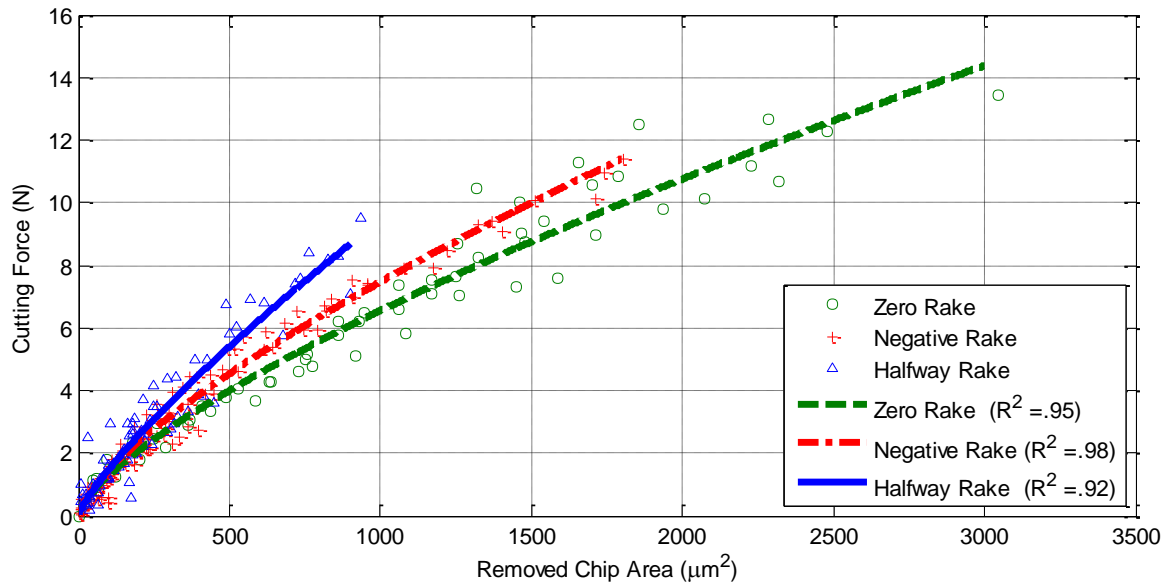


Figure 7-9. Grit Orientation Impact on Cutting Forces

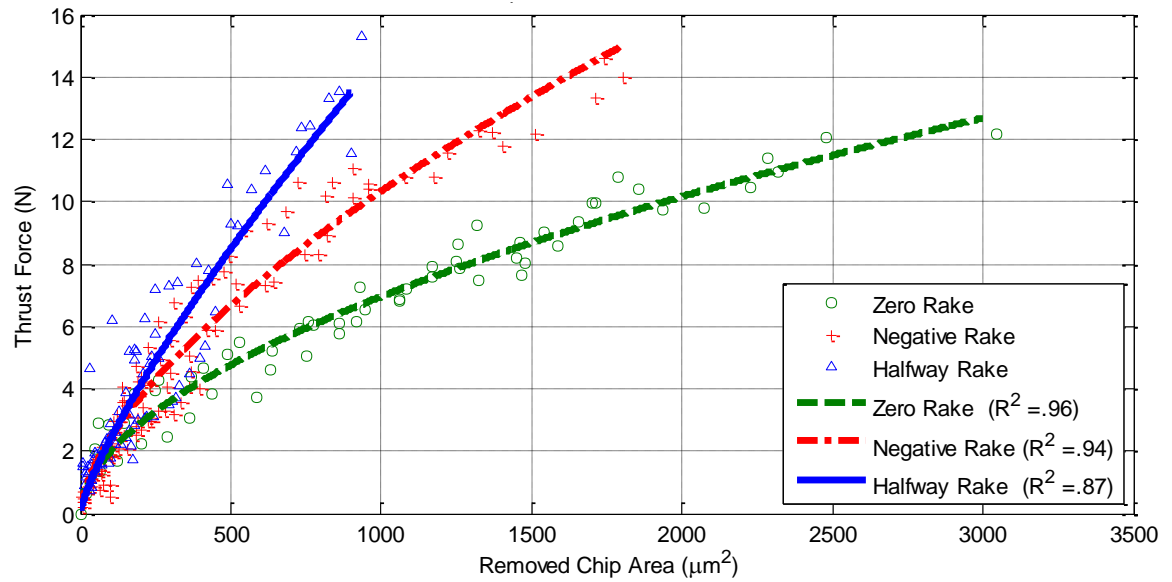


Figure 7-10. Grit Orientation Impact on Thrust Forces

The cutting and thrust forces showed similar trends with respect to the grit orientation. The zero rake orientation had the lowest average magnitude, followed by the negative and halfway rakes. Comparing the orientations with the zero rake as a baseline, the thrust forces increased over twice as much then the cutting forces. To compare the relation between the average cutting and thrust forces, the slope of a linear trend line was taken for the data. The average slope of the negative rake orientation cutting and thrust forces were 32% and 86% larger than the zero rake orientation. The average slope of the halfway rake forces were 87% and 199% greater than the negative rake orientation cutting and thrust forces.

The thrust force shows the distinctive relationship between a higher thrust for a negative rake angle tool while lower thrust for a zero rake angle tool. This is in general agreement to negative rake cutting tools [21]. The complex geometry and rake face associated with the halfway rake angle was hypothesized to produce an averaging effect from the two extreme orientations; however this was not the case. The experimental results for the halfway rake had the highest resulting forces for a given removed chip area. Recall the halfway rake angle had two oblique rake faces with respect to the cutting direction, one defined by the -30° rectangular rake face and the other by the 0° triangular rake face. Even with complex geometry such as the halfway rake orientation, comparing and quantifying various grit orientations and geometry was accomplished by measuring and relating removed chip areas to the forces.

7.3.2 ORIENTATION IMPACT ON GRIT FRACTURE AND MATERIAL REMOVAL

The grit orientation was found to have some impact on the magnitude of force for a given removed chip area, but the orientation also had a large impact on the dimensions of the removed chip area and types of wear. Both the workpiece grooves, and forces showed differences in the fracture rate of each orientation. A measured workpiece profile is given for each orientation in Figure 7-11 to Figure 7-13, where the original workpiece surface is at the 0 mm height. For each profile the y-axis is the groove height, or depth, into the workpiece and the x-axis is an arbitrary workpiece width position recorded on the Talysurf. The same scale is used in the three figures, and each groove is one revolution apart. The traverse feed

for the zero rake orientation was nominally 300 $\mu\text{m}/\text{rev}$ and 350 $\mu\text{m}/\text{rev}$ for the negative and halfway rake orientations. The grit path for each workpiece starts on the right of the figure and proceeds to the left as the axial and traverse feed both increase; the axial feed increases down and the traverse feed increases to the left.

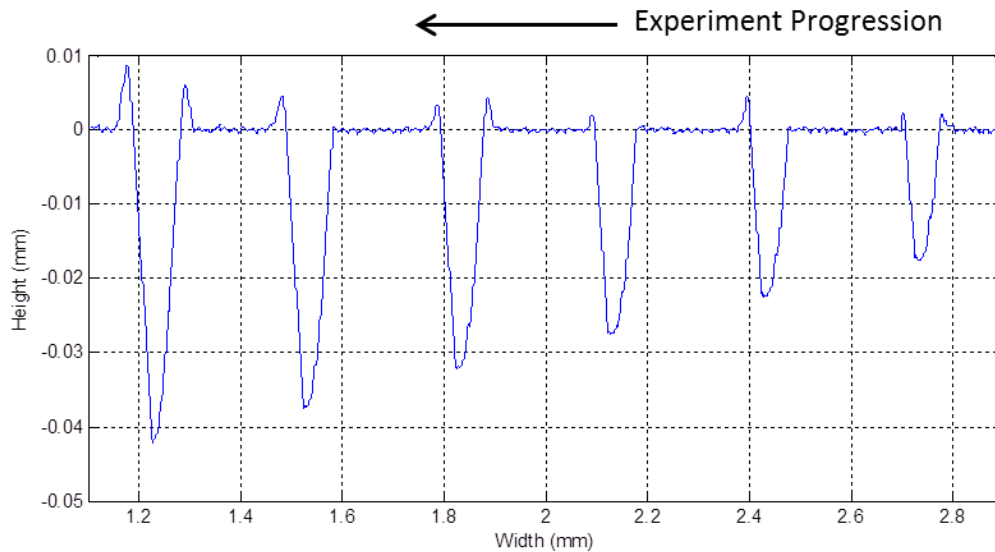


Figure 7-11. Zero Rake Orientation Workpiece Profile

The zero rake profile often reached large cutting depths and only sustained one or two fractures per experiment. The groove in Figure 7-11 sustained no fractures in the given window. The zero rake orientation was able to reach larger total material removed areas before fracture occurred. The overall removed material magnitudes can be inferred from Figure 7-9 and Figure 7-10 by noting the range of removed chip area magnitudes for each orientation.

Within the given workpiece profile range given in Figure 7-12, at least two known fractures occurred. Each fracture is marked with an arrow and can be located by noting the drastic profile change. Each profile revolution is marked within a bracket to improve clarity of how the grit contacted the workpiece and how the contact changed. The profile shows two

distinct high spots on the workpiece that change drastically in short cutting distances, compared to the zero rake orientation. The high spot on the right of the grit came into contact with the workpiece first and was followed by the left high spot. The progression of the grit profile demonstrates how rapidly a grit profile could change.

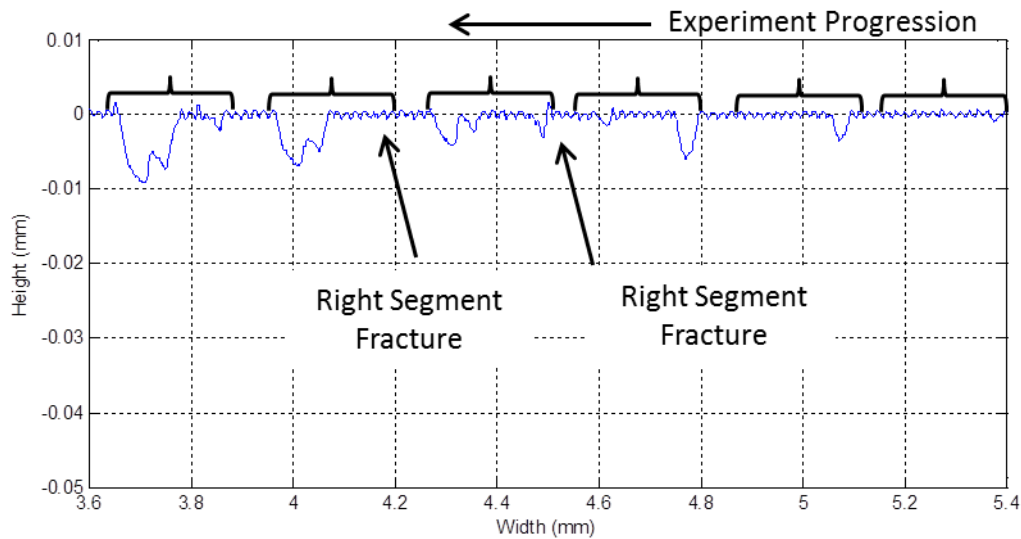


Figure 7-12. Negative Rake Orientation Workpiece Profile

The negative rake profiles showed that cutting occurred at depths of cut under $15\ \mu\text{m}$, which was considerably smaller than the zero rake orientation which reached $45\ \mu\text{m}$ depths. Even though the negative rake orientation cut at smaller depths of cut, the width of the grit in contact was larger than the zero rake orientation. The grit orientations showed the effect of having different rake face shapes and angles. The maximum removed chip area before a fracture occurred in the negative rake orientation was about half of the maximum area for the zero rake orientation.

The halfway rake orientation produced slightly larger cutting depths than the negative rake orientation but significantly lower depths than the zero rake orientation. The halfway rake orientation grooves were similar in shape to the zero rake orientation but had much lower

removed chip areas before fractures occurred. The halfway rake orientation grooves are described in Figure 7-13.

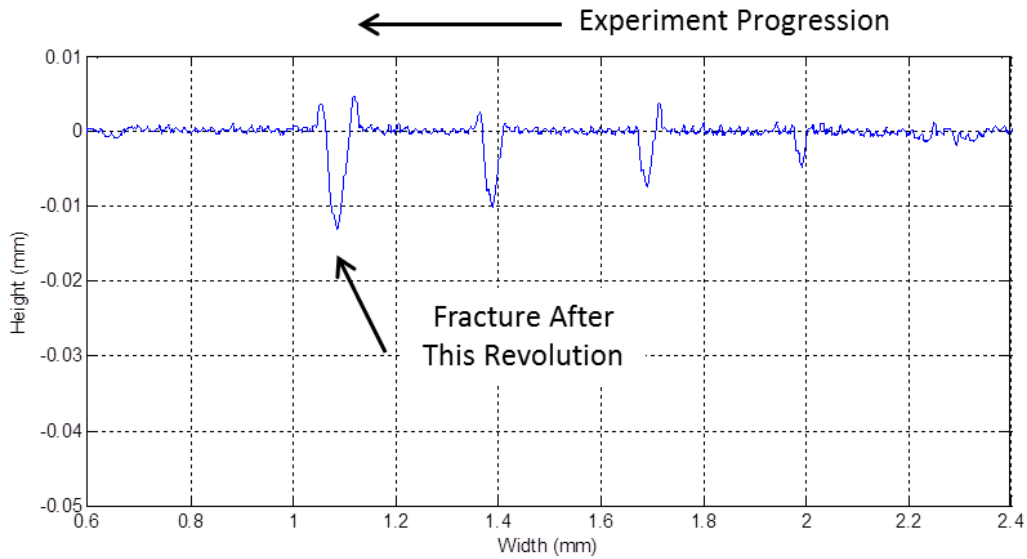


Figure 7-13. Halfway Rake Orientation Workpiece Profile

The three grit orientations each had slightly different characteristic cutting patterns. The maximum removed chip area before fracture relates to the largest x-axis experimental data point for each orientation which can be derived from Figure 7-9 and Figure 7-10. The fracture forces and respective removed chip areas are plotted in Figure 7-14. The largest removed area before the last grit fracture was the zero rake orientation, while the negative rake orientation was at about half of the removed area and the halfway rake orientation was about a third of the zero rake area.

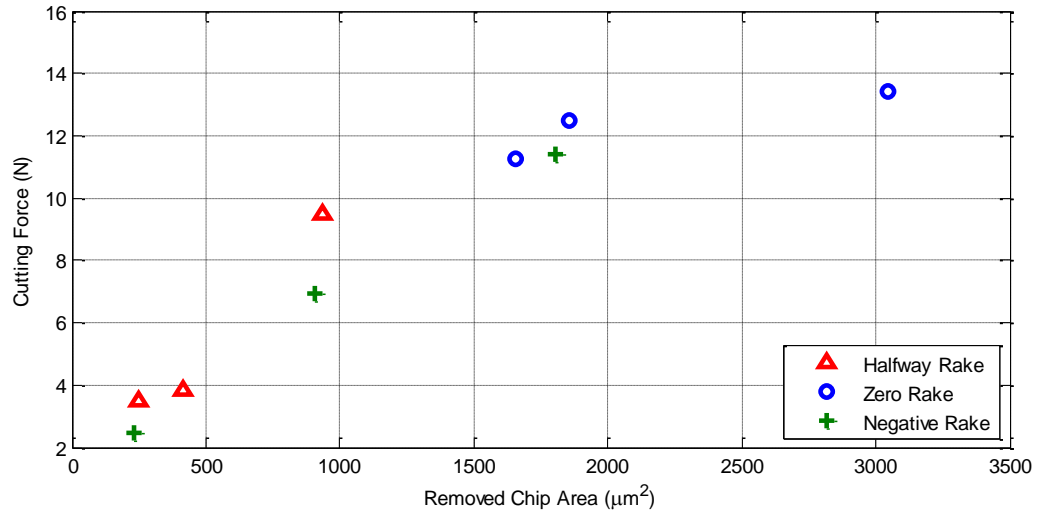


Figure 7-14. Orientation Fracture Forces and Removed Chip Area

A suggested area for further research is how the actual fracture event is affected by the grit orientation. Figure 7-15 shows a picture of the fracture point on the workpiece for each orientation in an increasing depth spiral experiment on 304 SS. Each point is accompanied by a location of stopped chip formation or possibly material accumulation. The zero rake orientation leaves a triangular imprint at fracture, corresponding to the geometry of the rake face, and the negative rake orientation looks like it leaves a similar imprint, but for the negative rake face shape. The strange fracture indentation occurs in the halfway rake orientation where the groove looked like a grit fracture started and the grit began to twist before the rest of the fracture occurred. This is inferred from the twist in the workpiece groove and the prolonged chip formation region at the fracture location. It seems that each of the orientations may incite fracture in different ways due to the various geometries and forces associated with each.

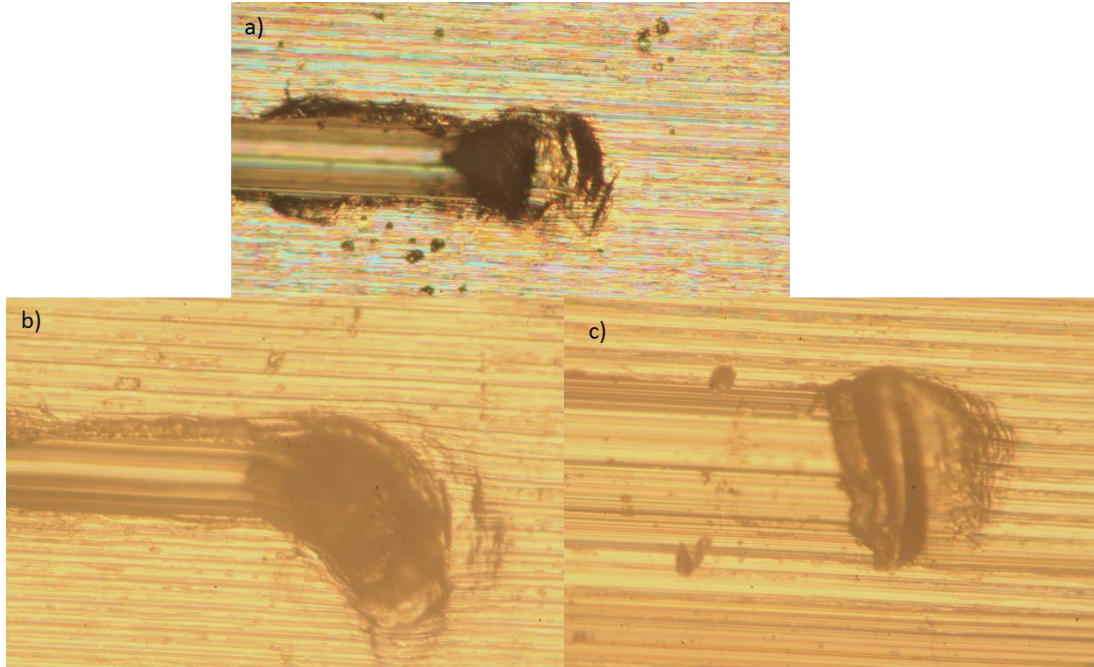


Figure 7-15. Fractures on a 304 SS at 1 m/s for an Increasing Depth Spiral: a) Zero Rake Orientation, b) Halfway Rake Orientation, c) Negative Rake Orientation

7.4 SPECIFIC CUTTING ENERGY COMPARISON

7.4.1 SPECIFIC CUTTING ENERGY BACKGROUND

A method of performance comparison is specific energy; used to measure both grinding and cutting tool performance. In grinding and cutting applications specific energy can be defined as the power required for grinding, P , divided by the volume material removal rate, Q . However, specific energy can also be defined as the cutting force (tangential force, F_c) divided by the cross-sectional area of the cut, $A_{profile}$. Shaw [2,6] used the latter method for calculating specific energy. The specific energy is given in Equation (7-1).

$$\mu_s = \frac{P}{Q} = \frac{F_c}{A_{profile}} \quad (7-1)$$

An important characteristic of specific energy is that at small depths of cut the specific energy of grinding abrasives increases due to the sizing effect, when the cutting edge radius

is on the same order of magnitude as the depth of cut [6,11,12,22]. Chip plowing accounts for the higher specific energy at lower material removal rates. As the material removal rate increases (increasing the depth of cut and removed chip area), the specific energy asymptotically approaches a steady state specific energy value [6,11,12].

Shaw [6] claims that specific energies are approximately the same for hard and soft steels. He explains this by noting that a possible cause is that soft steel has a lower strength but higher ductility while stronger steels often have lower ductility. This statement will be evaluated in the following section with an experimental comparison between steel workpieces.

Specific energy was also used to supplement experimental results previously discussed in Sections 7.1 to 7.3, to determine efficient cutting parameters from an energy perspective. Optimal parameters can be located via a minimum to the cutting energy for specific parameters. However it is important to consider that the specific energy comparison is from single grit testing conditions and will not directly compare to a grinding application with a plethora of randomly oriented grits. In a grinding application, the overall feed rate or depth of cut will be different over the range of active grits, on top of the variation between individual geometry. Nevertheless, in single grit testing for different abrasive products, the specific energy could be a useful comparison tool of the geometries. Specific cutting energy analysis will be used to compare the grit experiments side by side for different speeds, workpiece materials, and geometry orientations.

7.4.2 SPECIFIC CUTTING ENERGY RESULTS

The specific cutting energy of the experiments provided a different method to compare and analyze the already described data. Cutting parameters such as speed, material, or orientation were reanalyzed. The experiments for 304 SS 1215, 4330V, and 52100 steels at 1 m/s from Section 7.2 were compared in Figure 7-16 and Figure 7-17. Figure 7-16 shows the specific cutting energies plotted with respect to the removed chip area; the overall data trends are shown in Figure 7-17 for clarity.

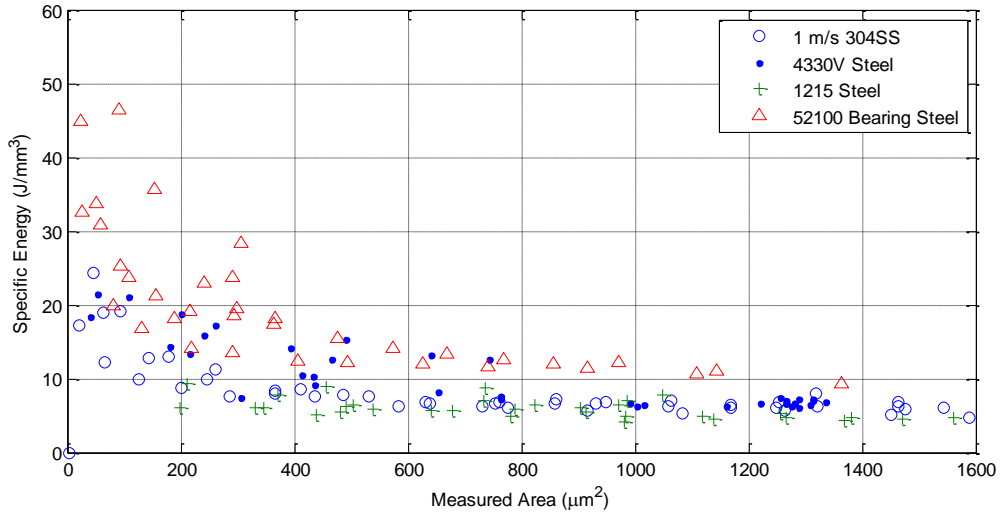


Figure 7-16. Specific Cutting Energy Comparison

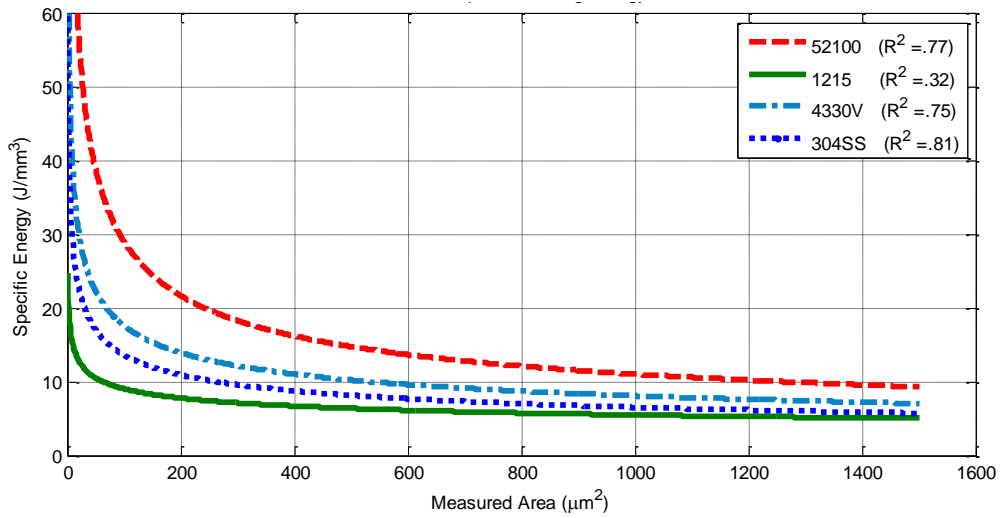


Figure 7-17. Specific Cutting Energy Data Fit for Clarity

Each trend appears to have a horizontal asymptote where the specific energy approaches a constant value. According to Rowe [12] this asymptote is the point at which the cutting regime takes full effect and there are minimal energy effects from plowing and rubbing.

Shaw's [6] conclusion with regards to the specific energy of steels being the same appears true once the cutting regime was fully established and approached the asymptote. All the steel materials seem to approach a similar specific cutting energy in the range of 5 J/mm³ to 9 J/mm³.

An optimal depth of cut can be determined by locating the removed chip area after the specific cutting energy is at a sufficiently low value and before fracture occurs for the specific workpiece material. However for the number of experiments conducted, an optimal range could not be determined. A statistically significant number of experiments would need to be conducted; especially at the upper range of the depth of cut where the fracture toughness of the grit will determine the maximum limit.

The specific cutting energy was calculated from the experiments discussed in Section 7.1 that were at 1, 4 and 8 m/s on the 304 SS workpiece. The same experimental data is plotted in Figure 7-18 but with respect to the specific energy. The 8 m/s force trend in Section 7.1 overlapped the 1 m/s and 4 m/s trends but the specific energy relation more clearly distinguishes between each speed at low removed chip areas. The specific energy of the three speeds shows that there may be a minimum specific energy between 1 m/s and 8 m/s.

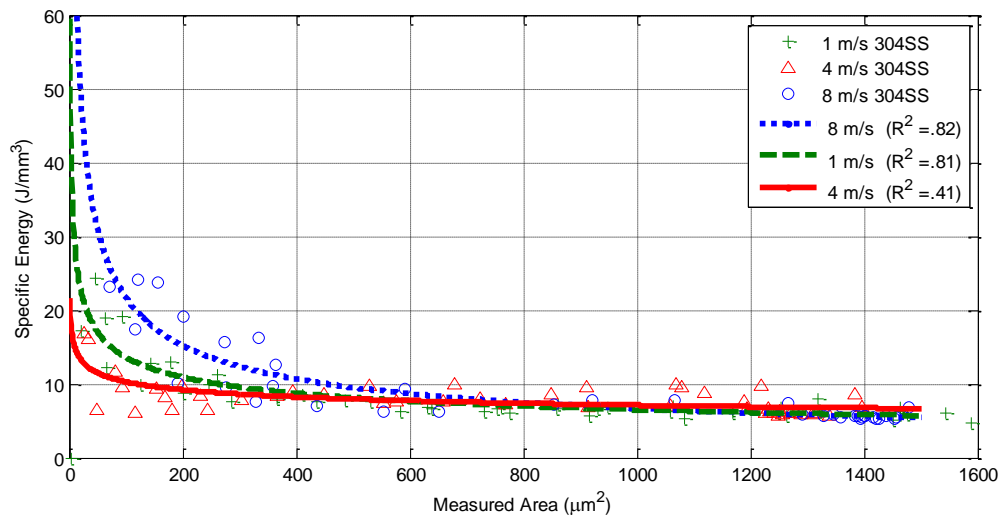


Figure 7-18. Specific Cutting Energy Comparison for 304 SS Speeds

The trends show that at 4 m/s a steady specific cutting energy regime is reached first followed closely by 1 m/s and then 8 m/s. The 8 m/s specific energy trend resembles the 52100 steel from Figure 7-16. The 1 m/s and 4 m/s speeds are close together and could be within a range of noise to each other. The distinctiveness of the experiments could be improved by testing more than three grits at each speed. If the cutting energy trends are correct there appears to be an optimal, lowest cutting energy trend, speed between 1 m/s and 8 m/s. A comparison with faster speeds up to about 20 m/s and more speeds between 1 to 8 m/s would provide more insight to the entire cutting energy trend with respect to cutting speed in a grinding application.

Finally a comparison between the grit orientations and specific energy is provided in Figure 7-19. The orientation experiments described in Section 7.3 were plotted with respect to specific energy. Although the cutting orientation had a large impact on the forces for a given chip area as discussed in Figure 7-9 from Section 7.3, Figure 7-19 does not show a large effect on the specific cutting energy.

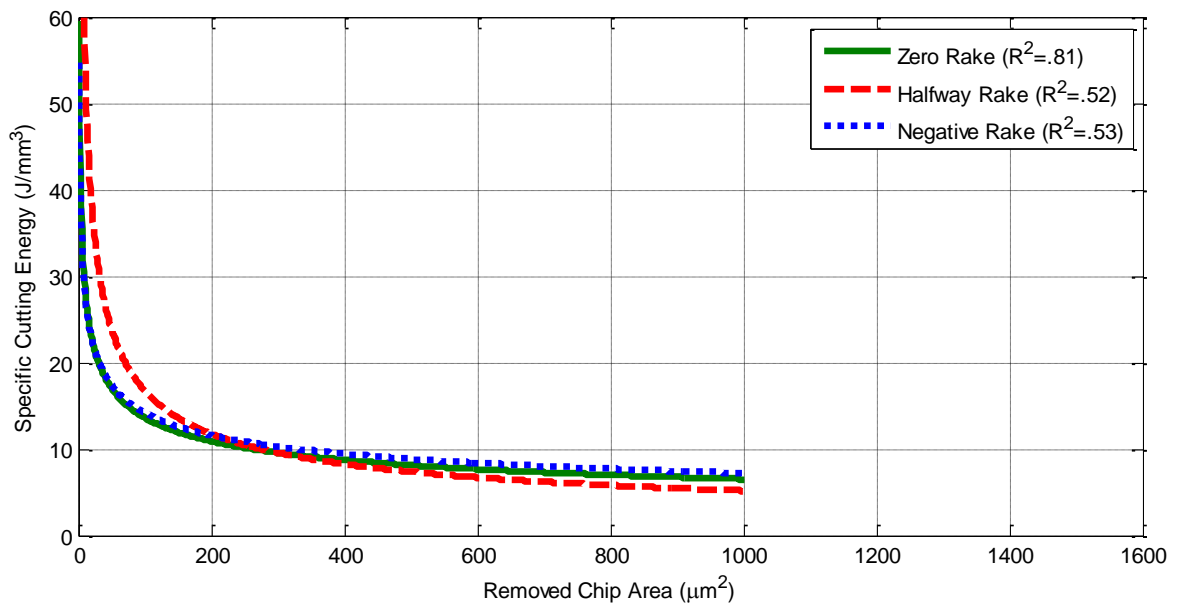


Figure 7-19. Specific Cutting Energy Comparison for Rake Orientation

Only the curves fitted to the experimental orientation data are shown. The zero and negative rake orientation follow a very similar specific energy curve while the halfway rake has a larger specific energy at lower removed material areas. The specific energy suggests that the best orientation for removing material is at one of the extreme orientations, negative or zero rakes. The curve fit for the zero rake orientation fit the data best, with a coefficient of determination of 0.81, compared to the negative and halfway rake comparisons at 0.53 and 0.52.

The performance of multiple grits acting simultaneously on a coated abrasive may act completely different than any one orientation. The zero and negative rake orientations had completely different optimal depth of cut characteristics as discussed in Section 7.3. The negative rake fractured at the large depths of cut where the zero rake orientation would continue to remove material. Even though all of the orientations had comparable removed chip areas, the specific energy with respect to depth of cut is completely different. The specific energy with respect to depth of cut is plotted in Figure 7-20. The negative rake orientation were clustered at less than 15 μm depth of cut, while the negative zero rake orientation was still able to cut at much higher depths.

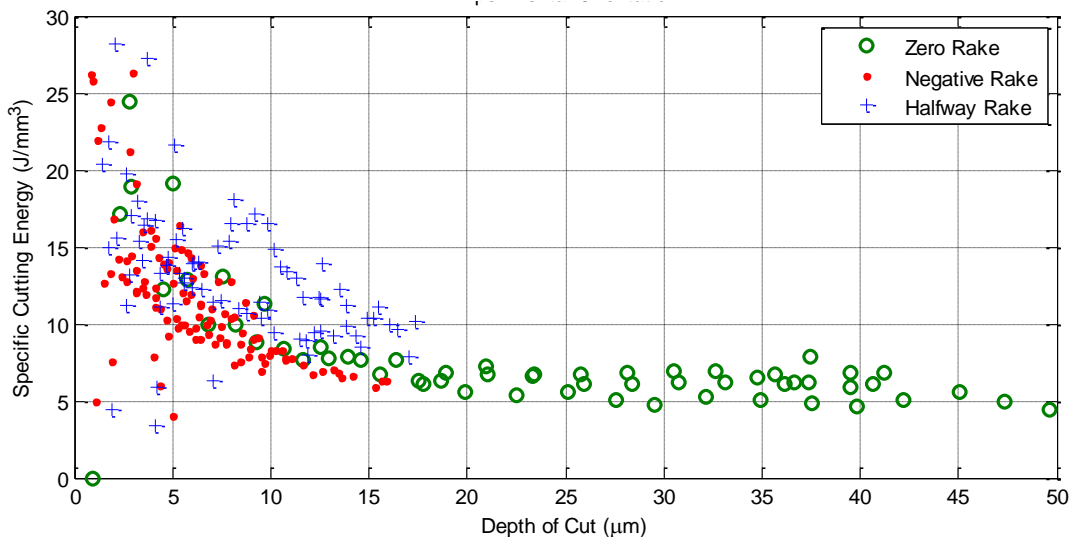


Figure 7-20. Specific Cutting Energy Comparison to Depth of Cut for Rake Orientations

At depths of cut under 15 μm , the single grit experiments could be used to compare to a coated abrasive product with an assortment of grits. The specific cutting energy results from the single grit testing could be used to assess the impact of different geometry grits, but the interplay of the orientations on a coated abrasive will most likely require further testing with a small sample of a coated abrasive.

7.5 SHEAR ANGLE MEASUREMENT IN HIGH SPEED VIDEO

7.5.1 MEASUREMENT PROCESS

High speed video was mainly used as a qualitative observation of the cutting interface described in Section 5.4. However, the high speed imaging was used for quantitative measurements of the chip shear angle from the chip speeds and workpiece surface speeds. The chip speed could be observed during experiments and it changed speeds during a single cut when occurrences such as material build up occurred. The chip speed was calculated by measuring the location of a distinct chip feature for several frames of video as shown in Figure 7-21. The change in location of the chip was then used in a velocity calculation with respect to the elapsed time between video frames.

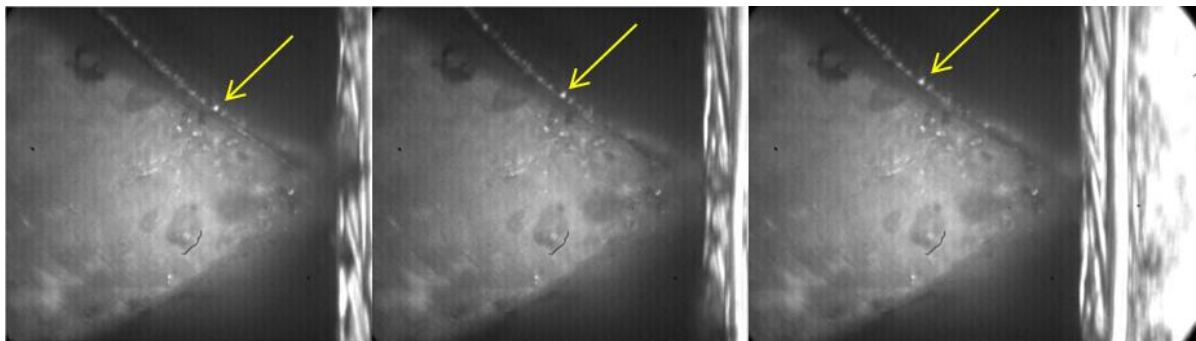


Figure 7-21. Chip Speed Calculation Images for a Negative Rake Plunge

Distances were measured on the video by measuring the displacement of a feature in pixel values and converted to micrometers by calibration (0.5578 $\mu\text{m}/\text{pixel}$). This calibration factor was determined by measuring the picture viewing window range, 440 μm by 330 μm ,

and relating the dimensions to the camera pixel location. The elapsed time between the chip displacements corresponds to the number of frames between images and the camera frame rate. In the high speed video the workpiece speed, or the surface speed, was a fixed value for each experiment based on the diameter of the workpiece and rotation speed of the spindle. The shear angle was determined by the ratio of chip speed to cutting speed via Equation (7-2) and (7-3) which is a variation of Merchant's model. Merchant [3] showed that the shear angle was related to not only the chip thickness but also speed and rake angle.

$$r_c = \frac{v_{chip}}{v_{cut}} \quad (7-2)$$

$$\tan(\alpha) = \frac{r_c \cos(\phi)}{1 - r_c \sin(\phi)} \quad (7-3)$$

where r_c is the cutting ratio of apparent chip thickness before removal to actual chip thickness or the velocity of the chip to the surface speed of the workpiece. The rake angle of the tool is ϕ , and shear angle is α as shown in Figure 7-22.

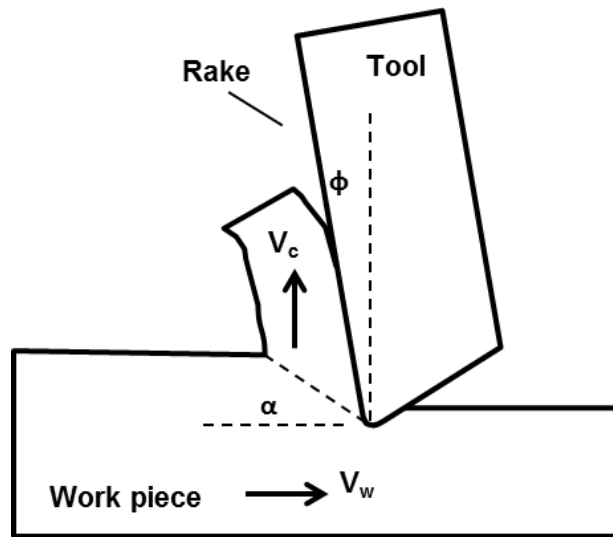


Figure 7-22. Shear Angle Relation to Chip and Workpiece Velocity

Unfortunately, cutting conditions did not always promote a good video quality to follow the chip. An increasing depth spiral experiment, described in Section 7, for the zero rake orientation is shown in Figure 7-23 for the grit depicted in the inset image. The negative rake plunge cut depicted in Figure 7-21, represented a best case imaging scenario and the increasing depth spiral cut in Figure 7-23, is considered the worst case. The zero rake orientation does not accommodate a focused grit and the increasing depth spiral experiment blocks the grit/workpiece interface by the translating workpiece. Nevertheless, as long as a feature was identified on the chip, the shear angle could be calculated. The periods of time that a distinguishing feature on a chip was visible were sometimes very short.

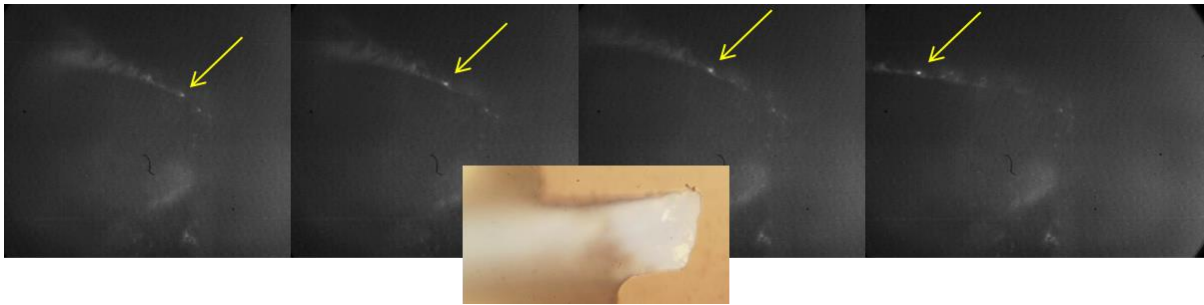


Figure 7-23. Four Contiguous Images for a Zero Rake Increasing Depth Spiral Used to Calculate the Shear Angle

7.5.2 MEASURED SHEAR ANGLE IN HIGH SPEED IMAGING

Several shear angle measurements were calculated from high speed videos for each material. However, the measured shear angles could only be taken from videos which had good visualization characteristics and did not necessarily represent shear angles for all of the experiments. The measured average chip velocity, shear angle and shear angle standard deviation is given in Table 7-2.

Table 7-2. High Speed Video Shear Angle Measurements

Material	Shear Angle	Standard Deviation	Chip Velocity (m/s)
Zero Rake 52100	16.2°	3.58	0.29
Zero Rake 1215	13.2°	0.33	0.23
Zero Rake 4330V	11.0°	3.34	0.20
Zero Rake 304SS	16.5°	4.76	0.30
Negative Rake 304SS	7.2°	1.06	0.16

The standard deviation for the shear angle was different from material to material because some values were averaged from several videos and others from a single video. The method from which the shear angles were measured was dependent on if a video that had good chip characteristics was recorded. Higher speed cutting conditions for the 304SS material did not produce viable videos due to motion blur of the chip. The shear angles recorded here should only be considered as a case study of a collection of high speed videos. More shear angle data is needed to create a comprehensive correlation to shear angle from the high speed videos. A more accurate calculation of shear angles could be determined with a larger sample size but also by more readily distinguishing the rake angle besides the generic 0° or -30° rake angles that were used in Equation (7-3). Localized geometry and large edge radii of the grit could have produced larger negative rake angles which would have decreased the shear angle. Nevertheless, the measured values of shear angle gave general values for shear angles that were used in the Arcona tool force model in Section 8.

Further details of the measurements used to find shear angles in Table 7-2 are given for a complete understanding of the results. The average shear angle for the 52100 steel was calculated from two different experiments under the same conditions in an increasing depth spiral cut. The 1215 steel was averaged between two shear angles that were recorded during the same cutting experiment, which is most likely the reason for a very low standard deviation compared to the other materials. The 4330V shear angle was taken from five

measurements during a single experiment. The measurements ranged from the very beginning of the experiment to the very end, covering a wide range of depths of cut. The 304 SS shear angle consisted of two experiments where several shear angles were from each experiment.

7.5.3 SHEAR ANGLE WITH ERNST AND MERCHANT MODEL

The high speed video shear angles were compared to the Ernst and Merchant [31] model for shear angles, given in Equations (7-4) and (7-5). The Ernst and Merchant model gives an estimation for the shear angle, α , in terms of the rake angle, ϕ , friction angle, ψ , and cutting and thrust forces, P_c and P_t [7,31]. Forces were taken from the experimental data and were used in the calculations in conjunction with the nominal rake angle value, 0° or -30° ; results are shown in Table 7-3.

$$\tan \psi = \frac{P_t + P_c \tan \phi}{P_c - P_t \tan \phi} \quad (7-4)$$

$$\alpha = 45^\circ - \frac{1}{2}(\psi - \phi) \quad (7-5)$$

Samples of the cutting and thrust data were used to calculate the shear angles from the Ernst and Merchant model. The experimental force data used in the model were the forces that correlated to specific profile area measurements, described in Section 6.2.4. This same force data was displayed in Sections 7.1 to 7.3. The model was also used to calculate separate shear angles for the 4 m/s and 8 m/s stainless steel material. These shear angles were not identified from high speed videos because the chip speed was too fast to distinguish features, also referred to as motion blur. The Ernst and Merchant model values were consistently higher than the measured shear angle values except for the 52100 steel.

Table 7-3. Shear Angles for Ernst and Merchant [31] Model

	Video Shear Angle	Model Shear Angle
Zero Rake: 304 SS at 1 m/s	16.5°	20.5°
Zero Rake: 304 SS at 4 m/s	---	19.7°
Zero Rake: 304 SS at 8 m/s	---	18.8°
Zero Rake: 4330V Steel	11.0°	24.1°
Zero Rake: 1215 Steel	13.2°	23.8°
Zero Rake: 52100 Steel	16.2°	12.7°
Negative Rake: 304 SS	7.2°	16.3°

The shear angles for the 304 SS and 52100 steel at the zero rake orientation are comparable to the values measured with the high speed video imaging. However, in comparison to the high speed video the rest of the experimental test conditions were overestimated by the Ernst and Merchant model. The difference in the shear angles results could be due to the estimated nominal shear angle. The localized geometry is most likely representative of a rake angle that is lower than the nominal rake angle used in both the high speed video and Merchant model due to the blunt edge of the grit. The modeled shear angle could also be skewed by the cutting and thrust forces. An example of the force variation is a tool with a large flank contact area. The flank face may not directly impact chip conditions at the rake face but would change the ratio between cutting and thrust forces. Therefore, the measured shear angles with respect to chip velocity are more indicative of the chip characteristics than the forces used in the Ernst [31] model. Although the Ernst [31] model may be convenient, directly measuring chip characteristics is recommended for calculating shear angle.

8 MODELLING RESULTS

8.1 EXPERIMENTAL COMPARISON TO THE ARCONA MODEL

8.1.1 MODEL PARAMETERS

The effectiveness of the model at predicting cutting forces for a single grinding grain was investigated. The alumina friction coefficients on each workpiece material were unknown so a best fit trend line was taken for the Arcona force model with the friction factors as the variables. The validity of the fitted friction factors were then compared as a verification of the model. The measured chip area, flank area, and cutting or thrust forces were used from Sections 7.1, 7.2, 7.3 while the shear angle was used from Section 7.5. The best fit friction factors for each material are given in Table 8-1 through Table 8-5. The rest of the modeled parameters needed for the Arcona model are provided in a table above each figure.

The comparison of data was only plotted with respect to removed chip area, assuming the experimental force variance due to flank contact area was a minimum. This was done for the sake of presenting data in a two dimension figure. However, because the Arcona model takes into account both the removed chip area and flank contact area; the plots with respect to removed chip area can be used as a relative comparison to show the effect of flank contact area on the variation of the forces.

8.1.2 MODEL COMPARISON

The model parameters for 304 SS are given in Table 8-1 for the cutting and thrust forces that are plotted in Figure 8-1 and Figure 8-2. The 304 SS data at 1, 4, and 8 m/s surface speeds were all used in the model to define a single trend. The modeled correlation for the Arcona model to the experimental results has one of the best coefficients of determination in relation to all of the experimental data, but is still low at $R^2 = 0.72$ and 0.28 for cutting and thrust forces. The model also deviates more at larger removed workpiece areas.

Table 8-1. 304SS Model Parameters

Hardness, H	Modulus of Elasticity, E	μ	μ_f	Shear Angle, α
2.202 GPa	193 GPa	1.299	1.243	16.5°

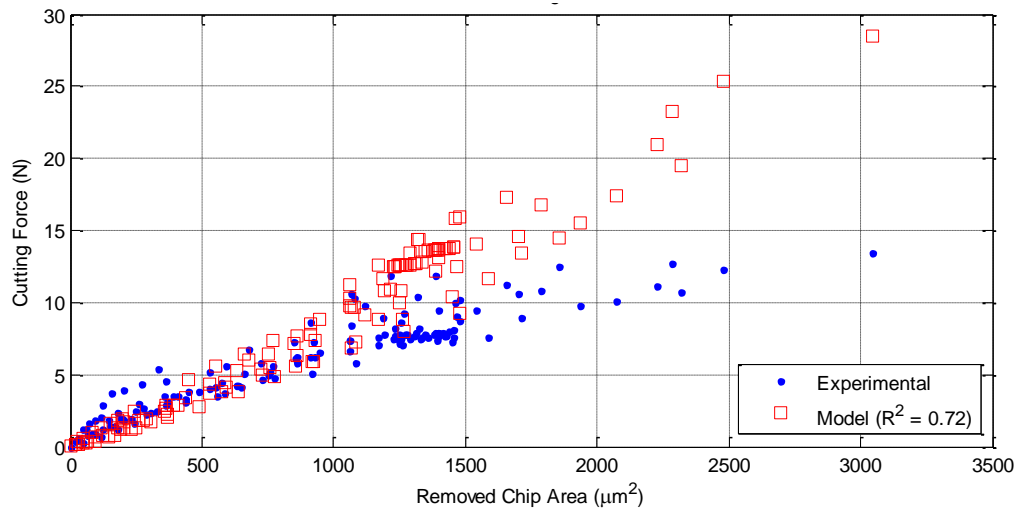


Figure 8-1. 304 SS Cutting Force: Experiment and Modeled Fit

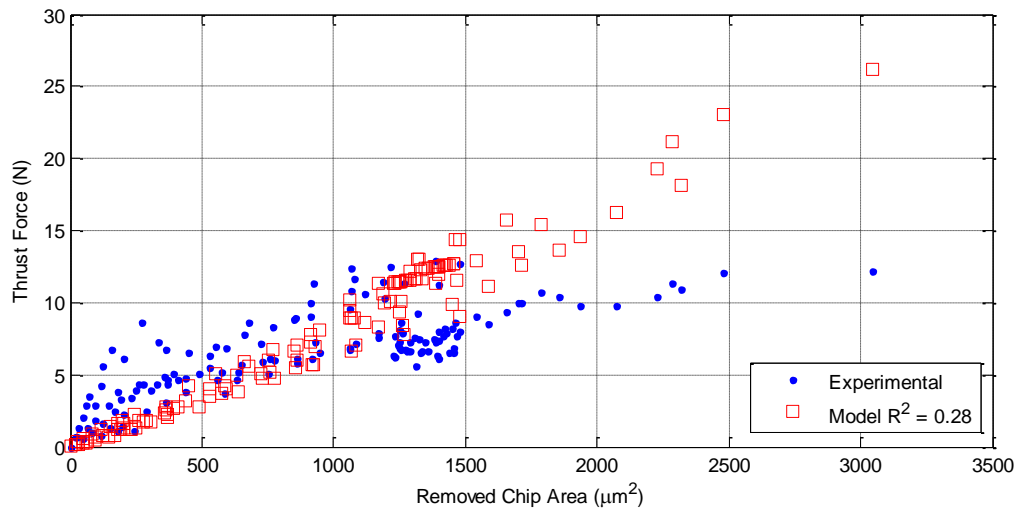


Figure 8-2. 304SS Thrust Force: Experiment and Modeled Fit

The model parameters for 4330V steel are given in Table 8-2 and experimental results are plotted in Figure 8-3 and Figure 8-4. The model largely differs from the experimental forces at the single depth of cut experiment. The single depth of cut experiment for the 4330 steel is shown by the area data cluster between $1300 \mu\text{m}^2$ to $1400 \mu\text{m}^2$. The Arcona model correlation to experimental data has a cutting and thrust coefficient of determination, R^2 , of 0.59 and -0.22 but follows the average trend of force data well (the experimental data had a large data spread).

Table 8-2. 4330V Model Parameters

Hardness, H	Modulus of Elasticity, E	μ	μ_f	Shear Angle, α
2.74 GPa	200 GPa	0.4338	0.8191	11°

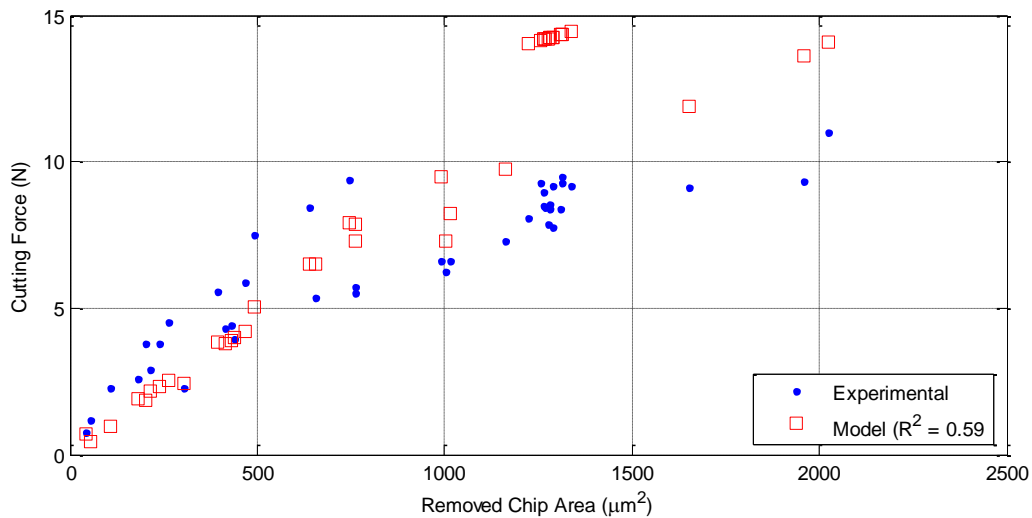


Figure 8-3. 4330V Cutting Force: Experiment and Modeled Fit

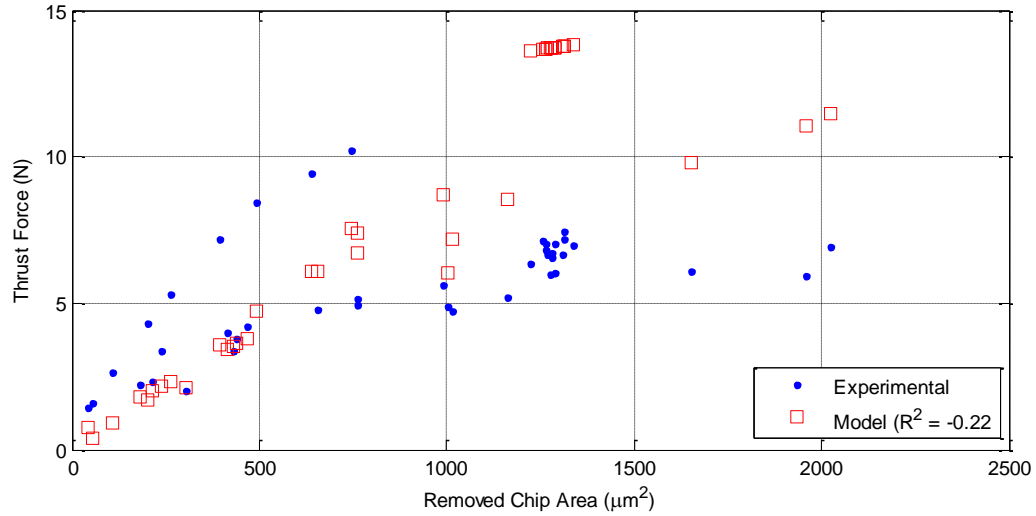


Figure 8-4. 4330V Thrust Force: Experiment and Modeled Fit

The model parameters for 1215 steel are shown in Table 8-3 and are compared with the experimental results in Figure 8-5 and Figure 8-6. The Arcona model deviated from the experimental 1215 steel trend after about $1000 \mu\text{m}^2$ removed chip area, which resulted in a coefficient of determination of 0.38 and 0.30 for the cutting and thrust forces.

Table 8-3. 1215 Model Parameters

Hardness, H	Modulus of Elasticity, E	μ	μ_f	Shear Angle, α
1.85 GPa	200 GPa	1.203	1.867	13.2°

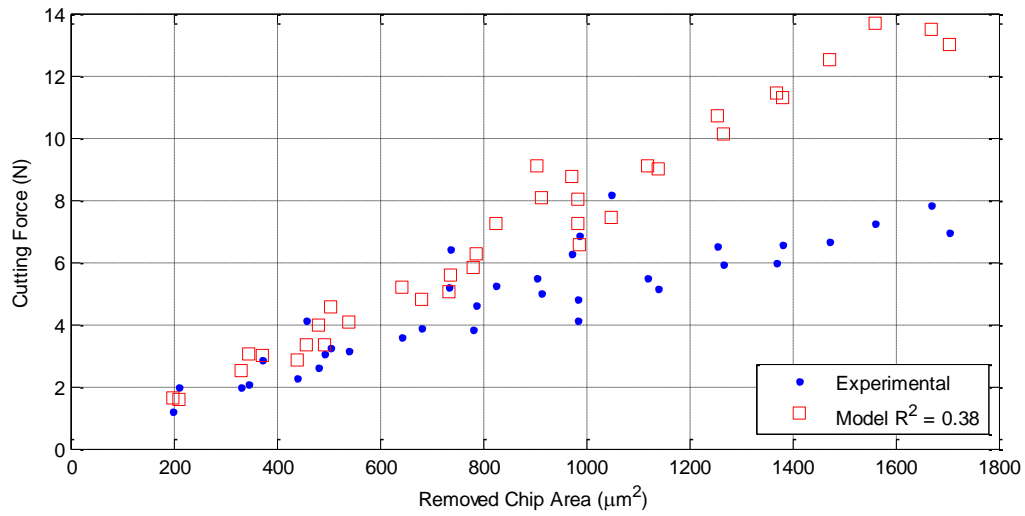


Figure 8-5. 1215 Cutting Force: Experiment and Modeled Fit

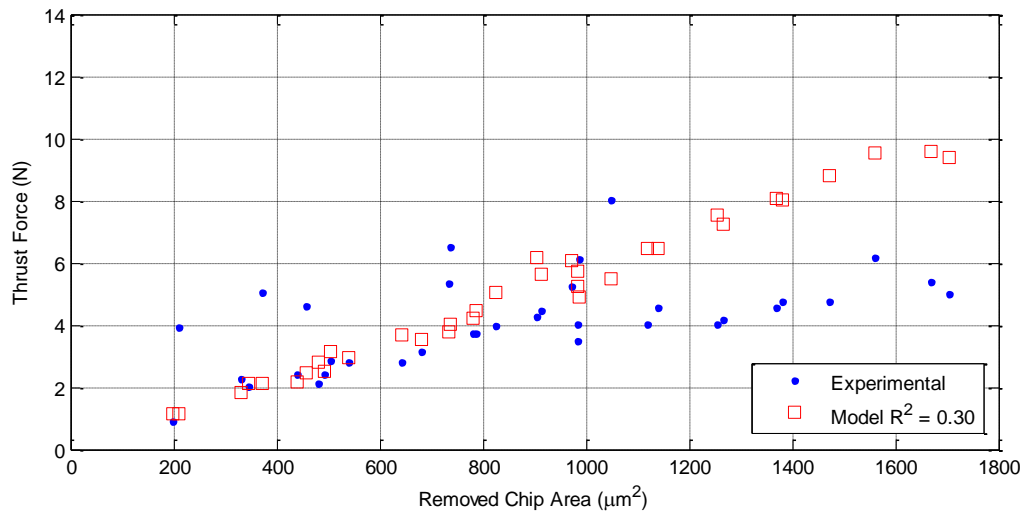


Figure 8-6. Thrust Force: Experiment and Modeled Fit

Model parameters for 52100 steel are described in Table 8-4. Figure 8-7 and Figure 8-8 compare the experimental and modeled forces. The coefficient of determination is 0.19 and -0.32 for the cutting and thrust forces, but still followed the overall trend of experimental data.

Table 8-4. 52100 Model Parameters

Hardness, H	Modulus of Elasticity, E	μ	μ_f	Shear Angle, α
8.224 GPa	210 GPa	0.1897	0.2488	16.2°

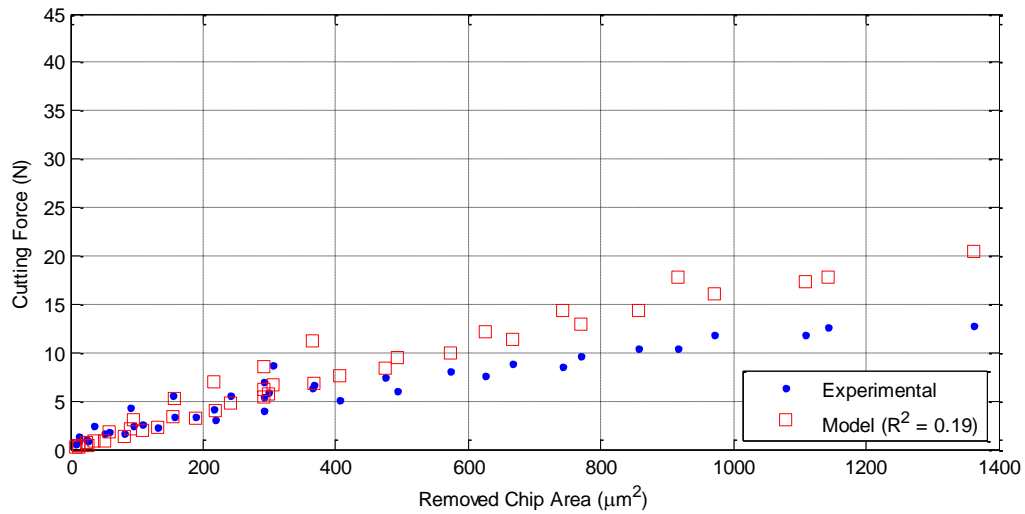


Figure 8-7. 52100 Cutting Force: Experiment and Modeled Fit

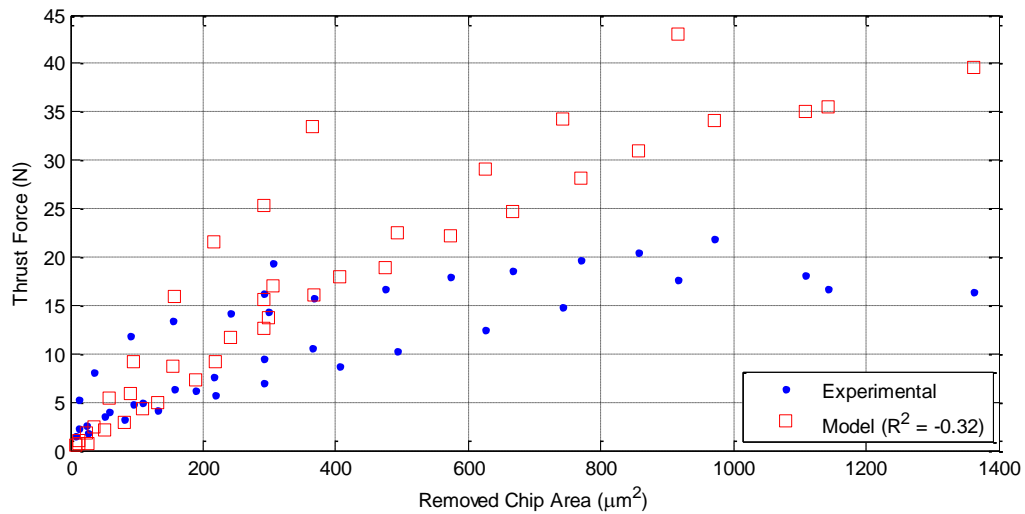


Figure 8-8. 52100 Thrust Force: Experiment and Modeled Fit

The negative rake orientation experiments, for 304 SS workpiece material, are plotted with the model in Figure 8-9 and Figure 8-10 while the modeled parameters are in Table 8-5. The negative rake orientation has the best fit to the Arcona model, with R^2 values of 0.87 and 0.77 for cutting and thrust forces, but also has the highest predicted friction factors.

Table 8-5. 304 SS Negative Rake Model Parameters

Hardness, H	Modulus of Elasticity, E	μ	μ_f	Shear Angle, α
2.202 GPa	193 GPa	2.418	6.289	7.2°

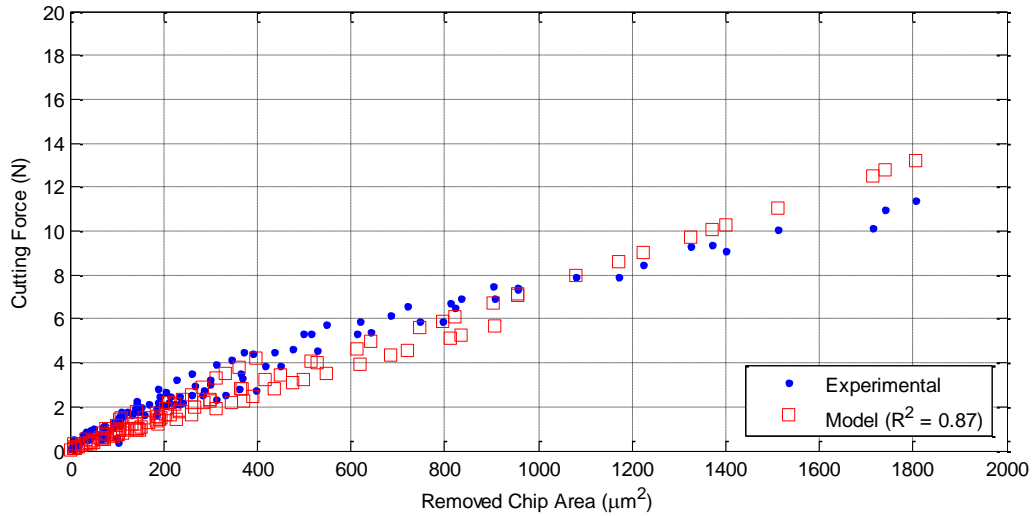


Figure 8-9. Negative Rake Orientation Cutting Force: Experiment and Modeled Fit

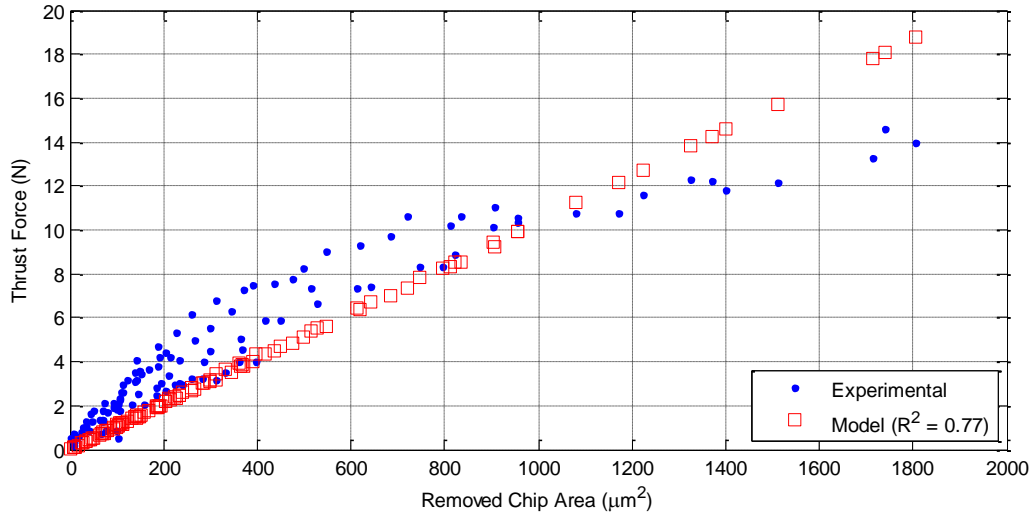


Figure 8-10. Negative Rake Orientation Thrust Force: Experiment and Modeled Fit

8.1.3 CONCLUSIONS REGARDING THE ARCONA MODEL

The Arcona model was used as a comparison to experimental forces and as a basis to better define contact geometry. Defining contact geometry, based on the Arcona model geometry, proved successful to compare experimental results to each other, but the model did not compare to experimental results as well. The modeled results for the friction factors of the 304 SS and 1215 steel materials seemed too high for realistic coefficients. The coefficients of friction for the 4330V and 52100 steels are within a wide range of reasonable friction coefficients. However there were no comparisons for the friction values for the given machining conditions. Reasonable coefficients were considered to be in the range of 0 to 1 while a friction coefficient higher than 1 was considered unreasonable. The best correlation to the Arcona model occurred for the negative rake orientation, but also produced the largest friction coefficients.

The Arcona model was originally used in diamond machining with a well-defined tool but did not work as well with loosely defined grit geometry of the shaped alumina grits. The loose geometry and large nominal cutting radius of the grit is much different than a diamond tool that has a sharp cutting edge radius of 50 nm. The model deviated more from

experimental forces as the chip area was increased. At a removed chip area around $1000 \mu\text{m}^2$ the model had a different force slope than experimental data which could be a different cutting regime trend. The Arcona model was originally developed and used for removed chip areas under $1600 \mu\text{m}^2$. For larger removed chip areas and even larger radius tools, like the shaped alumina grits, the model may need to be modified.

The Arcona model deviation from experimental results could have been due to the non-planar shaped alumina grit faces and large cutting edge radiuses with respect to the depth of cut. In the case of the shaped alumina grits, the cutting and thrust forces were most likely due to the large cutting edge radiuses that could result in sizing effects such as plowing. The specific geometry of the cutting edge could impact the forces in a different way than a geometrically well-defined diamond tool. Further experiments with the Arcona model could seek to define a new parameter that impacts forces when the cutting edge radius is close to the depth of cut.

8.2 FINITE ELEMENT THIRD WAVE ADVANTEDGE MODELS

8.2.1 BACKGROUND

Third Wave AdvantEdge is a FE modeling software for material removal processes that calculates the shape and thickness of the chip, the cutting and thrust forces and the tool/workpiece temperatures based on machining conditions and tool/workpiece properties. The FE model solves the mechanical and thermal problem at each time step and iterates the results to reach a solution. The model repeats the steps as the tool progresses into the workpiece and a chip is formed. The program features adaptive re-meshing to resolve characteristics such as the primary and secondary shear zones in the chip and takes into account the effects of friction and conduction at the interfaces. AdvantEdge allows the user to see numerous results such as the tool forces, tool/workpiece temperatures, strains, strain rates, stress, pressure, and velocity components. However depending on the parameters used, the simulation can be quite time consuming, 2-5 hours of simulation to do a few milliseconds of cutting time to reach a steady state condition. Third Wave models could supplement single grit testing if it could be validated as an accurate model.

AdvantEdge has been used to model and compare experimental chip morphologies [32] and has been compared side-by-side with other finite element packages [33]. In one study [32] the chip morphologies produced comparative results to the chip dimensions while Bil et al [33] described mixed results. To determine if Third Wave would be successful to model single grit experiments, the model was compared with experimental results.

8.2.2 FINITE ELEMENT ANALYSIS PARAMETERS

A 2D turning simulation was used to represent the experimental for single point turning. The AdvantEdge model in 2D mode allows the user to input cutting parameters and basic tool geometry. To represent the alumina grit, geometries were assumed to be simple and uniform. A single model was used for each grit orientation while parameters such as depth of cut and contact width were varied to represent the experimental conditions. AdvantEdge defines the depth of cut and feed in a different way than they have been referenced in this thesis. The depth of cut in AdvantEdge refers to the contact width of the tool and chip. The depth of cut has been referred to as the tool width within previous context. The Third Wave feed parameter has generally been referred to as the cutting depth or depth of cut in previous sections. Figure 8-11 shows the AdvantEdge parameters and what conditions they govern. The Third Wave terminology for each parameter will only be used within this FE modeling section and will be placed in parentheses.

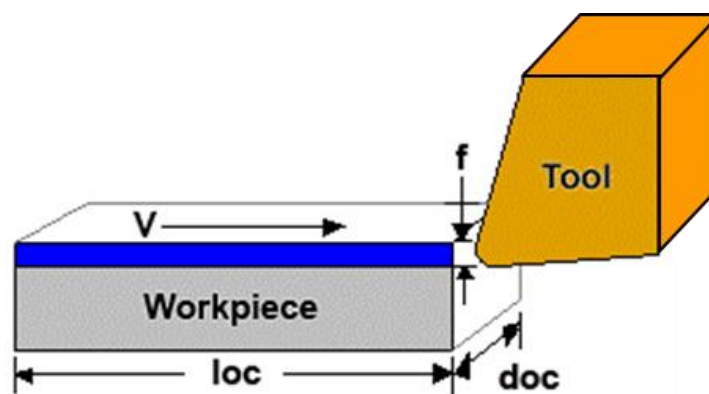


Figure 8-11. AdvantEdge Parameter Description [34]

The dominant parameters, that were modeled in AdvantEdge, which resembled experimental conditions, are given in Table 8-6. A recommendation by Bil et al [33] was to adjust the friction factor to resemble experimental results. The friction factor was set at a constant of 0.8 for each material because it matched the average ratio of thrust to cutting forces similar to experiments. The width of the cut (depth of cut, doc) and depth of cut (feed, f) were varied to match experimental areas as described in the next section for the geometry relation.

Specific meshing characteristics were needed to successfully complete simulations without simulation errors. The meshing characteristics were mostly set to default values and then modified to improve meshing characteristics, except the minimum element size was set to 5 μm .

Table 8-6. Modeling Parameters

Parameter	Value
Tool Material	Alumina
Workpiece Material	304SS, 1118, 52100
Tool Radius	20 μm
Friction	0.8
Initial Temperature	20°C
Length of Cut (loc)	1 mm
Min. Element Size	5 μm
Velocity (V)	1 m/s unless noted

The workpiece characteristics were matched to the experiments with a few exceptions. The Third Wave material library had 304SS and 52100 steel with comparable hardness values to the experimental workpieces. However, 1118 steel was used as a default Third Wave material in place of the 1215 steel. 1118 steel was determined to an acceptable material for replacement with similar properties.

The 4330V steel was not included in simulation results since the closest material was 4340 steel. Judging from experiments, the experimental 4330V was not in the hardened condition. The Third Wave 4340 would not have been similar enough to the experimental 4330V. AdvantEdge has an option to modify hardness characteristics but the materials had over a 20% difference in hardness and Third Wave recommended not modifying the hardness past 20% [34].

8.2.3 FEA MODEL AND EXPERIMENTAL GEOMETRY RELATION

The modeled depth of cut (feed), width of cut (depth of cut), and tool geometry had to be slightly modified from experimental conditions to fit the AdvantEdge model. The tool was modeled with a 20 μm cutting edge radius and either a 0° or -30° rake angle as shown in Figure 8-12. A custom tool was modeled for the negative rake orientation while a standard AdvantEdge tool, with a modified cutting edge radius, was used for the zero rake orientation. The tool was assumed to be flat and smooth, representing the nominal geometry of the grit.

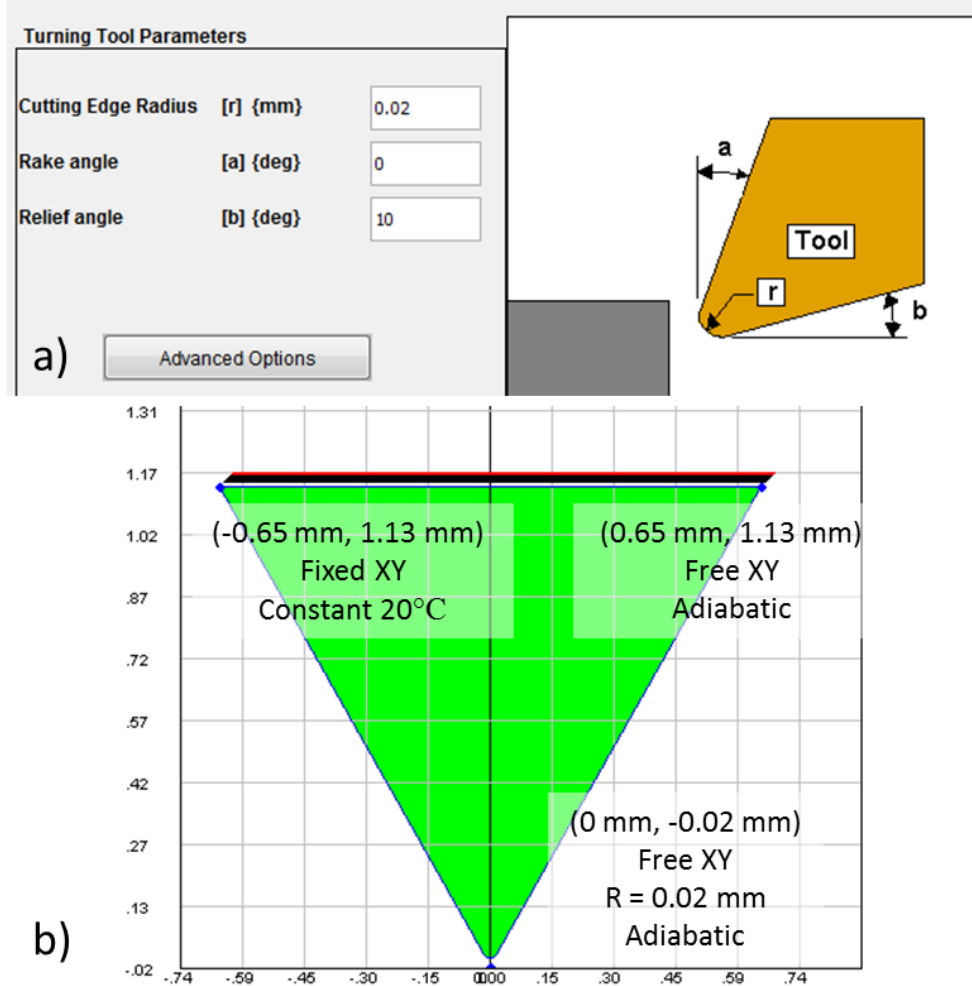


Figure 8-12. Tool Geometrical Parameters for a) Zero Rake, b) Negative Rake

For the two orientation models in Figure 8-12, the width of the tool (depth of cut, d_{oc}) was a constant value. In the 2D AdvantEdge model, the grit width is assumed to be a constant, uniform width so force results could be simulated. The uniform width represented the negative rake tool geometry well; however experimentally the zero rake orientation had a strong dependence on tool width based to the depth of cut. The triangular width of the zero rake angle orientation was adapted to be a rectangular area that fit the same cutting area as the triangular area. The average triangular width of the triangular face was used as the

approximate width in the model. This way the removed material area and depth of cut would be equivalent as shown in Figure 8-13.

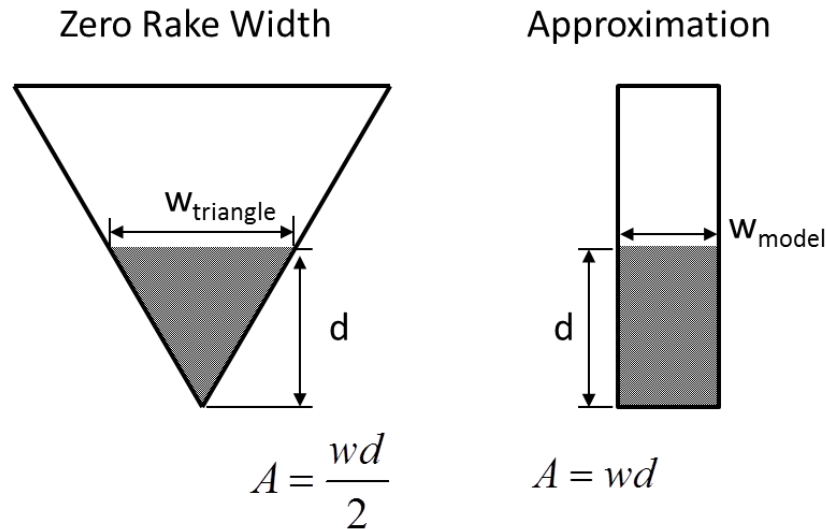


Figure 8-13. Zero Rake Width Approximation for AdvantEdge

The AdvantEdge geometry for the zero rake angle tools were determined by fitting the experimental removed chip area, A , with respect to the measured depth of cut, d . The area was then modified to a rectangular area by dividing the area by the depth, following the equation for a rectangular area. The resulting equation should represent the rectangular width that was used as a model dimension in AdvantEdge. This provided the Third Wave models with a similar removed chip area for each experimental depth according to Equation (8-1) where α and β are dummy variables representative of the specific curve fit. This same method was used for the width of the negative rake orientation tool. The negative rake orientation was close to rectangular chip geometry, but still had a variable width due to the localized geometry at the tip of the grit. The depth of cut was modeled at 10, 20, 30, and 40 μm depths for the zero rake orientation and at 5, 8, and 15 μm depths for the negative rake orientation.

$$A_{\text{experiment}} = \alpha d^2 + \beta d \tag{8-1}$$

$$W_{\text{model}} = \frac{A}{d} = \alpha d + \beta$$

8.2.4 EFFECT OF SPEED ON 304 SS IN ZERO RAKE ORIENTATION

Each individual grit was different at the micrometer scale, but the generalized AdvantEdge parameters were used to represent the average experimental results. A comparison is given for both the thrust forces and cutting forces. All graphs are plotted with force on the y axis and the removed chip area on the x axis. The effect of speed was compared for the stainless steel material in Figure 8-14 and Figure 8-15 at 1, 4, and 8 m/s surface speeds.

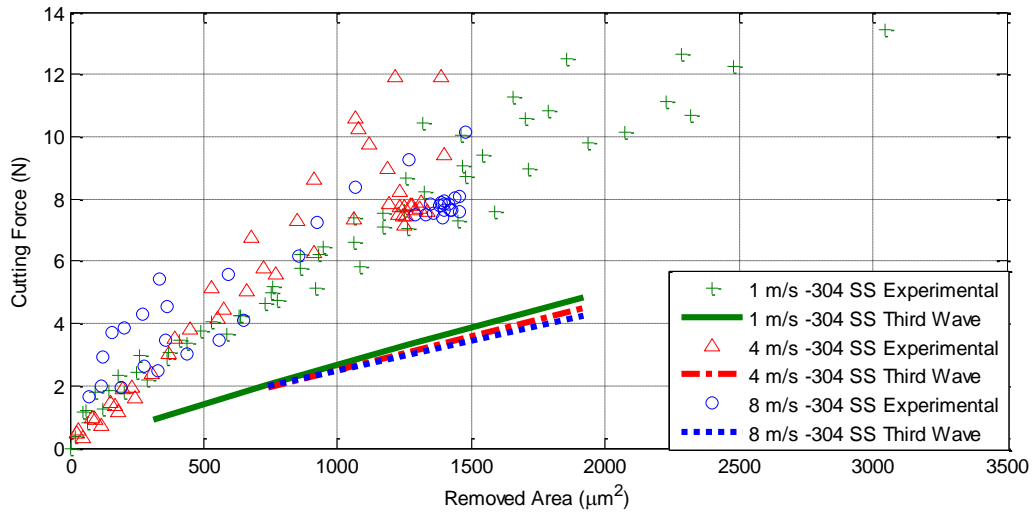


Figure 8-14. 304 SS Speed and Cutting Force Comparisons to Third Wave

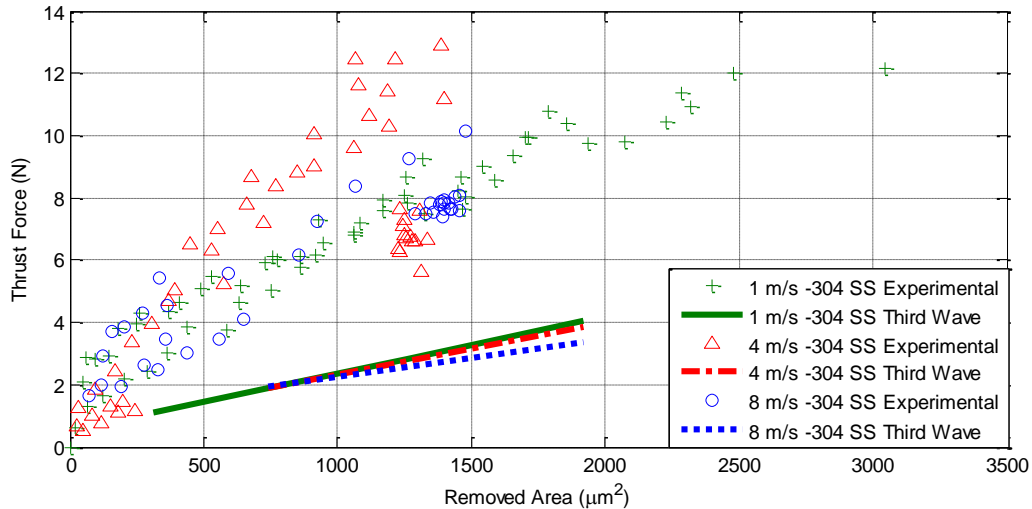


Figure 8-15. 304 SS Speed and Thrust Force Comparisons to Third Wave

The AdvantEdge model deviates significantly from the experimental forces. In both the model and experiments, the cutting speed has little distinguishable effect on the overall forces. However, the model shows that increasing cutting speed should decrease the forces slightly while experimentation showed a different effect. As described within the experimental data comparison of Section 7.1, the overall relations of speeds were that the 4 m/s speed had the highest force followed by the 1 m/s and 8 m/s speeds. The modeled forces for speeds are about 54% lower than the experimental cutting forces and 61% lower for the thrust forces at 1 m/s.

8.2.5 EFFECT OF MATERIAL IN ZERO RAKE ORIENTATION

A material comparison between the modeled and experimental results is shown in Figure 8-16 and Figure 8-17 for 304SS, 1215 (1118) steel, and 52100 steel. The modeled 1215 steel was the only model to match experimental forces and is plotted again separately in Figure 8-18.

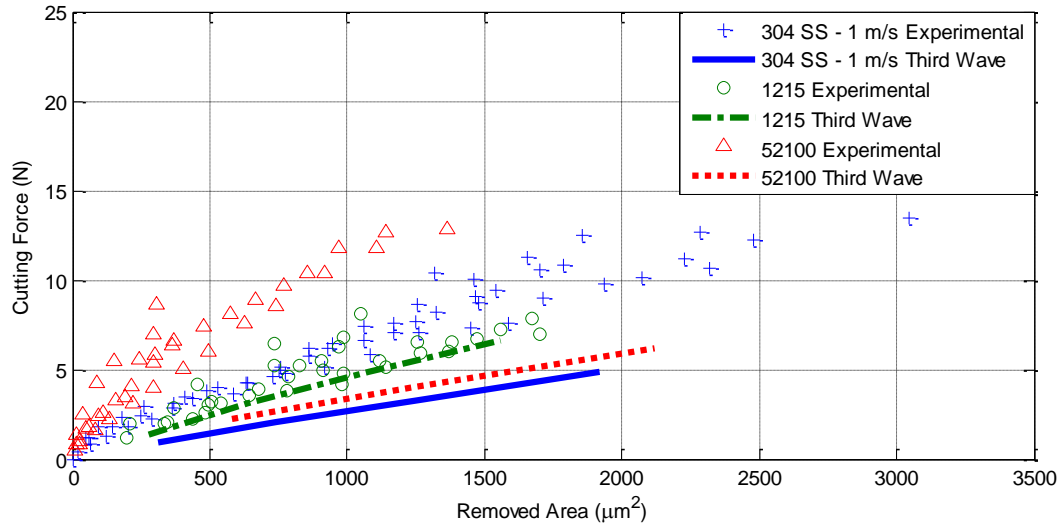


Figure 8-16. Steel Cutting Force Comparisons to Third Wave

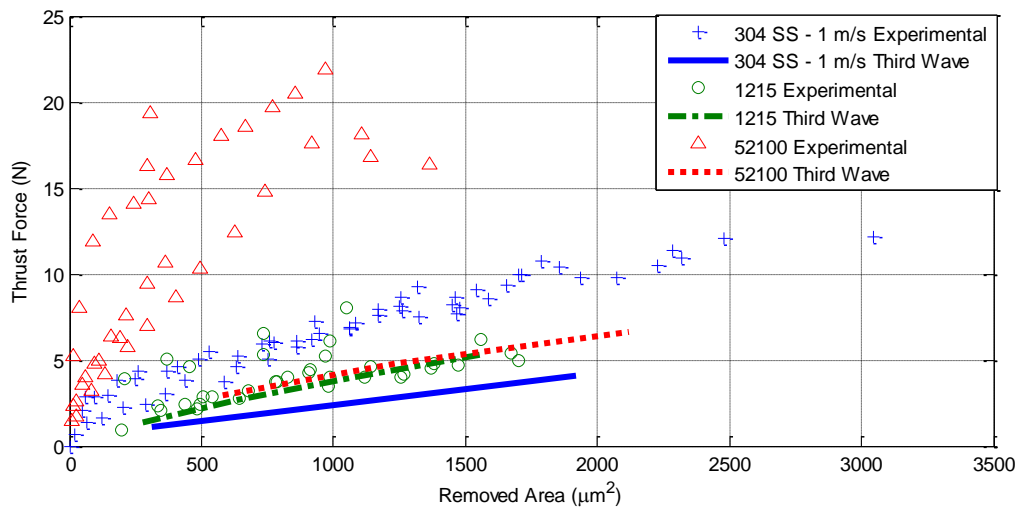


Figure 8-17. Steel Thrust Comparisons to Third Wave

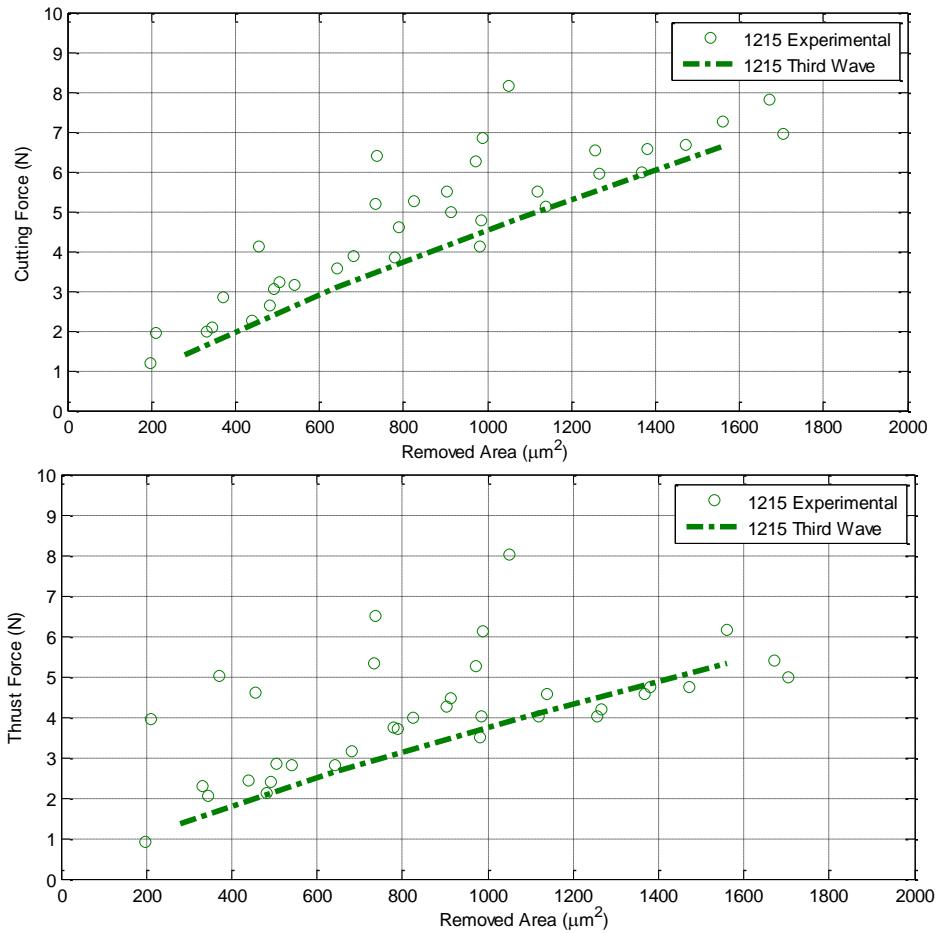


Figure 8-18. 1215 Cutting and Thrust Comparison to Third Wave

Much like the effect of speed, the material comparison deviates significantly from the experimental results with the exception of the 1215 steel. The 304 SS modeled cutting and thrust forces were on average 54% and 61% lower than experimental forces while the 52100 steel modeled cutting and thrust forces were 76% and 84% lower than experimentally found. The 1215 steel modeled cutting and thrust forces were closest to experiments and only 15% lower than experimentally found for both the average cutting and thrust forces.

The experimental trend where the force magnitudes followed the hardness was not apparent in the model. Not only does the AdvantEdge model not show a large effect of material

hardness, the modeled 1215 (1118) steel breaks the hardness trend. The modeled 1215 had the lowest hardness in Third Wave but the highest forces.

It was determined that Third Wave could not be compared to specific grit experiments because the model typically predicted forces lower than experimental results for the zero rake orientation. This could be because the 3D cutting geometry was over simplified in the models. If the tool geometry was a cause for the FEA model deviation, the large radius tool may have created experimental material flow out of the two dimensional plane of the model. Since the model is only 2D, it did not take into account the effects of the material flow out of plane. A suggestion for further modeling comparison would be to run a 3D model to see if it fit better with experiments or material flow at the tool edges. Also, the experimental contact areas have complex geometry at the tool edges which was not included in the models and was only matched to equivalent chip areas. The impact of the tool width shown in Figure 8-18 did not represent experimental forces as anticipated.

Another thought is that material pickup on the tool effected the forces in ways that were not modeled in AdvantEdge. The much higher experimental forces may have been a result of tool pickup on the 304 SS and 52100 steels. This could potentially explain why the model matched the 1215 material, which has a better machinability rating. However, both of these conjectures have no direct experimental proof.

The flank area was another parameter that was largely ignored in the models. Several models were conducted with very small tool relief angles to increase the flank contact but the results showed that lowering the relief angle had very little effect on the modeled forces. Third Wave did not allow zero or negative relief angles in the default tool. However, it may be possible to create a custom tool with a wear flat that simulated a large flank contact area. This option was not explored since most of the grits did not have a wear flat. The grits were modeled with a 20 μm radius instead.

8.2.6 EFFECT OF RAKE ANGLE

The negative rake orientation was modeled and compared to experiments on 304 SS at 1 m/s described in the experimental orientation comparison in Section 7.3. The negative rake model for cutting and thrust forces are shown in Figure 8-19 and Figure 8-20. The halfway rake orientation was not included because the geometry was too complex for the 2D Third Wave AdvantEdge models.

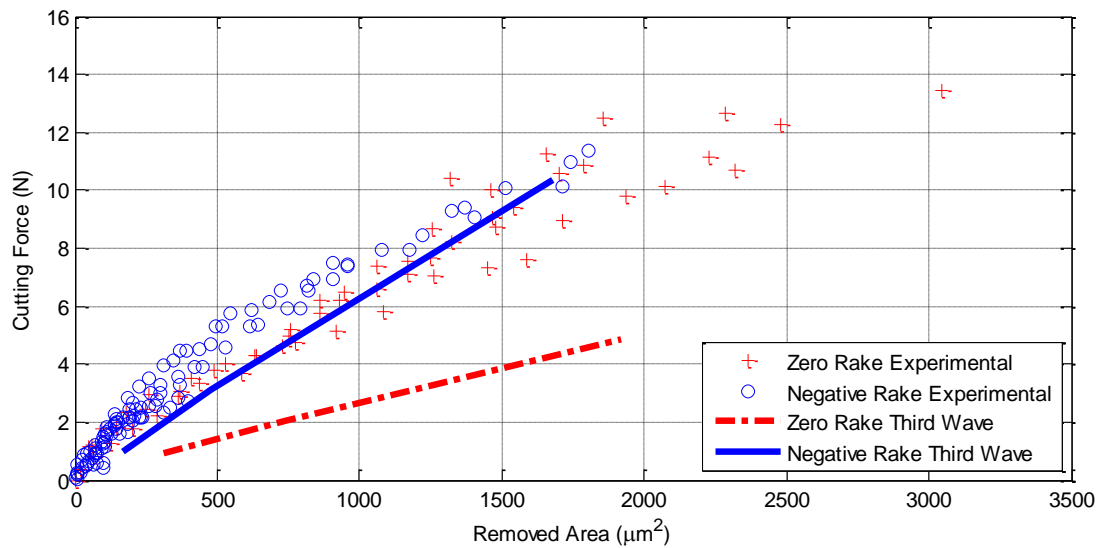


Figure 8-19. Third Wave Grit Orientation Effect on Cutting Forces at 1 m/s for 304 SS

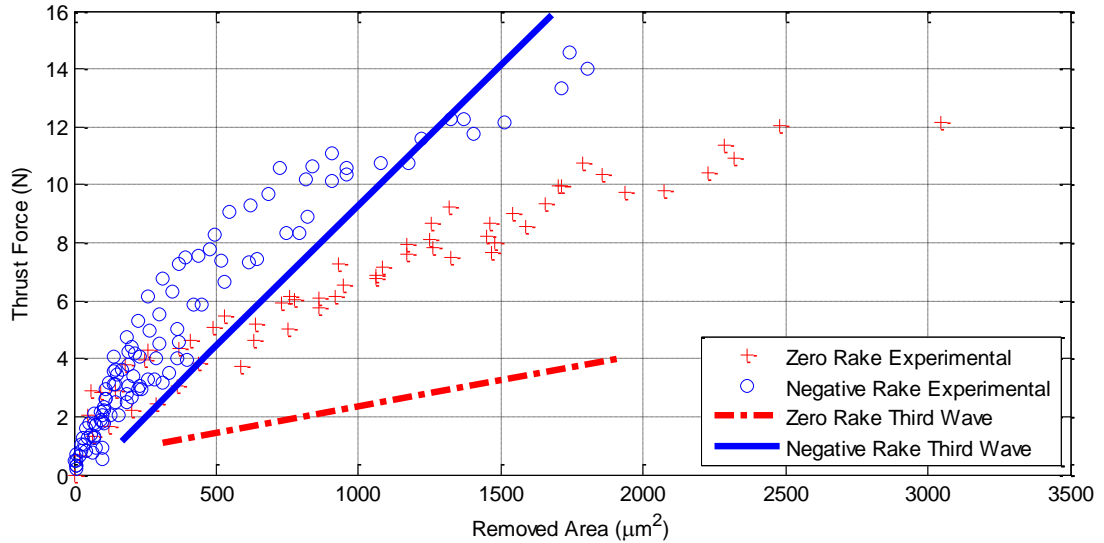


Figure 8-20. Third Wave Grit Orientation Effect on Thrust Forces at 1 m/s for 304 SS

The negative rake orientation matches both the cutting and thrust forces very well, only being 17% and 10% lower than the average experimental cutting and thrust forces. This is completely different than the disparity described in Sections 8.2.4 and 8.2.5 for the zero rake orientations.

A further investigation of the effectiveness of the Third Wave model in the negative rake angle was completed with 52100 and 1215 (1118) steels, but experiments on the materials were only successful on the 52100 steel. Negative rake orientation groove geometries were not measured on the 1215 steel because grit grooves could not be distinguished from a poor surface finish on the workpiece. This prevented an experimental measurement of the 1215 workpiece. The effect of grit orientation for 52100 steel is given in Figure 8-21 and Figure 8-22.

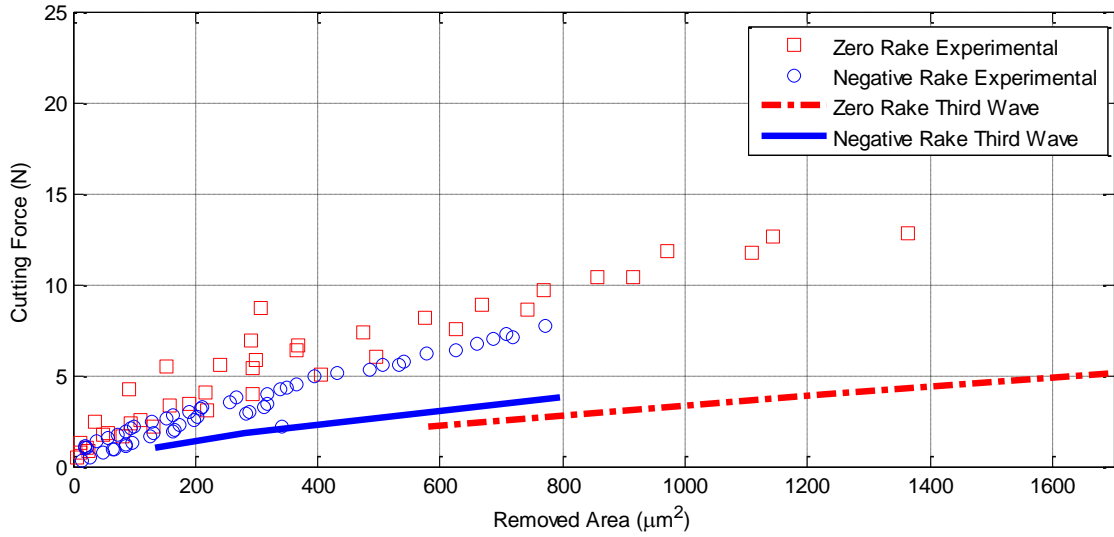


Figure 8-21. Third Wave Grit Orientation on Cutting Forces at 1 m/s for 52100 Steel

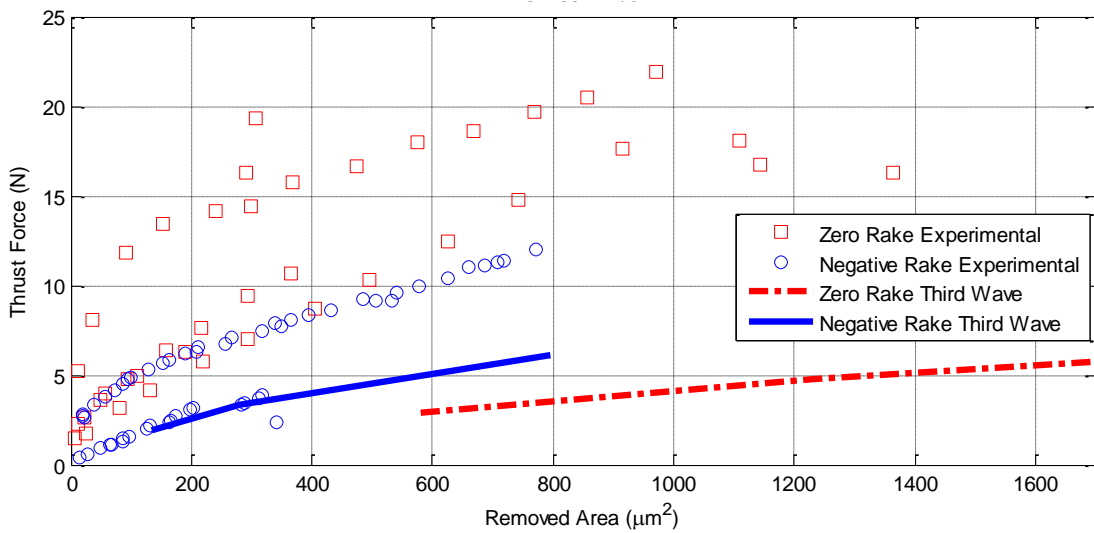


Figure 8-22. Third Wave Grit Orientation on Thrust Forces at 1 m/s for 52100 Steel

The experimental 52100 steel orientation effect was different than the 304 SS. The 52100 negative rake experiments produced 11% lower cutting and 17% lower thrust forces than the zero rake orientation experiments. It is not understood why the 52100 experiments showed

the negative rake forces decreasing from the zero rake while the 304 SS workpiece was opposite to this as described in Section 7.3.

Although the 52100 negative rake Third Wave model was similar to the 304SS material in that it increased the magnitude of the predicted forces, it did not correlate to experiments. The 52100 model under predicted the experimental cutting and thrust forces by 53%. However, the shear angle measurements from Third Wave, given in Section 8.2.8, suggest that the AdvantEdge 52100 material may not be a good representation of the experimental 52100 steel. Further information is given in that section. Looking at the simulations as a whole, the negative rake comparison suggests that the Third Wave models may only match specific cases of cutting. 304 SS at the negative rake orientation is an example of Third Wave matching well with experiments.

The Third Wave model could be further used to determine what models resemble experimental cases, but a comparison to experimental data will be needed to determine the validity of the model. Further manipulation of the AdvantEdge materials (through custom properties) may produce a more accurate resemblance to experiments, but for the tested parameters it does not.

The method for estimating tool contact width, in the Third Wave model, works better for the negative rake orientation and may be the cause of the zero rake discrepancy between experimental and modeled forces. As suggested in Section 8.2.5 for the zero rake tools, using a 3D model could improve material flow characteristics for the alumina grits that do not follow the geometry of a well-defined cutting tool.

8.2.7 THIRD WAVE MODEL TEMPERATURE

The AdvantEdge software calculates a peak tool temperature and temperature distribution in the grit, chip, and surrounding workpiece. Unfortunately, there are no experiments to compare the temperatures from the model, and only the modeled results are given. The thermal boundary conditions were a constant temperature of 20°C on the top of the tool and adiabatic on all other surfaces or set by default and shown in Figure 8-12 for the zero and

negative rake orientations. The peak tool temperatures for 304 SS based on speeds are plotted in Figure 8-23. This is the same simulation that was used for the results in Figure 8-14. The model shows that cutting speed greatly affects the peak tool temperature. The figures are marked with a point where each Third Wave data point was modeled, and the data points are connected with a linear interpolation between each point. The interpolation is given to show a general trend for temperature, not as a specific interpolation that the temperature follows.

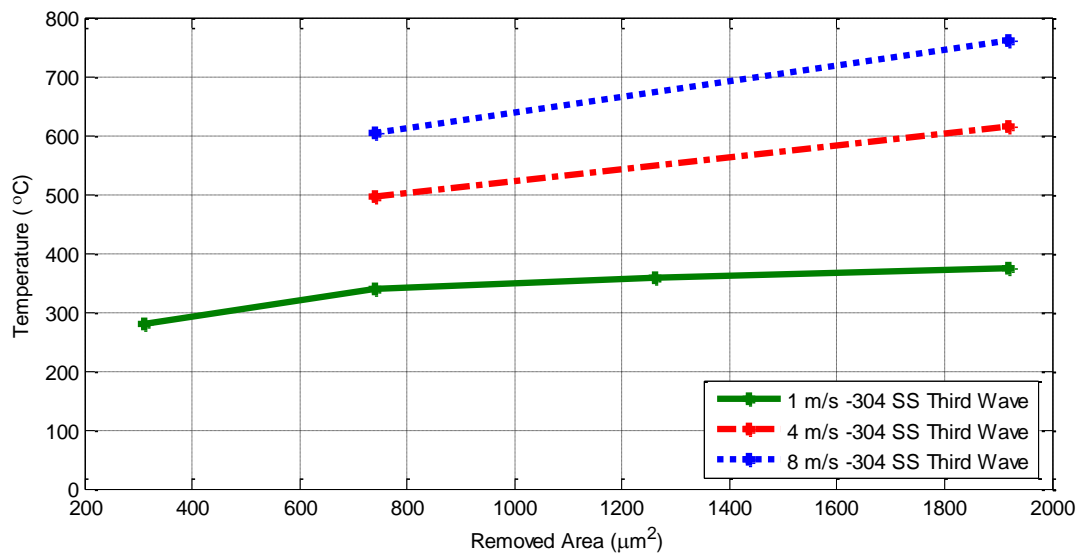


Figure 8-23. 304 SS Peak Tool Temperatures at 1, 4, and 8 m/s Cutting Speed

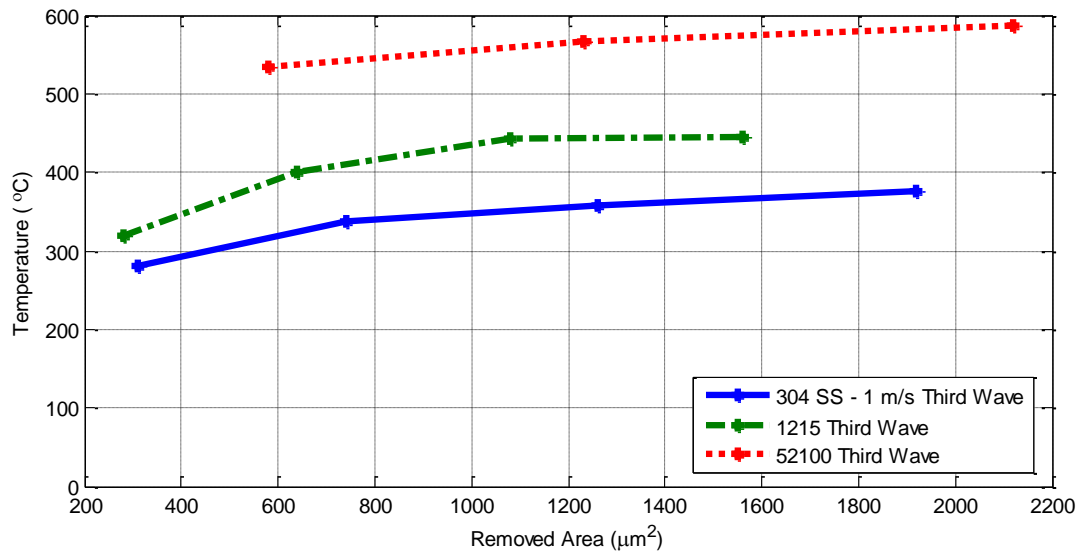


Figure 8-24. Peak Tool Temperatures of Steel Workpieces

The thermal properties for the default materials in Third Wave were not displayed for the user, but the combination of cutting parameters and material properties had a significant impact on the predicted tool temperature as shown in Figure 8-24.

The AdvantEdge temperature contour plot for 304 SS, 1215 steel, and 52100 steel are given in Figure 8-25 to Figure 8-28 for identical simulation parameters. Each model represents a 1 m/s cut at a depth of cut (feed, f) of 20 μm except for the negative rake orientation which is at a 1 m/s cut and depth of cut (feed, f) of 8 μm . The overall depth of the negative rake orientation was different to more accurately resemble a typical depth of cut for the negative rake orientation.

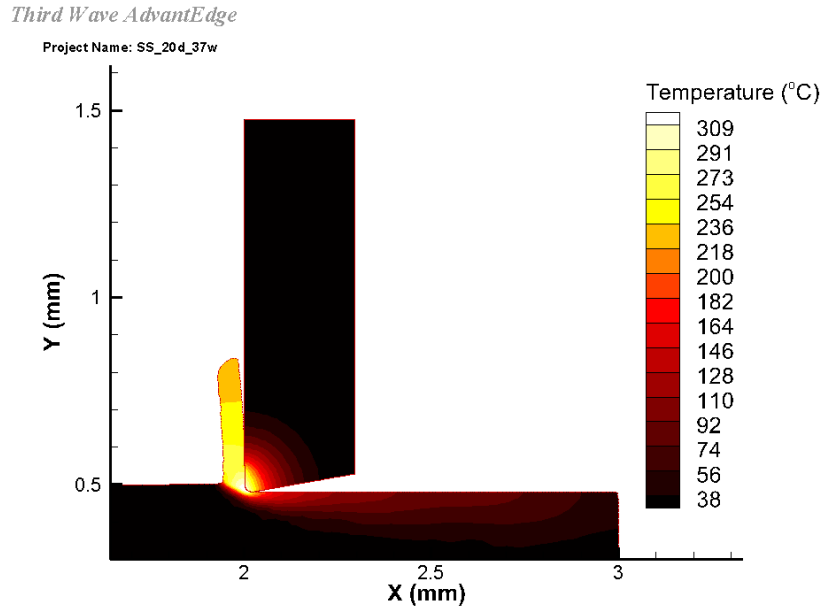


Figure 8-25. 304 SS Temperature Profile at 1 m/s and 20 μm Depth

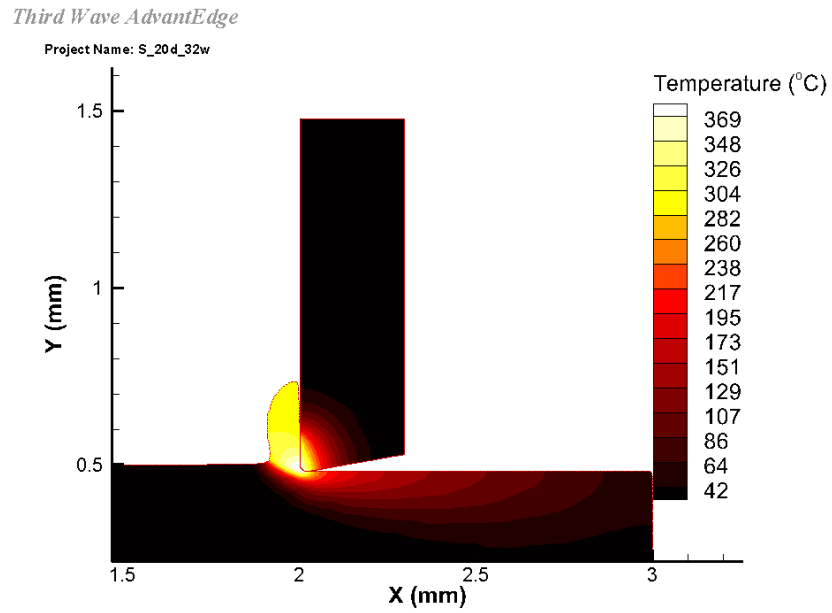


Figure 8-26. 1215 Temperature Profile at 1 m/s and 20 μm Depth

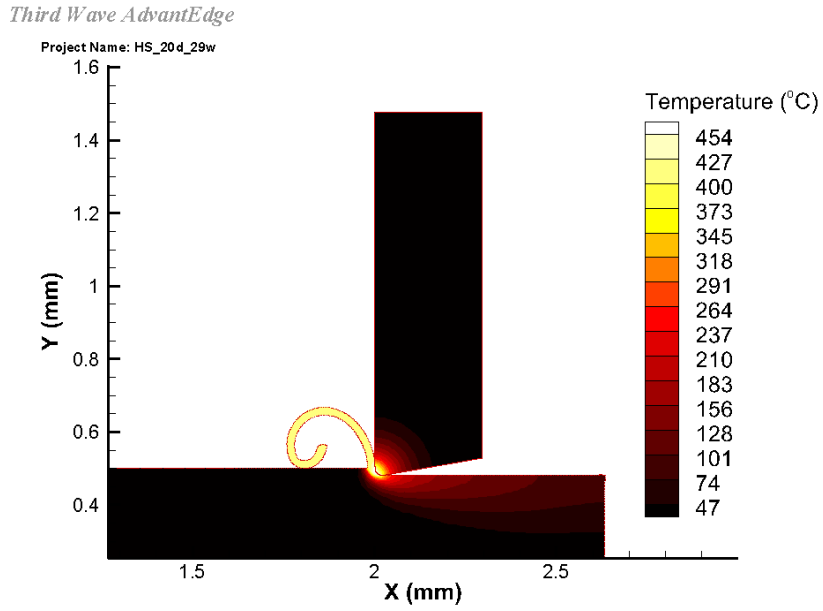


Figure 8-27. 52100 Temperature Profile at 1 m/s and 20 μ m Depth

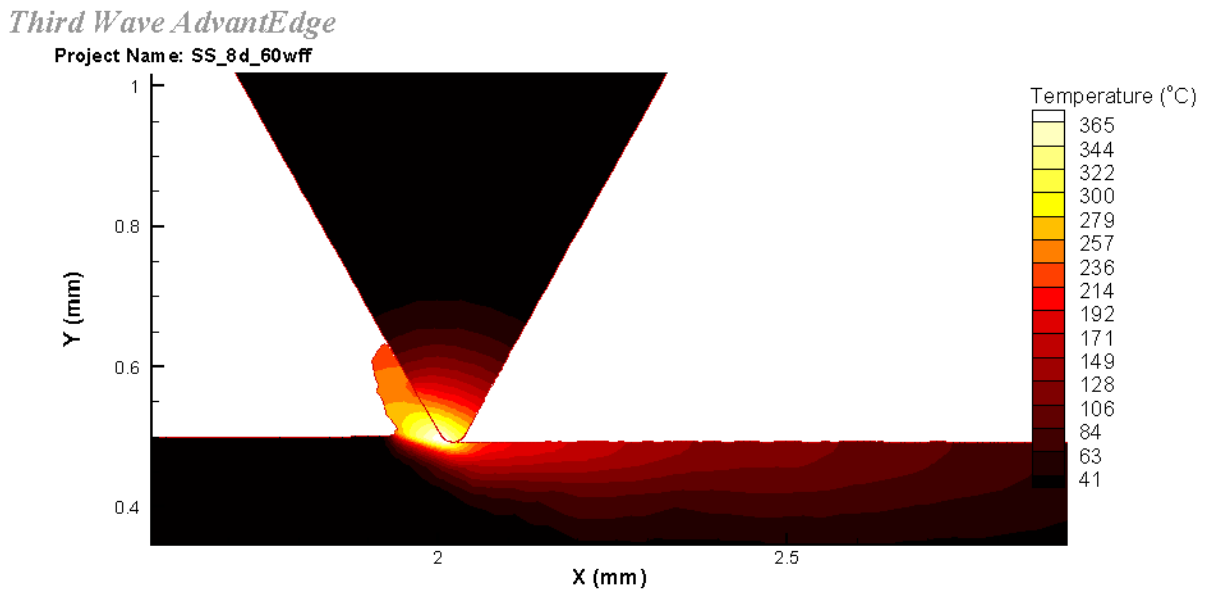


Figure 8-28. Negative Rake Orientation for 304 SS at 1 m/s and 20 μ m Depth

At this point the results for Third Wave temperatures are provided solely for future reference of the modeled temperatures for the given parameters. The models can be compared further if future experiments are reproduced while a suitable temperature measurement technique is utilized.

8.2.8 THIRD WAVE MODEL SHEAR ANGLE

The shear angle can be extracted from the Third Wave models by measuring the chip morphology. The shear angle was calculated for each model by looking at the area of maximum strain rate and measuring the angle at which it occurred. The maximum strain rate occurred on the shear plane of the chip/workpiece. The chip morphology for each simulated set of parameters was shown in Figure 8-25 to Figure 8-28 in the temperature simulation section. The predicted shear angles for each of the models are given in Table 8-7. The shear angles for the 1215 and 304 SS are comparative to the experimental conditions but much different for the 52100 steel.

Table 8-7. Third Wave Shear Angles

Material	Third Wave Shear angle	Experimental Shear Angle
Zero Rake: 1215 Steel	16.3°	13.2°
Zero Rake: 304 SS	18.0°	16.5°
Zero Rake: 52100 Steel	35.8°	16.2°
Negative Rake: 304 SS	7.8°	7.2°

The similarity in the predicted 1215 shear angle to experimental further suggests, in light of matching forces, that the model could be used for further 1215 experimental testing in the zero rake orientation. Conversely the similarity in 304 SS shear angle but the difference in force prediction per grit orientation suggests that the model may be able to be reworked to more accurately represent the experimental conditions. Modeling with 3D geometry in Third

Wave is a suggestion for further exploration, especially for the zero rake orientation. A 3D model for the zero rake tool could give insight to whether or not the 2D simulation represented material flow well at the cutting edge. The disparity for the 52100 steel suggests that the material characteristics and/or modeled parameters in Third Wave do not represent the experimental 52100 steel. The closeness of the negative rake 304 SS shear angle and also forces suggest that AdvantEdge could be effectively used for further experimental comparison and supplementation for the 304 SS workpiece at the negative rake tool.

9 CONCLUSIONS

A grit tool holder was developed to hold and test shaped alumina grits in similar orientations that would occur on a coated abrasive product. Methods were explored to quantify and compare single grit performance for grinding applications. Studying individual grains have proven challenging due to localized geometry and differences between individual grits. Macroscopic abrasive grits were used in experiments to have a more controlled shape and contour compared to crushed grits, but even the shaped grits contained localized geometry differences at the location of material removal. The differences in localized geometry produced cutting and thrust forces that had variation in experiments at the same parameters.

Methods were developed to observe individual grits in the process of material removal action. A high speed camera was used to capture video of cutting at 6006 FPS. The video quality was dependent on the planarity of the grits, but was used to effectively distinguish chip formation, material build up, and fracture for individual grains. Grit geometries that deviated from the high speed imaging field of view resulted in a blurred image. A lower magnification lens could be used to have a larger depth of view at the expense of the image magnification. The high speed imaging optics were used in conjunction with experimental forces to visualize material pickup accumulate at the tool/chip interface as the tool forces increased. Several instances of cutting correlated material pickup with a rise in cutting forces that induced fracture. However, material pickup was not always present in videos when the force rose and a fracture occurred. Occurrences that were not captured on video were attributed to the event not being located within the focal depth of the optics.

Chip formation characteristics were also visualized with the high speed video. It was used to determine shear angles for cutting speeds at 1 m/s and below. However, shear angle measurements could only be taken during periods of high speed video when distinct chip characteristics were present. More shear angle measurements are needed to validate the experimental shear angles because only small segments of videos were considered clear enough for measurements.

In light of geometrical differences affecting grit characteristics, experimental analysis was developed to distinguish and compare grits of slightly different geometry. Workpiece measurement techniques were used to successfully compare experiments where variable grit geometry would otherwise make comparisons difficult. Surface profiles were used to measure the removed chip area of non-overlapping tool paths so experimental forces could be related. The methods to define the contact area were based on the Arcona model. The measured surface profiles and grit contact geometry provided a basis for repeatable experimental results. Distinct relationships between experimental parameters were found, but more experimental results are needed for conclusive results. Preliminary results showed that the workpiece hardness directly impacts cutting and thrust forces. Forces between 304 SS, 1215 steel, and 52100 steel were compared. 1215 steel had 8% lower cutting forces and 14% lower thrust forces than the 304 SS, while significantly harder 52100 steel was 116% and 285% greater than cutting and thrust forces than the 304 SS material.

The specific shaped grit that was studied had two distinct orientations of possible cutting conditions but could also be mounted anywhere between the two orientations. The two extreme rake angle orientations were represented by either a 0° rake angle with a $20\ \mu\text{m}$ edge radius or a -30° rake angle with a $300\ \mu\text{m}$ wide flat face. A third orientation was tested which was halfway between the two previous orientations. The measurement techniques used for grit comparison were utilized to show that the 0° rake angle orientation removed material at the lowest force at a given removed chip area on 304 SS. The -30° rake grit orientation produced 32% higher cutting forces and 86% higher thrust forces than the 0° rake at comparative material removed areas on a 304 SS workpiece. The halfway rake orientation

had the largest experimental forces at 87% and 199% greater cutting and thrust forces than the 0° rake orientation. Comparative cutting statistics and relationships were demonstrated and could be used to more effectively design and compare various grit shapes by using the measurement techniques. The measurement and experimental methods can effectively distinguish cutting characteristics and parameters in single grit testing.

The experimental methods and measurement techniques were used effectively to compare single grit performance. It was possible to compare experimental data with respect to specific cutting energy. The specific cutting energy could be used to determine effective experimental conditions such as optimal grit geometry, effective parameters for different workpiece materials, or could be expanded to compare grit friability.

The experimental data was compared to a force model described by Arcona, but was determined to not be an effective tool for grit performance prediction at this time. Nevertheless experimental data was also compared to Third Wave AdvantEdge cutting simulation package and returned mixed results. 2D Third Wave models for the grits did not produce effective simulations for most conditions. The simulation and experimental data disparity was most likely due to an incorrect assumption of tool geometry, specifically tool width, in the 2D simulation. This hypothesis was determined after the negative rake orientation simulations on 304 SS. The negative rake orientation had a more reasonable 2D geometry and produced results that resembled 304 SS experiments better. Further work is needed to expand the Third Wave tool models into an effective modeling tool.

9.1 FUTURE WORK

Further work can be conducted to extend the methods developed for single grit experimentation and comparison. For instance, the high speed video images were successful in capturing material removal of a single abrasive grit but had issues with grits that were not completely in the field of view of the optics. Even material pickup and chip formation was not completely visualized because they did not happen in the field of view of the camera. A lower magnification optical setup could provide a larger field of view at the expense of the magnification. A 20x microscope objective could be used to better visualize overall chip

formation and material build up. A larger portion of the grit contact or width of the cutting process would be within the field of view. Having a lower magnification lens would also allow more light to enter the detector and allow a faster shutter speed.

The Talysurf was used to measure the surface profiles of the grit in the workpiece, but using the Polaris would provide more information of the profile change. A larger quantity of profile data could be extracted and matched with experimental forces with the Polaris. However the issue of probe dropout at steep grooves or burred edges prevented Polaris measurements. A more robust aberration probe on the Polaris machine may provide a better surface profile measurement. The data density on Polaris in the circumferential direction of the workpiece could be improved by having a higher data collection rate on the aberration probe. Alternatively this could also be accomplished by slowing the spindle speed which would result in a longer data collection time.

Experimental results could be further compared over a broader range of cutting speeds for each material, but especially on 304 SS. The three experimental speeds on the 304 SS material showed that there may be some sort of minimum in specific energy between a 1 m/s to 8 m/s cutting speed. Further speed experiments would determine if this is actually a minimum or just a result of variation in experimental results. Also a further comparison of speeds closer to 20 m/s would provide a better comparison from the experimental single point turning speeds to speeds that are more representative of a coated abrasive.

More experiments and research with the Arcona tool force model could determine if it could be updated with a modification for tools that have a large cutting radius relative to the depth of cut.

Third Wave simulations may be able to more accurately determine cutting characteristics of abrasive grits using a 3D simulation model. The 2D experiments conducted showed mixed results for different materials and orientations. A 3D simulation should accurately define grit geometry, such as the non-uniform contact widths of each grit orientation. Future

comparison with experiment results could determine if Third Wave is an effective modeling tool for shaped single grit experiments.

REFERENCES

- [1] ME Merchant. Some Observations on the Past and Present of Research on Machining and Grinding, Applied Mechanics Reviews. 46 (1993) 72-73.
- [2] MC Shaw. Some Observations Concerning the Mechanics of Cutting and Grinding, Applied Mechanics Reviews. 46 (1993) 74-79.
- [3] ME Merchant. Mechanics of the Metal Cutting Process. I. Orthogonal Cutting and a Type 2 Chip, J.Appl.Phys. 16 (1945) 267-275.
- [4] JD Drescher, Tool Force, Tool Edge, and Surface Finish Relationships in Diamond Turning. PhD Dissertation, North Carolina State University. (1991).
- [5] C Arcona, Tool Force, Chip Formation, and Surface Finish in Diamond Turning, PhD Dissertation, North Carolina State University. (1996).
- [6] MC Shaw, Principles of abrasive processing, Clarendon Press; Oxford University Press, Oxford; New York, 1996.
- [7] JA Schey, Introduction to manufacturing processes, McGraw-Hill, Boston, 2000.
- [8] S Kalpakjian, Manufacturing engineering and technology, 6th ed., Prentice Hall, New York, 2010.
- [9] S Mezghani, M El Mansori. Abrasiveness properties assessment of coated abrasives for precision belt grinding, Surface and Coatings Technology. 203 (2008) 786-789.
- [10] 3M, 3M Cubitron II Abrasives. http://solutions.3m.com.au/wps/portal/3M/en_AU/Cubitron-II/Home/, Jul 2013 (2014).
- [11] S Malkin, Grinding technology : theory and application of machining with abrasives, Industrial Press, New York, 2008.
- [12] WB Rowe, Principles of modern grinding technology, William Andrew, Oxford ; Burlington, MA, 2009.
- [13] SW Date, S Malkin. Effects of grit size on abrasion with coated abrasives, Wear. 40 (1976) 223-235.
- [14] AP Mercer, IM Hutchings. The deterioration of bonded abrasive papers during the wear of metals, Wear. 132 (1989) 77-97.

- [15] J Shibata, I Inasaki, S Yonetsu. The relation between the wear of grain cutting edges and their metal removal ability in coated abrasive belt grinding, *Wear*. 55 (1979) 331-344.
- [16] T Kayaba, K Hokkirigawa, K Kato. Analysis of the abrasive wear mechanism by successive observations of wear processes in a scanning electron microscope, *Wear*. 110 (1986) 419-430.
- [17] RG Visser, RC Lokken. The effect of the severity of the grinding mode on the wear characteristics of grade 36 Al₂O₃- and Al₂O₃-ZrO₂-coated abrasive belts, *Wear*. 65 (1981) 325-350.
- [18] AL Carrano, JB Taylor. Geometric Modeling of Engineered Abrasive Processes, *Journal of Manufacturing Processes*. 7 (2005) 17-27.
- [19] X Chen, W Brian Rowe. Analysis and simulation of the grinding process. Part II: Mechanics of grinding, *Int.J.Mach.Tools Manuf.* 36 (1996) 883-896.
- [20] ZB Hou, R Komanduri. On the mechanics of the grinding process – Part I. Stochastic nature of the grinding process, *Int.J.Mach.Tools Manuf.* 43 (2003) 1579-1593.
- [21] R Komanduri. Some aspects of machining with negative rake tools simulating grinding, *International Journal of Machine Tool Design and Research*. 11 (1971) 223-233.
- [22] MC Shaw, *Metal cutting principles*, Oxford University Press, New York, 2005.
- [23] BM Lane, *Development of Predictive Models for Abrasive and Chemical Wear of Diamond Tools*, PhD Dissertation, North Carolina State University. (2010).
- [24] BM Lane, M Shi, TA Dow, R Scattergood. Diamond tool wear when machining Al6061 and 1215 steel, *Wear*. 268 (2010) 1434-1441.
- [25] M Shi, *Thermo-Chemical Tool Wear in Orthogonal Diamond Cutting Steel and Stainless Steel*, MS Thesis, North Carolina State University. (2010).
- [26] M Shi, B Lane, CB Mooney, TA Dow, RO Scattergood. Diamond tool wear measurement by electron-beam-induced deposition, *Precis Eng.* 34 (2010) 718-721.
- [27] Kistler., *Data Sheet*. Type 9251A, 9252A, 9250A4, 9251A4. Kistler Instrument Corp., Amherst, NY,.
- [28] C Arcona, TA Dow. An Empirical Tool Force Model for Precision Machining, *Journal of Manufacturing Science and Engineering*. 120 (1998) 700-707.

[29] E Miller, Deflection Prediction and Error Correction of High Speed Miniature Milling Tools, MS Thesis, North Carolina State University. (2000).

[30] L MatWeb, <http://www.matweb.com/>, MatWeb: Material Property Data. 2014.

[31] H Ernst, ME Merchant. Chip Formation, Friction, and High Quality Machined Surface
, Surface Treatment of Metals (ASM). (1941) 299-378.

[32] TD Marusich, M Ortiz. Modelling and simulation of high-speed machining, Int J Numer Methods Eng. 38 (1995) 3675-3694.

[33] H Bil, SE Kılıç, AE Tekkaya. A comparison of orthogonal cutting data from experiments with three different finite element models, Int.J.Mach.Tools Manuf. 44 (2004) 933-944.

[34] Third Wave Systems, AdvantEdge, v6.2-010 (1997-2014).

APPENDICES

10 EXPERIMENTAL SETUP DETAILS

10.1 HIGH SPEED CAMERA SETTINGS

The high speed camera settings were tweaked to produce the best optimal images for the experimental setup. The camera gain, exposure, and pixel depth were set to the values given in Table 10-1. These settings were used in post processing using the Phantom MultiCam Software while leaving the original video unaltered. The post processing assisted in distinguishing features of the chip and grit. The image adjustments in conjunction with the 200W light source produced effective parameters to view cutting at 6006 FPS.

Table 10-1. High Speed Camera Settings

Image Adjustment	Value
Brightness (%)	0.00
Gain	0.283
Gamma	0.716
Sensitivity	64.000

10.2 CAMERA FOCUSING TECHNIQUES

The camera was focused on features at different focal depths through various times in the experiments to determine best qualitative focusing characteristics. The focusing technique varied slightly for the various orientations. The focus regions are given in Figure 10-1 for the negative and zero rake orientations; the halfway rake uses the same method as the zero rake technique. The camera looks at the triangular face of the grit for the negative rake orientation and at the rectangular face for the zero rake orientation.

The negative rake orientation was focused on the tip of the grit or the first grit contact point to the workpiece. With proper grit selection described in Section 5.5, the negative rake orientation was straightforward and the camera was focused on the front triangular face of

the grit while also focusing on the tip of the grit. This occurred when the tip of the grit was at the front of the triangular face in Figure 10-1a. For grits that were not completely flat the focus point was moved back the distance of the depth of cut from the tip of the grit shown by the secondary focus point in Figure 10-1a. This sometimes led to slightly blurred grit faces, but good chip formation. Because this point was at the depth of cut of the experiment, it also corresponded to the maximum width of chip formation. The width is shown with the depth of cut dashed line for the rectangular-like face in Figure 10-1b.

The zero rake orientation was focused on tip of the grit that extended furthest, which would be the first point of contact for cutting as shown in Figure 10-1b. Due to the orientation of the grit, this would still result in a blurred image, but the operator would dither the focus and determine the point where the outline of the grit was least unfocused. The focus point provided an image of the tip of the chip geometry. The tip of the chip stayed in line with the tip of the grit most of the time. The secondary camera focus location was the depth of cut distance from the furthest edge; to give room for a chip that was pushed closer to the camera. The secondary focus point is shown in Figure 10-1b on the rectangular-like face.

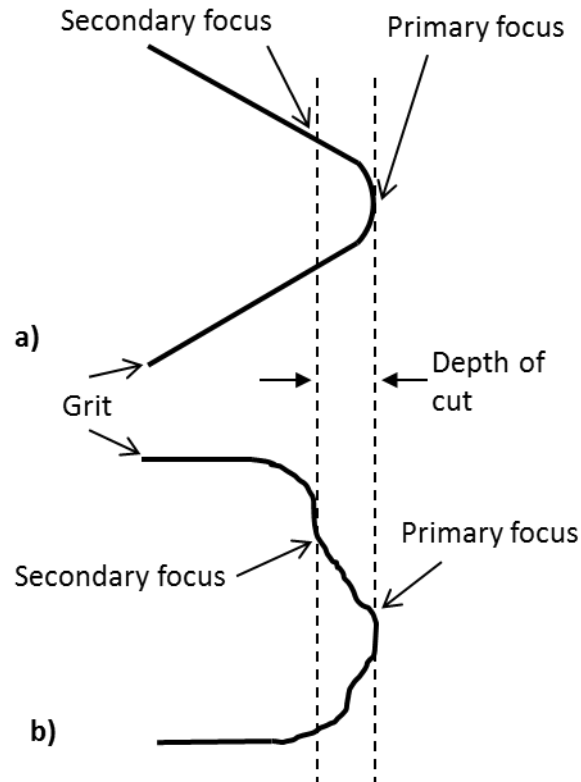


Figure 10-1. Camera Focus Locations for: a) Negative Rake Orientation Viewpoint, b) Zero Rake Orientation Viewpoint

In both orientations, localized grit geometry tended to push chips in directions, into or out of the expected focal depth. Chip formation was variable and did not always behave as described. The guidelines are given for most grit/chip focusing cases.

11 THIRD WAVE

11.1 FLANK AREA INTERPOLATION CURVES FROM MEASUREMENTS

The modeled Third Wave areas were interpolated from the measured experimental areas and heights described by Equation (8-1) and Section 8.2.3. The experimental area was curve fit to find a best fit relation to groove depth for each experimental parameter (workpiece material or tool orientation). The 2D AdvantEdge model is a rectangular chip area, so the fitted area was treated as a rectangular area to estimate a model tool width at specific depth

parameters. The area is divided by the depth to estimate the width. Thus the modeled tool geometry was used to compare to the experimental removed area at each depth. Equations for the specific curve models are given in Equations (11-1) to (11-4).

304 SS workpiece for zero rake orientation:

$$A_{304SS} = 0.5478d^2 + 25.69d$$

$$W_{304SS} = \frac{A}{d} = 0.5478d + 25.69 \quad (11-1)$$

1215 steel workpiece for zero rake orientation:

$$A_{1215} = 0.3505d^2 + 25.07d$$

$$W_{1215} = \frac{A}{d} = 0.3505d + 25.07 \quad (11-2)$$

52100 steel workpiece for zero rake orientation:

$$A_{52100} = 1.217d^2 + 4.567d$$

$$W_{52100} = \frac{A}{d} = 1.217d + 4.567 \quad (11-3)$$

304 SS workpiece for negative rake orientation:

$$A_{Neg} = 7.779d^2 - 5.151d$$

$$W_{Neg} = \frac{A}{d} = 7.779d - 5.151 \quad (11-4)$$

11.2 THIRD WAVE MODEL MATERIALS

Some material properties can be viewed in Third Wave. The properties for the default materials that were used for the various workpieces are given in Table 11-1. The thermal and some mechanical properties of the materials were hidden from the user.

Table 11-1. Default Third Wave Workpiece Properties

Material	Hardness	Ultimate Tensile	Yield Strength
304 -SS	248 Vhn	505 MPa	215 MPa
AISI 1118 (1215)	160 Vhn	525 MPa	315 MPa
AISI 52100	653 Vhn	-----	-----

12 FURTHER EXPERIMENTAL SETUP DETAILS

12.1 WORKPIECE CONSIDERATIONS

A discontinuous workpiece was used to more accurately resemble contact in grinding where the grit moves in and out of workpiece contact for specific periods of time. Two separate discontinuous discs were compared, one to resemble grinding conditions and one to accommodate data acquisition. Grinding conditions are very broad, however for comparison to grinding the workpiece was designed with 3 mm of contact and 30 mm of travel out of contact. This workpiece was never used in experiments but is utilized to give a perspective of the discontinuous workpiece suggested for data acquisition purposes. The suggested workpiece has equal segments of contact and non-contact in 45° increment's, corresponding to roughly 40 mm of contact for a four inch diameter disk. A graphical comparison between the two discontinuous workpieces is shown in Figure 12-1.

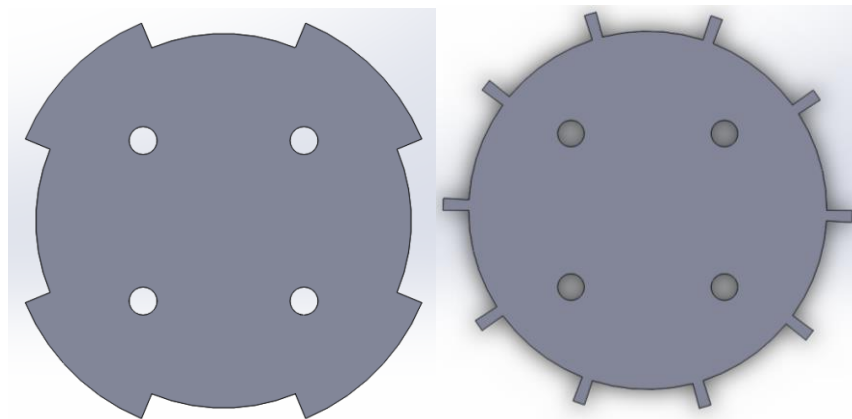


Figure 12-1. Discontinuous Workpieces: 40 mm Contact (left), 3 mm Contact (right)

The data acquisition rate is directly impacted by the contact distance and speed of the workpiece. In cutting experiment the force data was recorded at 5 kHz and video at 6 kHz. Depending on contact length and workpiece speed, capturing force and video data becomes more critical as fewer amounts of data are recorded. For the 3 mm contact length workpiece

at 1 m/s the time in contact is only 0.003 s, corresponds to only 151 force recordings and 182 frames from the camera. This amount is reduced at higher cutting speeds. At 5 m/s only 30 force recordings and 36 frames would be recorded per contact. However, with the 40 mm contact workpiece at 5 m/s 83 force samples and 100 frames can still be recorded for each contact. Even though the 40 mm contact workpiece may still be larger contact times for grinding, the data acquisition accommodation makes it a better choice for experiments.

The segmentation will induce some amount of vibration into the system, either vibration of the workpiece itself or vibration of the load cell. The response of the load cell in the cutting force direction is 11.6 kHz. This frequency is much higher than any input that could be induced by workpiece contact, so vibration effects should not be a factor.

12.2 LOAD CELL AMPLIFIER SETTINGS

The settings for the amplifier described in the experimental setup are given in Table 12-1.

Table 12-1. Amplifier Settings and Gains for Load Cell

Setting	Cut Force	Thrust Force	Side Force
Transducer Sensitivity Range	100-1.1k	100-1.1k	100-1.1k
Mechanical Units per Volt	50m	50m	50m
Transducer Sensitivity	676	676	536
Capacitor Range	Long	Long	Long
Calibration Factor	4.33 N/V	4.23 N/V	7.65 N/V

12.3 NATURAL FREQUENCY OF LOAD CELL

The natural frequency of the load cell was measured experimentally by striking the load cell with a small mallet and measuring the response at 30 MHz on an oscilloscope. The measured response is given in Figure 12-2 for measured voltage over time. The response

data is then interpreted via a Fast Fourier Transform (FFT) to determine individual frequencies. The strongest signal frequency from the data taken in the cutting force direction was 11616 Hz. Several responses are shown in Figure 12-2 and Figure 12-3. The load cell natural frequency was determined to be much higher than any induced frequency from the designed discontinuous workpieces.

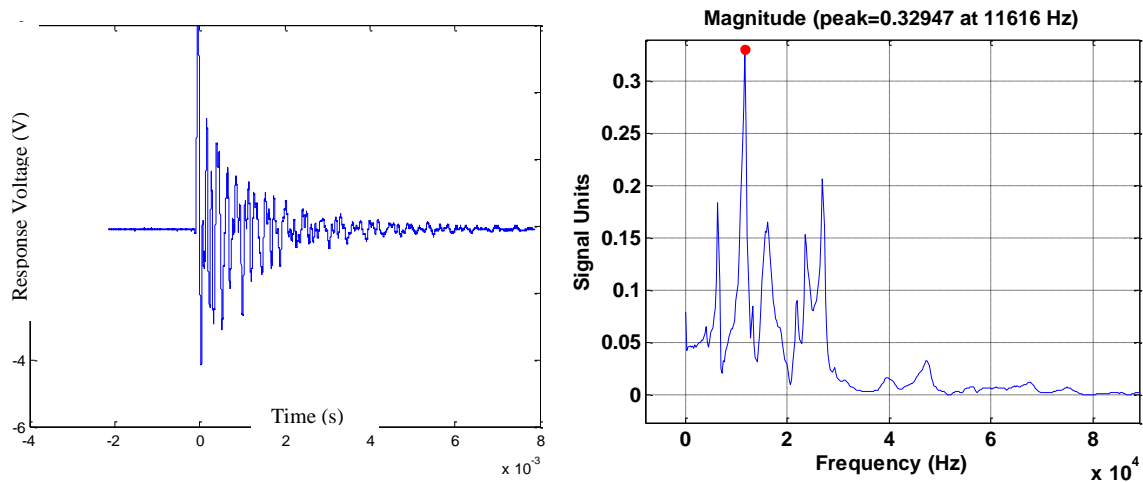


Figure 12-2. Load Cell Response (left) and FFT (right)

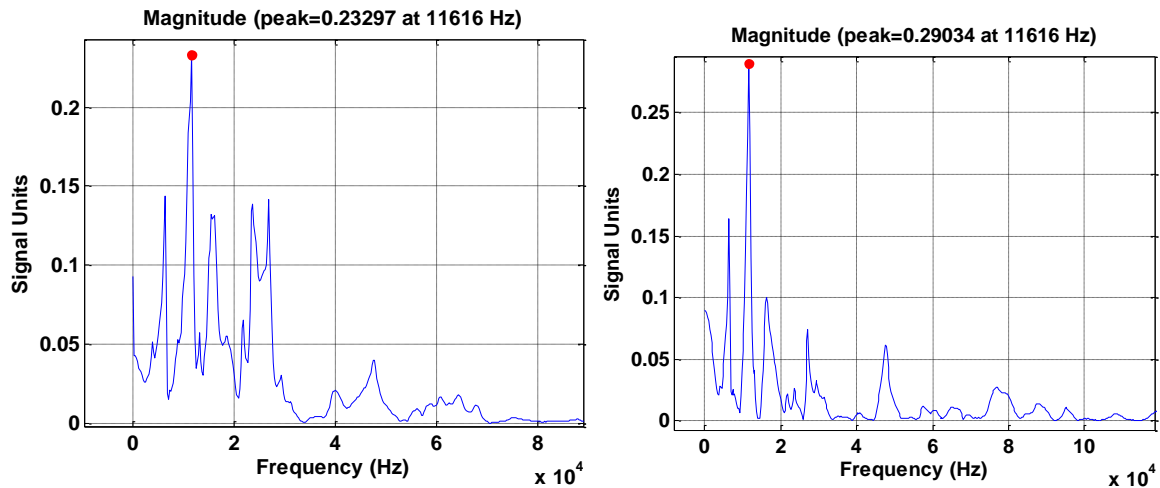


Figure 12-3. FFT of Several Load Cell Responses

13 TEMPERATURE

13.1 CUTTING TEMPERATURES

An original goal of the project was to determine the peak cutting temperatures of the grit and temperature distributions of the grit. Several aspects of temperature measurement were investigated including an infrared pyrometer, infrared camera, and mounted thermocouple. The infrared pyrometer and camera measurements were not followed through with while the thermocouple measurements were prone to error. More information on thermocouple experiments and results is discussed further. Predicting heat generated in the cutting process through an energy balance roughly characterizes that 2/3 to 3/4 of generated energy is a result of the shear plane in the chip and the remaining energy is due to frictional forces on the tool. However, for grinding this energy distribution may change so that the workpiece experiences about 80% of the energy according to Sato [2].

13.2 THERMOCOUPLE EXPERIMENT

A thermocouple was clamped between the grit and the tool holder to record temperature during cutting experiments. A brass workpiece material was used to allow steady state temperature measurements because a steel workpiece may induce grit fracture before a steady state was achieved. An 80 μm diameter thermocouple was placed 750 μm from the tool cutting edge. The thermocouple and grit placement are shown in Figure 13-1.

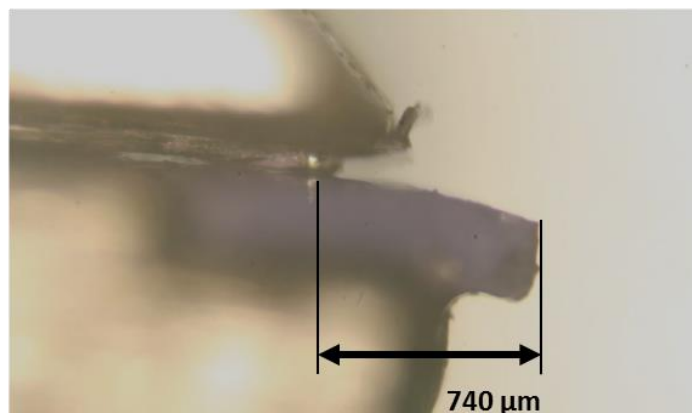


Figure 13-1. Thermocouple Placement on Grit

The temperature was measured over a range of depths of cut and traverse feeds. Two separate sets of experiments with overlapping tool paths were used to cut brass material. One set of experiments were conducted at a 126 $\mu\text{m}/\text{revolution}$ feed rate with a 10, 20, 30, 40, and 50 μm depths of cut and the other set of experiments were at 10 μm depth of cut with a traverse feed of 45, 91, and 136 $\mu\text{m}/\text{revolution}$. The temperature and forces are shown in Figure 13-2 with respect to the approximated removed area of both experiments. The removed area was estimated by multiplying the feed by the depth of cut for the given experiments.

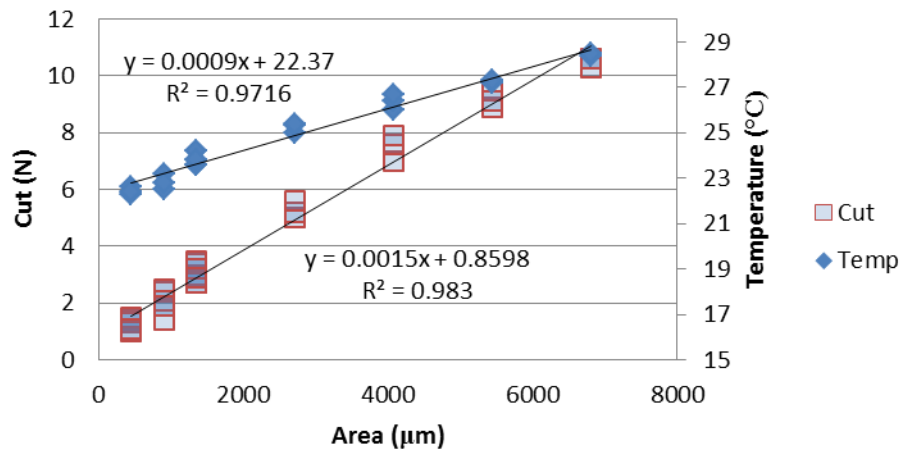


Figure 13-2. Measured Cutting Forces and Temperatures

The ambient temperature was 21.5 $^{\circ}\text{C}$ and the peak measured temperature was 29 $^{\circ}\text{C}$. For the overlapping traverse experiments on brass, the measured temperature rise is very small at the location of the thermocouple. However, a model was investigated to predict temperature at the cutting interface. A single grit and thermocouple were used for the all of the experiments with no grit fractures.

13.3 THERMOCOUPLE MODEL RELATION

An ANSYS model was created to relate the measured temperature to the peak temperature but was deemed insufficient. The thermocouple model relation was deemed a poor method to relate the measured thermocouple temperature to the peak temperature of the tool due to the large thermal gradient that would be present across the tool. The thermocouple would read a low temperature while the tip of the grit would theoretically be at a very high temperature. Using a simple analytical model of radial 2D heat transfer given in Equation (13-1), the temperature gradient across the triangular grit is demonstrated in Figure 13-3. The analytical model is treated as a section of a circle with a constant heat input at the smaller radius, representative of the radius of the grit. The grit is assumed to be a constant thickness L and 60° , or $1/6$, of a circle. The analytical model only serves as a simplified model to show the challenge with relating a temperature measured from a thermocouple to the peak tool temperature.

$$Q = kV(r)\Delta T$$
$$Q = \frac{2\pi L}{6 \ln\left(\frac{r_o}{r_i}\right)} \Delta T \quad (13-1)$$

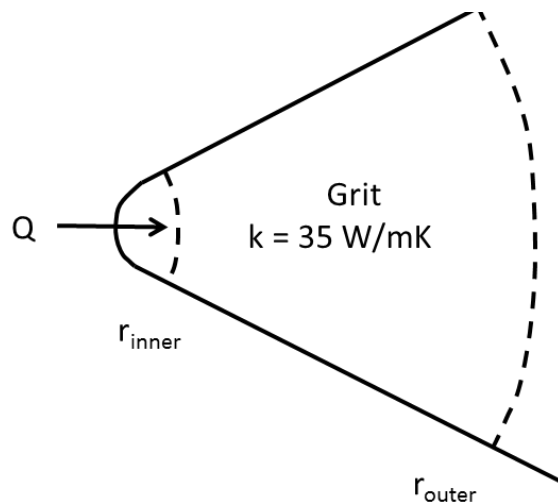


Figure 13-3. Analytical Grit Model as a 60° Segment of a Circle

The grit thermal conductivity was assumed to be a constant 35 W/mK, however if the thermal conductivity of alumina changes with respect to temperature this would create an even more sensitive model. For a single thermal conductivity two different measured temperatures are shown in Figure 13-4 with their theoretical temperature curve. A 25°C and 28°C thermocouple measurement represents a 20 °C peak temperature difference according to the model. The measured temperatures are marked with the vertical line at 740 μm that is labeled with the “thermocouple placement location.” The x axis is the distance away from the grit radius. So the point at about 20 μm is assumed to be the maximum temperature location.

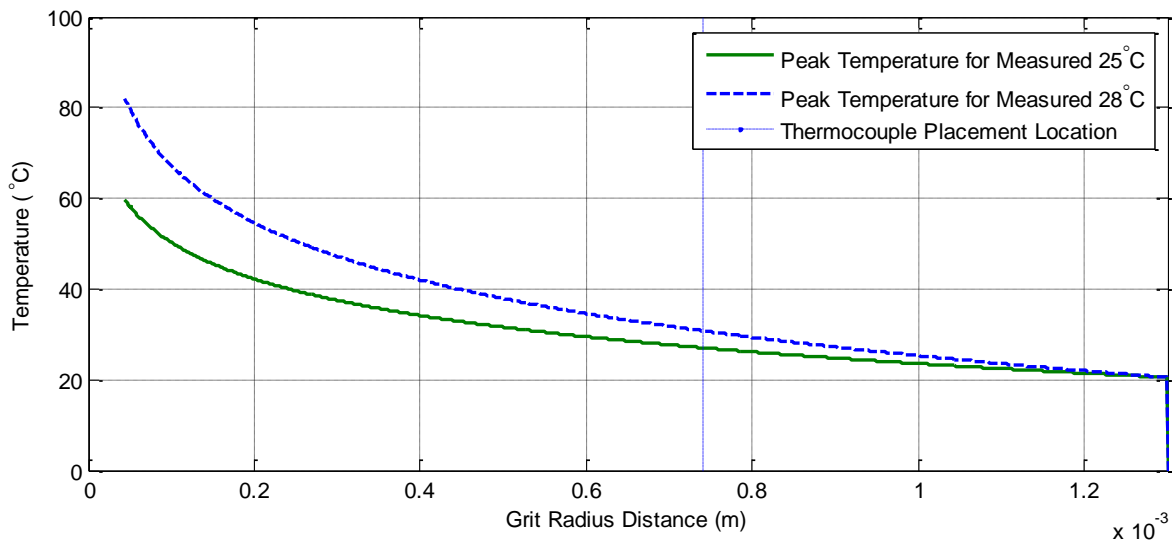


Figure 13-4. Peak Grit Comparison for Two Measured Temperatures

The temperature measurement was discontinued for the steel workpieces. Even if an ANSYS model was completely functional and accurate, confirming the accuracy of the model for individual grits would prove time consuming. Each grit, with slight variations in contact area and even differences in overall dimensions, could potentially alter the modeled temperature relation to the measured thermocouple temperature.

14 GRIT CLAMP/HOLDER DRAWING

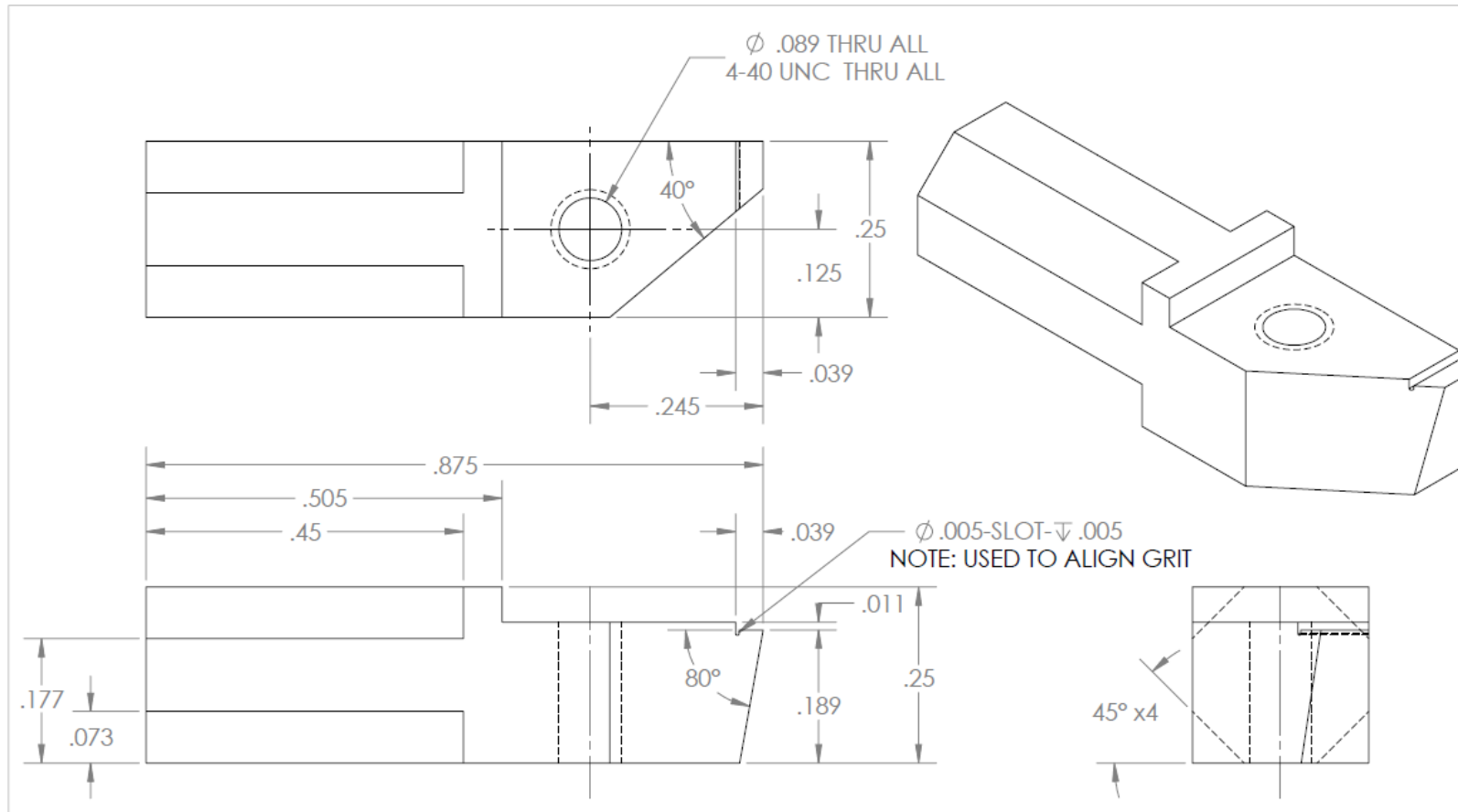


Figure 14-1. Grit Holder Dimension Drawing: Units are in Inches

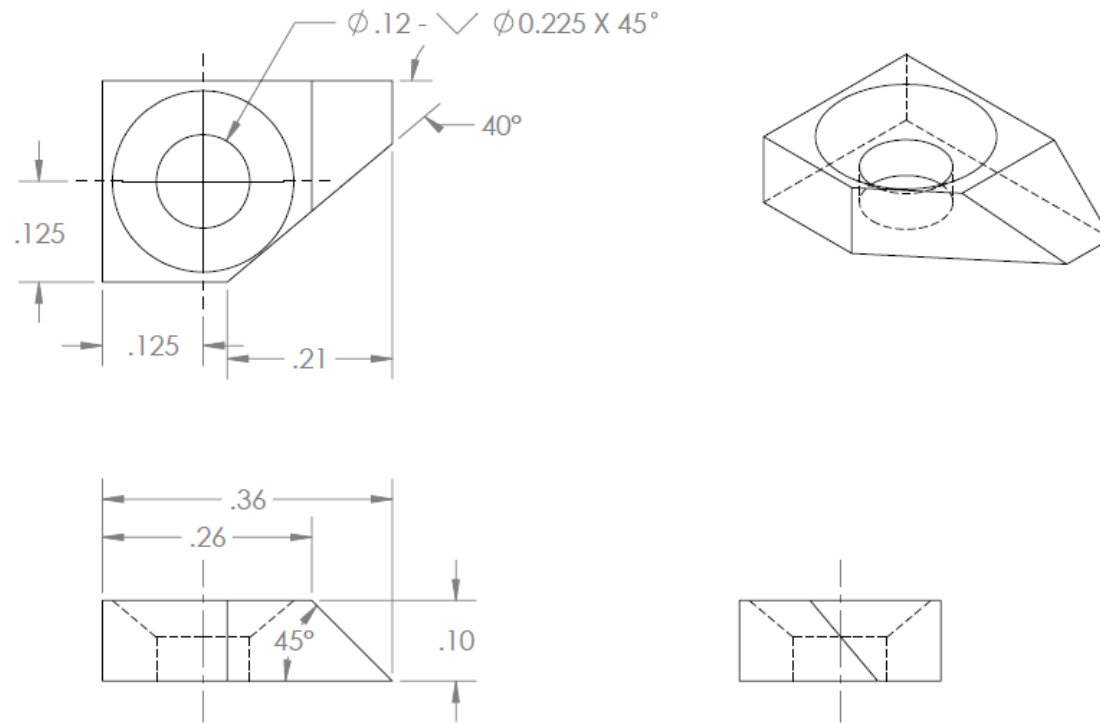


Figure 14-2. Grit Clamp Dimension Drawing: Units are in Inches